Hochschule Wismar
University of Applied Sciences
Technology, Business and Design
Fakultät für Ingenieurwissenschaften

Deutsches Zentrum
DLR für Luft- und Raumfahrt
German Aerospace Center

Master-Thesis

PIC (Photonic Integrated Circuit) based high throughput optical communication system for space application

Submitted on:	03.06.2024
From:	Dinesh Kumar Umasankar
	born on 11.05.1998
	in Chennai
Matriculation number:	373616
Supervisor:	Prof. Dr.-Ing. habil. Andreas Ahrens
Second supervisor:	Dr. Jasmeet Singh
External supervisor:	Dr. Marcin Ziarko

Acknowledgment

I would like to express my sincerest gratitude to Prof. Dr.-Ing. habil. Andreas Ahrens, Dr. Marcin Ziarko and Dr. Jasmeet Singh for their incredible support and guidance throughout the completion of this thesis. Their expertise and knowledge were absolutely invaluable throughout all stages of this work. I am extremely grateful to Dr. Marcin Ziarko for giving me the incredible opportunity to work under his guidance at the German Aerospace center(DLR). His friendly advice and generous feedback helped me to gain so much knowledge and grow as a person professionally. I'd like to thank my supervisor Dr. Jasmeet Singh again for his constant feedback and encouragement, which helped me to complete this work. I must also thank Prof. Dr.-Ing. habil. Andreas Ahrens for his guidance during my thesis and for helping me throughout my Master's course.

I would also like to extend my wholehearted thanks to Mr. Giulio Terrasanta and Dr. Nicola Bergamasco for their amazing feedback and assistance throughout my journey of realizing this thesis. They made me experience a wonderful and joyful working atmosphere.

Finally, I would like to thank my parents, brothers, sisters and friends for their unwavering support, love and encouragement throughout this incredible journey. A special thanks to my girlfriend Lalitha Priya, for her incredible love and support which helped me to complete this thesis.

Kurzfassung

Intersatellitenlinks sind ein schnell wachsender Anwendungsbereich für die optische Kommunikation. Sie haben ein großes Potenzial, die bestehenden terrestrischen Netze zu ergänzen, um einen weltweiten Breitbandzugang zu ermöglichen. Während dicht besiedelte Gebiete durch Glasfaserverbindungen gut versorgt sind, können Satellitensysteme zur Abdeckung ländlicher oder abgelegener Gebiete eingesetzt werden. Die optische Satellitenkommunikation bietet nicht nur eine hohe Bandbreite, sondern auch Verbesserungen bei Kosten, Größe, Gewicht und Leistung, die durch die photonische Integration ermöglicht werden.

In dieser Arbeit wird das Thema der Skalierung von optischen Freiraumverbindungen auf 100 Gbps pro Wellenlängenkanal und darüber hinaus untersucht. Es wird eine quantitative Studie durchgeführt, um die optimalen Modulationsformate in Bezug auf Empfängerempfindlichkeit, Transceiver-Komplexität, Rauschanfälligkeit und spektrale Effizienz auszuwählen, um eine Datenrate von mindestens 100 Gbps zu erreichen. Das Ergebnis dieser Studie wird dann verwendet, um optische Schaltkreismodelle zu erstellen, um die Verbindungsleistung unter verschiedenen Systemrauschbedingungen zu analysieren und zu vergleichen, basierend auf realistischen Systemannahmen für eine Übertragung von einem geostationären Erdorbit-Satelliten zu einer optischen Bodenstation. Die Layouts der integrierten photonischen Schaltkreise für die analysierten optischen Systemmodelle werden entworfen und ihre Anforderungen an die Chipgröße werden untersucht. Das Potenzial für die Skalierung des ausgewählten Systems auf bis zu vier Kanäle unter Verwendung von Dense Wavelength Division Multiplexing wird untersucht und die Auswirkungen einiger nicht-linearer Effekte auf die Systemleistung werden analysiert.

Abstract

Intersatellite links are becoming a rapidly growing application area for optical communications. They have a great potential to complement the existing terrestrial networks in order to provide global broadband access. While densely populated areas are well served through optical fiber connections, satellite systems can be used to cover rural or more remote areas. Optical satellite communications offers not only high bandwidth, but also improvements in cost, size, weight and power (C-SWaP) offered by photonic integration.

In this thesis, the topic of scaling free-space optical (FSO) links to 100 Gbps per wavelength channel and beyond is investigated. A quantitative study is performed to select the optimal modulation formats in terms of receiver sensitivity, transceiver complexity, noise susceptibility and spectral efficiency to achieve at least 100 Gbps data rate. The outcome of this study is then used to prepare optical circuit models to analyse and compare the link performance under different system noise conditions, based on realistic system assumptions for a geostationary earth orbit (GEO) satellite to optical ground station transmission. The Photonic Integrated Circuit (PIC) layouts for the analysed optical system models are designed and their chip size requirements are studied. The potential for scaling the selected system up to four channels using dense wavelength division multiplexing (DWDM) is investigated and the impact of some non-linear effects on system performance is analysed.

Contents

1 Introduction

The usage of broadband internet access has increased significantly in recent years, and new solutions are required to provide broadband communication on a global scale [1]. In the past, telecommunication was limited by cables including optical fiber networks and their point to point communication range. Modern internet based technologies and services such as cloud services, Internet of Things (IoT) and big data applications require fast, reliable, large bandwidth and secure internet coverage [2]. In terrestrial networks, wired technologies such as optical fiber communication solves the problem in high-density metropolitan regions. However, the construction of optical fiber network is not profitable in remote areas with less population [2]. Satellite communication overcomes this bottleneck by providing global broadband coverage, which is also highly beneficial for emergency and disaster relief[1].

At present, most of the communication satellites use radio frequency (RF) technologies which have a limited bandwidth. On the other hand, optical wireless communication has advantages such as bandwidth up to 10 THz, license free spectrum, handling of high data rates, data security and implementation of complex optical networks. As a result, the satellites incorporated with this FSO communication technology solve the demand for global broadband internet access coverage [2]. For example, three satellites in GEO can cover the whole world excluding the poles [1]. The LEO satellite communication technology is also used for deep-space communication between the Earth and other planets [3].

1.1 Latest trends in optical satellite communication

The current RF based satellite communication system uses S-band (2-4 GHz), X-band (8-12 GHz), Ku-band (12-18 GHz) and Ka-band (26-40 GHz) in the RF spectrum [4]. However, as stated earlier, there is an exponential increase in demand for larger bandwidth and higher data rates. In order to meet these demands, the satellite operators are investigating into higher bandwidth bands such as V-band (40-75 GHz) and W-band (75-110 GHz). Alternatively, other scientific groups developing

high throughput communication satellite using optical communication technologies [4].

The higher bands of RF communication technology requires large antenna and high power, resulting in a larger system size, higher cost and bandwidth limitations. For example, a few recent proposals for global internet coverage using RF links such as Starlink by Space-X with 12000 satellites in low earth orbit (LEO), Oneweb with 900 satellites in LEO and Telesat with 300 to 500 satellite in LEO, all have bandwidth limitations [1].

On the other hand, optical communication technologies operate in higher frequency band, i.e. in THz frequencies, which have the property to transmit the data faster and have larger bandwidth compared to RF satellite technology. It also offers advantages such as secure data transmission due to its smaller illuminated "footprint" and reduction in size, weight and power (SWaP) of the on-board communication terminal, which increases the capacity of the payload for on-boarding other scientific instruments and/or reduces mission costs [5]. These factors lead to more research and development (R&D) activities towards smaller SWaP and high throughput optical satellite communication system around the world [4]. For example, as a part of the OSIRIS series programme, German Aerospace Center (DLR) has developed OSIRIS4CubeSat(O4C), also known as the PIXL-1 payload, which supports 100-Mbps downlink with a power consumption under 9 W and has a weight of only 395g [4].

Similarly, the National Institute of Information and Communications Technology (NICT) of Japan started to develop versatile miniaturised lasercom terminals that can be mounted on a small moving platform which will play an important role in the development of 5G and beyond 5G networks with stringent SWaP requirements [4]. At present, NICT is developing and designing CubeSat version transceivers to demonstrate experiments such as GEO-LEO acquisition and tracking tests at ultra-long distances, LEO-ground bi-directional 10 Gbps communication through the atmosphere and out of atmosphere between LEO and high-altitude platforms (HAPS) links [4].

The European Data Relay System (EDRS) already has an operational optical tech-

nologies such as LEO-GEO inter-satellite links instead of direct LEO-ground links. This optical network scenario allows longer link availability between LEO and GEO satellites provided with 1.8 Gbps data transfer [1][4]. NICT has a future vision to develop high throughput satellite by implementing robust RF links for the user side and optical feeder links on GEO-ground side because the clouds affect the optical feeder links severely [4]. From these examples, it is clear that researchers all around the world are already developing optical communication systems for satellite communication due to their various advantages.

Although optical communication technologies have advantages such as higher bandwidth of 10THz in the atmospheric transmission without any regulation, it still has relatively larger hardware components in terms of payload point of view and it is not fully developed to be integrated in the satellite system to support multiple terabits-per-second throughput [1]. To overcome these challenges scientists are investigating various technologies to develop and implement high throughput optical satellite communication systems with better C-SWaP characteristics.

1.2 Brief overview of Photonic Integrated Circuit(PIC)

PIC technology seems to be a potential area of interest to improve C-SWaP characteristics of the optical communication system, where the power consumption and the system footprint are reduced by miniaturization and integration of various optical components in a single chip [6]. One of the most mature and high-performing PIC platforms that have been developed is Indium Phosphide (InP), which allows for the monolithic integration of major active and passive optical components such as lasers, modulators and waveguides [7]. Therefore, the InP platform becomes a common choice for the implementation of advanced transmitters and receivers as a single complex photonic chip [7].

Figure 1 shows the basic block diagram of the PIC subsystem and the components that can be integrated on a single die for the satellite/ground station laser terminal. This implementation leverages PIC technology to become a key component of future optical space communication. Figure 2 also visualizes the size reduction potential of the PIC technology by placing the 10-cent coin beside a photonic chip as an example. The fact that such a miniaturised system includes a laser, modulator and a coherent receiver highlights the potential to improve SWaP parameters of the entire communication payload.
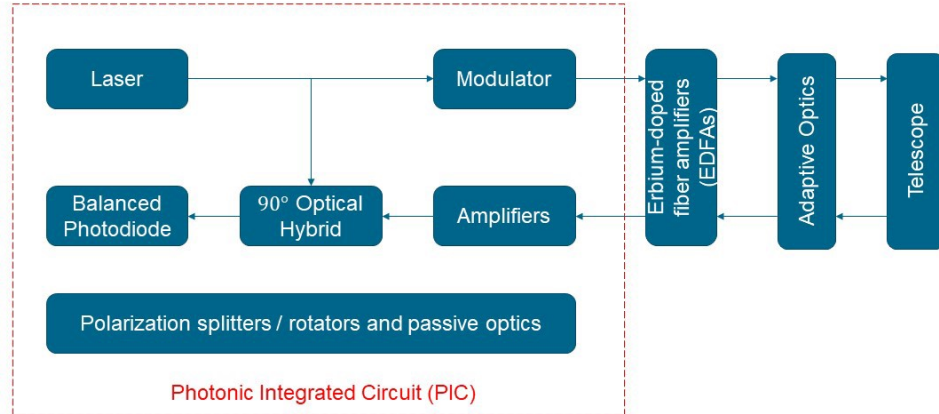
Figure 1: Block diagram of a PIC subsystem in satellite/ground station laser terminal. [6]

Figure 2: Image of PIC.

In contrast to the terrestrial communication systems, one of the major drawbacks of space communication is the impact of the harsh environment. One of such effects is radiation, which affects semiconductors at different levels in different orbital profiles according to their corresponding sources. These sources arise from a combination of galactic cosmic rays, high-energy solar flares and particles trapped by Earth's magnetosphere. The impact can range from single-event effect (SEE) to total-ionizing dose damage (TID) and displacement damage (DD) [6]. Therefore, it becomes a critical factor to gain knowledge about the radiation sources and their potential impact on various photonic components leading to degradation of system

performance.

Therefore, engineering the high throughput optical satellite communication system using PIC technology provides significant improvement in C-SWaP index.

1.3 Motivation

The increasing demand for high data rates, spectral efficiency and compact optical satellite communication system leads to the development of PIC based optical communication systems. Therefore it functions with higher-order modulation to meet the bandwidth demand and improve C-SWaP index. In this thesis, a quantitative study is carried out to select optimal modulation formats for the implementation of a high throughput optical communication system. The performance of selected modulation formats are analysed for a FSO link by simulating the corresponding optical systems, based on realistic system assumptions for a geostationary orbit (GEO) satellite to optical ground station transmission. Their corresponding PIC layout design is then performed.

The main objectives of this thesis are:

- Investigation of the scalability of FSO links to ≥ 100 Gbps per wavelength.

- Conduct a quantitative study to select the best implementation approaches in terms of receiver sensitivity, transceiver complexity, noise susceptibility and spectral efficiency for throughput scalability.

- Development of optical circuit models for the two most promising approaches to achieve the required system performance.

- Based on performance simulations of a realistic GEO satellite to ground station link, select an optimal implementation of optical transceivers for PIC design.

- Analyze the scaling-up potential of the previously selected system via dense wavelength division multiplexing (DWDM) to at least 4 channels. Focus on assessing non-linear effects and channel cross-talk on the system performance. Look into mitigation techniques to reduce these effects.

2 100 Gbps technology

To achieve 100 Gbps data rate transmission within the 100 GHz channel bandwidth according to the International Telecommunication Union (ITU) standard, the system should incorporate high speed electronics and optical components. Most importantly, the data should be modulated with high frequency carrier for longer and faster data transmission [8]. Generally, the carrier is an electromagnetic wave whose physical parameters such as amplitude, frequency and phase are modulated with data for a long distance transmission. In long distance optical communication system, Erbium Doped Fiber Amplifier (EDFA) plays an important role and its optimum amplification range falls in C and L bands of the communication spectrum [8]. Therefore, the data transmission utilizes the modulation of the carrier signal at C and L bands of the frequency spectrum.

The different types of modulation formats used in optical communication systems are shown in Figure 3 [9]. The most commonly used optical modulation format is on-off keying (OOK), where the amplitude of the laser pulse is modulated according to the data to be transmitted. The modulation formats that involve changing in the phase of the carrier signal are binary phase shift keying (BPSK) and differential binary phase shift keying (DBPSK), which are more robust to fiber propagation effects such as attenuation, dispersion and non-linear Kerr effects compared to OOK [8][9]. In BPSK modulation, the phase of the carrier signal is switched between 0 rad and π rad according to the message bits '0' and '1', respectively [9]. In DBPSK modulation, when bit '1' appears, the phase of the carrier signal is switched between $0 rad$ and πrad, but the phase of the carrier is unchanged for bit '0' [9].

OOK, BPSK and DBPSK modulation formats encode one bit per symbol, whereas multi-level modulation formats such as quadrature phase shift keying (QPSK), differential quadrature phase shift keying (DQPSK) and quadrature amplitude modulation (QAM) achieve more than one bit per symbol encoding [11]. These modulation
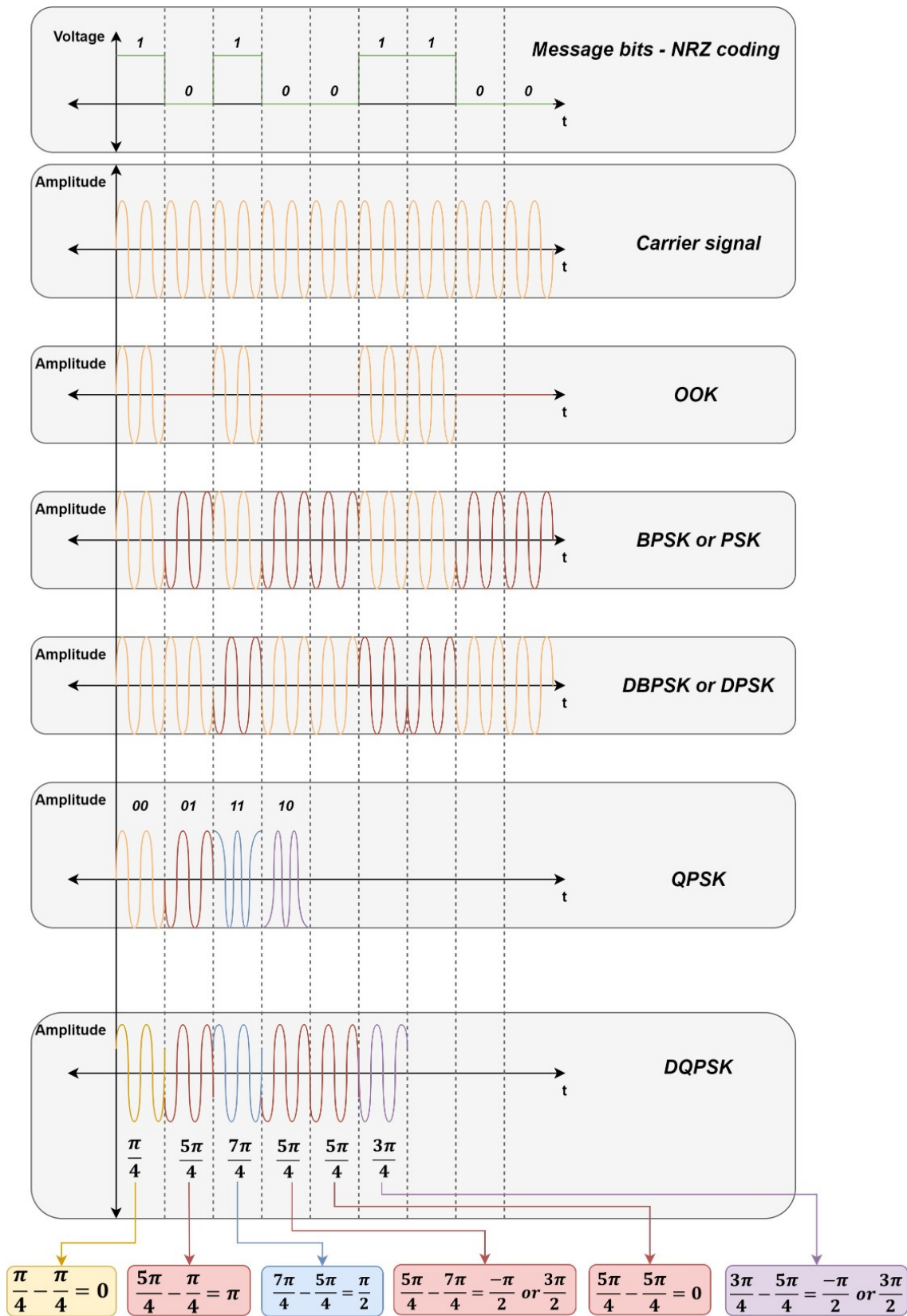
Figure 3: Optical modulation formats [9][10].

formats are considered as higher-order modulation as they have high spectral efficiency and allow high data rate transmission within a given bandwidth [11]. QPSK modulation uses four carrier phases to encode four symbols, each carrying two bits. On the other hand, in DQPSK modulation, the bits are coded to the phases of the carrier signal according to the differential bit mapping condition. This differential bit mapping involves the phase state of the previously transmitted symbol, the current symbol and the current message bits, and is discussed in detail in the chapter 4 [10]. Unlike in RF communication technology, these higher order modulation formats are not widely used and implemented in free-space optical communication, although their theoretical understanding is well defined.

2.1 Brief overview of noise in optical communication system

The performance efficiency of the system is determined by the error rate in the received bit stream, known as bit error rate. These errors are mainly caused by the noise in the system and the optical link. Noise in an optical communication system is defined as the deviation or unwanted signal from an ideal signal, which is usually associated with a random process. Thus, the noise in the system degrades the fidelity of the signal and alters the information. In an optical communication system, the noise signals are classified as the voltage noise, current noise and optical intensity noise [12].

Figure 4: Basic block diagram of an optical communication system [13].

Figure 4 shows the basic block diagram of an optical communication system, where the transmitter (Tx) consists of a light emitting laser diode, external electro-optic modulator and booster amplifier. In the receiver (Rx) there is a pre-amplifier, optical filter and photodiode. In this optical communication system, noise originates from different sources and these noise sources are classified as [12],

- Noise contribution from the transmitter.
- Noise contribution from the receiver.
- Noise contribution from the optical link or transmission channel.

2.1.1 Noise contribution from the transmitter

Noise sources at the transmitter due to optical components are from the laser and the Mach-Zehnder modulator (MZM). Other noise comes from the electronics that drive the laser and MZM due to the semiconductor noise, thermal noise and other external noise sources [12].

Laser Noise

In reality, the output of a semiconductor laser under a constant bias current is not stable. The output optical signal has a fluctuation in its intensity, phase and frequency due to the spontaneous emission of photons. The spontaneously emitted photons contribute a small random phase component to the coherent field originated by the simulated emission, which induces the randomness also in the amplitude and phase of the signal[8].

The output of an ideal monochromatic continuous wave (CW) laser is given by [8],

$$E_{cw}(t) = \sqrt{P} \cdot e^{j(\omega_c t + \varphi)} \cdot e_p \tag{2.1}$$

In the Equation 2.1, $\sqrt{P}$ is the power (normalized electric field amplitude) of the output signal, $\omega_c(t)$ is the carrier/center frequency, φ is the phase of the signal and e_p is the polarisation of the signal [11].

In practice, the output of the CW laser is not constant in intensity and phase. It can be represented as follows [14],

$$P = \overline{P} + \delta P(t) \tag{2.2}$$

$$\varphi = \varphi_0 + \varphi_n(t) \tag{2.3}$$

In the Equation 2.2, $\overline{P}$ is the average power value and $\delta P(t)$ is the fluctuating power with zero mean value. In the equation 2.3, φ_0 is the constant phase and $\varphi_n(t)$ is the variable phase. Therefore, the realistic laser output is given by substituting the equations 2.2 and 2.3 into the Equation 2.1[11]

$$E_{cw}(t) = \sqrt{\overline{P} + \delta P(t)} \cdot e^{j(\omega_c t + \varphi_0 + \varphi_n(t))} \cdot e_p \tag{2.4}$$

Relative Intensity Noise (RIN)

Intensity noise in the laser output is quantified by measuring its power fluctuation from the ideal value, which is represented as δP in Equation 2.2. The noise power is normalised to the average power by measuring the root mean square (rms) value and is represented as follows [14],

$$\delta P_{rms} = \sqrt{< (P(t) - \overline{P})^2 >} \qquad (2.5)$$

Where, δP_{rms} divided by $\overline{P}$ is called as the rms relative intensity noise (RIN).
The output power fluctuation can be slow or fast and its detection depends on the measurement device bandwidth. Therefore, higher frequency fluctuations cannot be measured with a slow detector and the limited measurement time window may not detect the slow fluctuations. To get an idea of the noise, we should look into its frequency spectrum. Therefore, the power spectral density (PSD) of the noise should be considered. The PSD of RIN is given as [14],

$$S_I(f) = \frac{2}{\overline{P}^2} \int_{-\infty}^{+\infty} < \delta P(t)\delta P(t + \tau) > e^{i2\Pi\tau} d\tau \qquad (2.6)$$

In the Equation 2.6, I represents RIN, factor 2 is because we only consider one-sided PSD, $<>$ represents the auto-correlation function. So, this equation is an auto-correlation function of the normalised power fluctuation. The unit of RIN PSD is Hz^{-1} , but is most commonly specified in decibel scale relative to the carrier in a 1 Hz noise bandwidth dBc/Hz [14].
The RMS value of RIN can be obtained by integrating the PSD over the frequency interval $[f_1, f_2]$ of noise, which is represented as follows [14],

$$\frac{\delta P_{rms}}{\overline{P}} = \sqrt{\int_{f_1}^{f_2} S_I(f) df} \qquad (2.7)$$

Phase Noise

The laser phase noise is a random phase fluctuation due to the spontaneous emission of photons and the change in carrier density. The actual phase can be understood as a random walk process in the time domain within the time interval τ, the spontaneous emission of photons can be modelled as a Gaussian distribution according to the central limit theorem [13].

The random phase change $\Delta\phi_n(t)$ is given by [11],

$$\Delta\phi_n(t) = \phi_n(t) - \phi_n(t - \tau) \qquad (2.8)$$

Assuming, that the frequency noise as a white power spectral density and by neglecting the intensity noise, the PSD of the optical field can be shown as a Lorentzian shaped spectrum. The Full Width at Half Maximum (FWHM) of this spectrum gives the line-width (Δf) of the laser. Δf quantifies the variance of the phase fluctuation ($\sigma_\phi(\tau)^2$) [11].

The phase error variance is given by,

$$\sigma_\phi(\tau)^2 = <\Delta\phi_n(t)^2> \qquad (2.9)$$

Therefore, the relationship between the phase error variance and the laser line-width is given by [13],

$$\sigma_\phi(\tau)^2 = 2\Pi\Delta f\tau \qquad (2.10)$$

MZM Noise

Ideally, MZM modulates the optical signal passing through it according to the appropriate bias conditions. However, in reality, the signal undergoes unwanted changes in frequency over a period of time, which is known as frequency chirping. Intensity modulation can be done directly by modulating the CW laser or by using a CW laser followed by an external modulator such as MZM [15]. The chirp effect is greater with direct modulation when compared to an external modulator. Therefore, external modulators are widely used in high-speed optical communication system. These external modulators are made of materials with strong electro-optic effect such as LiNbO$_3$ [16]. The chirp factor(α) is defined as the ratio between phase modulation and intensity modulation [15].

$$\alpha = 2I\frac{d\phi/dt}{dI/dt} \qquad (2.11)$$

Chirp parameter with respect to extinction ratio

In an ideal MZM with a 3 dB splitter/combiner and equal optical power loss in both arms, the extinction ratio is infinite. If the splitter/combiner ratio is not 50:50 and the optical power loss is not equal in both arms, then the MZM operates with a finite extinction ratio [15].

Assuming that the two RF drive voltage signals of the MZM as $v_1(t) = V_1\sin(\omega_{rf}t)$

and $v_2(t) = V_2 \sin(\omega_{rf}t)$. One of the arms is also biased with DC voltage $V_b \cdot \gamma_{opt}$ is the scaling factor between 0 and 1 for the asymmetrical device, it can be represented as follows [15],

$$\gamma_{opt} = \frac{\sqrt{\varepsilon} - 1}{\sqrt{\varepsilon} + 1} \tag{2.12}$$

ε in the Equation 2.12 is the extinction ratio of the MZM.

The chirp factor is a function of the relative amplitude of the two RF drive voltage signals, the DC bias voltage and the extinction ratio. Therefore, the chirp parameter of an ideal MZM with infinite extinction ratio ($\gamma_{opt} = 1$) in small-signal regime is given as [15],

$$\alpha_{IdealMZM} = \frac{V_1 + V_2}{V_1 - V_2} \cot(\frac{\Pi}{2V_\Pi}((V_1 - V_2)\sin \omega t - V_b) \tag{2.13}$$

The chirp parameter of MZM with finite extinction ratio in the small-signal regime is given by [15],

$$\alpha_{MZM} = \frac{V_1 + \gamma_{opt}^2 V_2}{\gamma_{opt}(V_1 - V_2)} \tag{2.14}$$

In the ideal case $\gamma_{opt} = 1$, then the equation 2.14 becomes

$$\alpha_{MZM} = \frac{V_1 + V_2}{V_1 - V_2} \tag{2.15}$$

Therefore, from the above chirp equations it is clear that the extinction ratio affects the signal by inducing unwanted frequency modulation (i.e. noise). Hence, the external modulators in high-speed optical communication system should be operated under minimum chirp conditions by appropriately tuning the RF drive voltages, DC bias voltage and its extinction ratio [15].

2.1.2 Noise contribution from the receiver
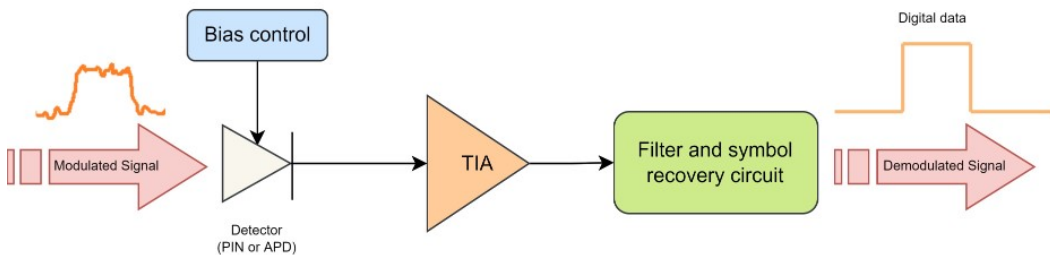
Figure 5: Basic block diagram of optical receiver [13].

Figure 5, shows the basic block diagram of the optical receiver where the modulated signal is received by the photodetector and the corresponding photocurrent(I_p) is produced at the photodetector output. Then the photocurrent(I_p) is processed by low noise trans-impedance amplifier(TIA) with a certain gain and converts the current signal into voltage signal, finally high-frequency electrical noise is filtered using filter circuit and the symbols are recovered from the voltage signal using decision making circuit in symbol recovery circuit. Thus, the received signal is demodulated and the digital data stream (i.e. information bits) is obtained [13].

Noise in this type of direct detection receiver causes fluctuations in the photocurrent, resulting in errors in the demodulated bit stream. The fundamental noise mechanisms involved in the photo current fluctuations are thermal noise and shot noise [13].

Thermal Noise

The load resistor R_L in the receiver front-end induces fluctuations in the photocurrent due to the random motion of the electrons at a finite temperature. This noise is known as thermal noise, Johnson noise or Nyquist noise. The photocurrent generated by the photodiode is given as [8],

$$I(t) = I_P + i_T(t) \tag{2.16}$$

In the Equation 2.16, $I_P = R_d P_{in}$(R_d is responsivity of the photodiode, P_{in} is the input optical power to the photodiode) represents the average current and i_T is a current fluctuation due to thermal noise.

The thermal noise is modelled as a stationary Gaussian random process with frequency independent (up to$\approx$1 THz) spectral density and is given by [8],

$$S_T(f) = \frac{2k_B T}{R_L} \tag{2.17}$$

The above Equation 2.17 is given for a two-sided spectral density $(S_T(f))$, where k_B is the Boltzmann constant, T is the temperature and R_L is the load resistance. Therefore, the variance of thermal noise $(\sigma_T{}^2)$ is obtained by using the auto-correlation function and is given as [8],

$$\sigma_T{}^2 = <i_T{}^2(t)> = \int_{-\infty}^{+\infty} S_T(f)df = \frac{4k_B T}{R_L}\Delta f \tag{2.18}$$

where Δf is the effective noise bandwidth. Also, $\sigma_T{}^2$ does not depends on the average photocurrent I_P.

The thermal noise due to the various resistors used the pre-amplifier and main amplifiers can be included in the above Equation 2.18 by specifying their noise figure (F_n) and given as [8],

$$\sigma_T{}^2 = \frac{4k_B T}{R_L} F_n \Delta f \tag{2.19}$$

Shot Noise

Fluctuations in the photodetector due to the generation of a stream of electrons at random times are known as shot noise. The shot noise current $(i_s(t))$ is a stationary random process with Poisson statistics and often approximated by Gaussian statistics. Its spectral density $S_s(f)$ is related to the shot noise by the Wiener-Khinchin theorem and is given by [8],

$$< i_s(t) i_s(t+\tau) > = \int_{-\infty}^{+\infty} S_s(f) e^{2\Pi f \tau} df \tag{2.20}$$

The shot noise variance $(\sigma_s{}^2)$ for a one-sided spectral density is given as,

$$\sigma_s{}^2 = < i_s{}^2(t) > = \int_{-\infty}^{+\infty} S_s(f) df = 2q I_P \Delta f \tag{2.21}$$

Where, in the Equation 2.21 $q I_P$ is a constant amplitude of the white noise and Δf is the effective noise bandwidth.

Dark current (I_d) is described as the current generated at the photodiode due to thermal radiation and straylight without any incident optical signal. Since the dark current of the photodetector also generates the shot noise, it should also be included in the Equation 2.21 and given as [8],

$$\sigma_s{}^2 = 2q(I_P + I_d)\Delta f \tag{2.22}$$

The receiver system also has other circuits such as decision circuits, pre-amplifier, low pass filter that generates shot noise. In this case, their transfer function should be included in the above Equation 2.22 [8].

From the Equation 2.19 and 2.22, the total variance of current fluctuation due to

the thermal noise and the shot noise can be given as [8],

$$\sigma^2 = << \Delta I^2 >> = {\sigma_s}^2 + {\sigma_T}^2 = 2q(I_P + I_d)\Delta f + \frac{4k_B T}{R_L}F_n \Delta f \qquad (2.23)$$

Optical Amplifier Noise

The main source of noise in an Erbium Doped Fiber Amplifier (EDFA) is amplified spontaneous emission (ASE) noise. ASE noise is generated by the amplification of spontaneously emitted photons of entire band by the amplifier. The electric field output ($E_{out}(t)$) of EDFA is given by [13],

$$E_{out}(t) = \sqrt{G}E_{in}(t) + n(t) \qquad (2.24)$$

where G is the gain of the amplifier relative to the power and $n(t)$ is the noise added by the amplifier. The ASE noise outside the signal band can be removed using an ASE filter with signal bandwidth. ASE noise is quantified using the PSD of ASE noise(ρ_{ASE}) and its unit is watts per hertz (W/Hz).

$$\rho_{ASE} = 2n_{sp}h\nu(G - 1) \qquad (2.25)$$

In the Equation 2.25, n_{sp} is the spontaneous emission factor and $h\nu$ is the photon energy. n_{sp} is given as [13],

$$n_{sp} = \frac{N_2}{N_2 - N_1} \qquad (2.26)$$

where N_1 and N_2 are population densities of ions in higher and lower energy states. Therefore, the total optical ASE noise power of the EDFA is given by multiplying the Equation 2.25 by the signal bandwidth (B) [13].

$$\rho_{ASE} = 2n_{sp}h\nu(G - 1)B \qquad (2.27)$$

At the detector, this optical ASE noise is converted into electrical ASE noise. So, it is important to understand its electrical characteristics. The photocurrent generated at the detector is now given as [13],

$$I_P = R_D P_{in} = R_D|E_{sig} + E_n|^2 \qquad (2.28)$$

where E_{sig} is the signal field and E_n is the ASE noise field. They are given as follows [13],

$$E_{sig}(f) = \sqrt{P_{sig}}e^{j2\Pi ft} \qquad (2.29)$$

$$E_n(f + \Delta f) = \sqrt{\rho_{ASE(f+\Delta f)}}e^{j2\Pi(f+\Delta f)t} \tag{2.30}$$

where f is the center frequency around which the optical signal exists with the bandwidth of B_0. Inside the optical bandwidth(B_0), a small area at a distance of Δf from f is considered for the calculation of the ASE noise as shown in Figure 6 [13]. Therefore the Equations 2.29 and 2.30 are substituted in the Equation 2.28.
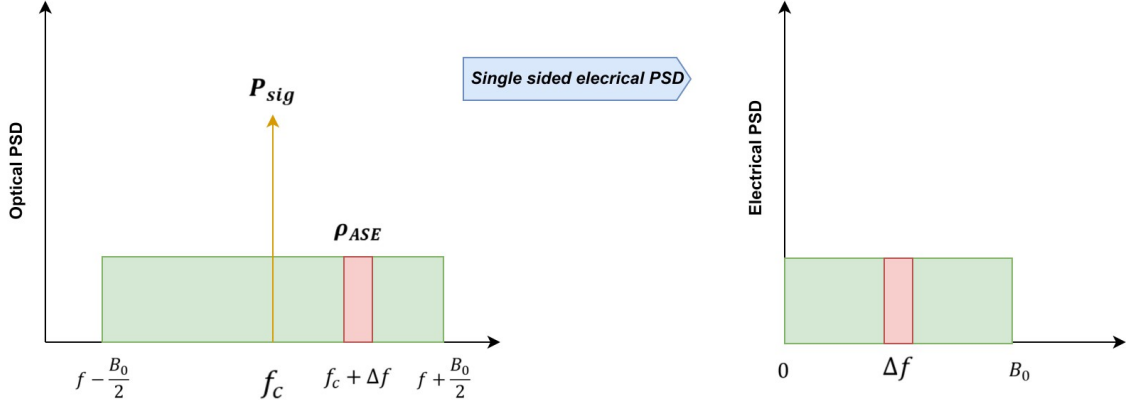
Figure 6: Frequency spectrum of ASE noise in optical and electrical domain [13].

$$I_P = \left|\sqrt{P_{sig}}e^{j2\Pi ft} + \sqrt{\rho_{ASE(f+\Delta f)}}e^{j2\Pi(f+\Delta f)t}\right|^2 \tag{2.31}$$

By expanding the Equation 2.31, the signal beat is obtained with itself $(Sig - Sig)$ component, $ASE - ASE$ beat component and $Sig - ASE$ beat component [8][13]. So, in addition to the message component in a received signal, it also has two noise components. Since the signal has higher power, $Sig - ASE$ noise contribution is larger compared to $ASE - ASE$ noise. So, $ASE - ASE$ noise component can usually be ignored [13]. Therefore, I_P at Δf is given as,

$$I_P(\Delta f) = R_D[2\sqrt{P_{sig}\rho_{ASE}(\Delta f)}cos(2\Pi ft)] \tag{2.32}$$

So, the power of the Sig-ASE beat noise is calculated by squaring the current in above the Equation 2.32 and given as [13],

$$Average power = 2R_D{}^2P_{sig}\rho_{ASE} \tag{2.33}$$

To estimate the PSD of $Sig - ASE$ beat noise, the ASE contribution from both sides of the spectrum should be taken into account, which can be done by doubling the ASE noise component [13]. The noise polarization could be random, so the polarisation overestimation factor of $\frac{1}{2}$ should be considered [13].

Therefore, the PSD of the Sig-ASE beat noise in the electrical domain is given as [8][13],

$$2R_D{}^2 P_{sig} \rho_{ASE} * 2 * \frac{1}{2} = 2R_D{}^2 P_{sig} \rho_{ASE} \qquad (2.34)$$

In practice, EDFA noise is quantified using the noise figure (NF), also denoted as F_n and its unit is in dB. F_n is defined as the ratio of the input signal-to-noise ratio(SNR) to the output SNR of the EDFA. The SNR is used to quantify the performance of the system which will be discussed later in this chapter. We already know the noise contribution of the EDFA and the receiver, so the noise figure F_n is given as [8],

$$F_n = \frac{1}{G} + \frac{2\eta n_{sp}(G-1)}{G} \qquad (2.35)$$

Where η is the quantum efficiency of the detector. The photodetector considered here is of the p-i-n type.

2.1.3 Noise contribution from the optical link/channel

In the FSO link, the signal traversing through it will experience atmospheric effects such as attenuation, radiation, turbulence and scattering which will introduce loss and noise in the system [1].

Atmospheric attenuation occurs due to the atomic and molecular absorption of the signal by particles present along the channel such as precipitation. Atmospheric turbulence induces fluctuations in the refractive index, causing beam deflection(jitter) and phase degradation. The temporal and spatial variation in signal intensity caused by atmospheric turbulence is known as scintillation. The scintillation effect impacts the Bit-Error-Rate (BER) performance on the millisecond time scale and it increases along the distance drastically [17].

Atmospheric radiance or background noise is the main source of FSO channel noise. These noises are usually modelled as white, Gaussian and single independent noise with Poisson random distribution. The FSO background noise affects the signal according to the atmospheric conditions. Therefore, the mathematical model of the FSO channel is classified into weak, moderate and strong turbulence channels and their model functions can be referred in [17].

In this thesis, the channel characteristics such as free space loss, scintillation margin, atmospheric attenuation, etc... are based on scenarios described in *"Optical technologies for very high throughput satellite communications"* [1].

2.2 Performance metrics of optical communication system

The performance of an optical communication system depends on signal-to-noise ratio (SNR), bit error rate (BER) and receiver sensitivity [8][13]. These metrics varies according to the system characteristics such as modulation format and receiver type [8][13]. Therefore understanding the type of receivers is essential. In this thesis we investigated and evaluated direct detection(DD) and coherent receivers.

2.2.1 Performance quantification of direct detection receiver

As mentioned earlier in this chapter, we consider the *p-i-n* type photodetector. In this type of direct detection receiver, only the intensity of the signal can be detected, so only Amplitude shift keying(ASK) or On-Off keying(OOK) modulation formats can be demodulated. On the other hand, the phase modulated data can be demodulated in the DD receiver with delay line demodulation technique by differential encoding the phase information (DPSK) to the carrier signal [8].

At the receiver, any electrical signal SNR is defined as [8][13],

$$SNR = \frac{average signal power}{noise power} = \frac{I_P{}^2}{\sigma^2} \tag{2.36}$$

We know that the noise variance of the shot and thermal noise from the Equation 2.23 and the signal power is square of I_P. Therefore, the optical SNR is given as [13],

$$SNR = \frac{R_D{}^2 P_{in}{}^2}{2q(I_P + I_d)\Delta f + \frac{4k_B T}{R_L}F_n\Delta f} \tag{2.37}$$

In the case of a thermal noise limited system, the SNR is given as,

$$SNR = \frac{R_d{}^2 P_{in}{}^2}{4k_B T F_n \Delta f}R_L \tag{2.38}$$

Therefore, the SNR in a thermal noise-limited system can be improved by increasing the signal power P_{in} and the load impedance(R_L) in the receiver front-end. Thermal noise is quantified by noise-equivalent power(NEP) or detectivity(NEP^{-1}), which is the minimum power per unit bandwidth required to produce SNR=1. Its unit is $W/\sqrt{Hz}$ [13].

In the case of a shot noise limited system, the SNR is given as [13],

$$SNR = \frac{R_D{}^2 P_{in}{}^2}{2q(I_P + I_d)\Delta f} \tag{2.39}$$

Substituting $R_d = \frac{\eta q}{h\nu}$ and P_{in} in terms of *bit energy/bit rate* the Equation 2.39 becomes [13],

$$SNR = \frac{\eta N_p B}{2\Delta f} \qquad (2.40)$$

where N_p is the number of photons and B is the bit rate. It is evident from the above equation that by increasing the signal power the shot noise also increases. Therefore, the improvement in thermal noise by increasing the signal power is limited. To overcome this problem coherent detection is used, where the local oscillator (LO) field is beaten coherently onto the received signal field [13].

2.2.2 Performance quantification of coherent detection receiver

This detection technique is employed in modulation formats such as binary phase shift keying, quadrature phase shift keying, etc..., since the phase information is demodulated by combining the local oscillator field with the signal field and converting them into equivalent amplitudes. The working principle of coherent detection is shown in the Figure 7 [8].

Therefore, the output of the coherent receiver is the mixed signal of received E_{Sig}
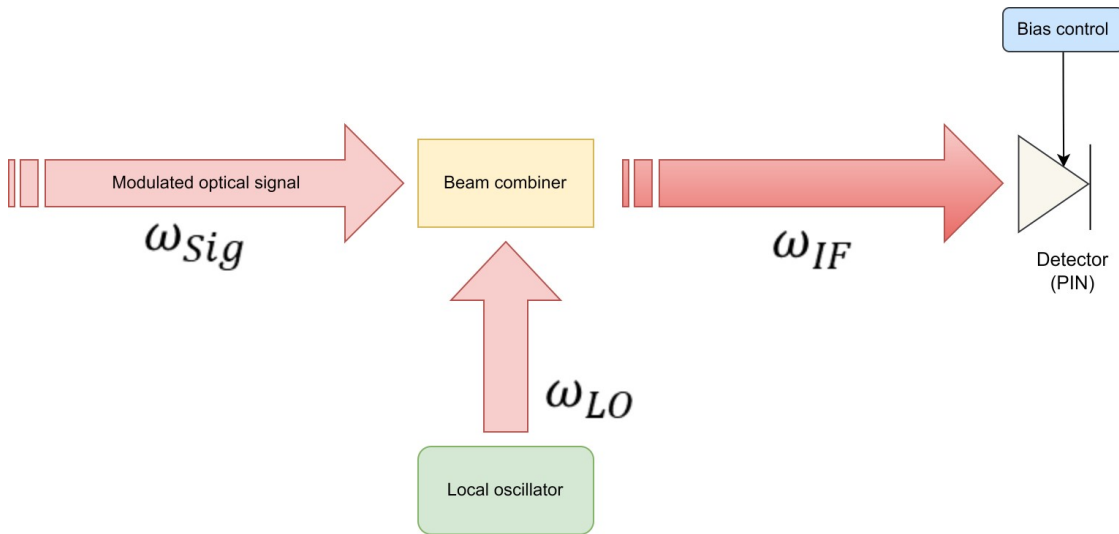
Figure 7: Working principle of coherent detector [8][13].

and LO signals E_{LO} field at an intermediate frequency (ω_{IF}) which is given by [8][13],

$$E_{Sig} = A_{Sig}e^{j(\omega_{Sig}t+\phi_{Sig})} \qquad (2.41)$$

$$E_{LO} = A_{LO}e^{j(\omega_{LO}t+\phi_{LO})} \qquad (2.42)$$

By squaring and combining the above fields with the photodetector responsivity (R_d) we obtain the photocurrent (I_P) incident on the detector. Which is given by [8],

$$I_P(t) = R_d(P_{Sig} + P_{LO} + 2\sqrt{P_{Sig}P_{LO}}cos(\omega_{IF}t + \phi_{Sig} - \phi_{LO})) \qquad (2.43)$$

Where, $P_{Sig} = A_{Sig}{}^2$, $P_{LO} = A_{LO}{}^2$ and $\omega_{IF} = \omega_{Sig} - \omega_{LO}$. P_{Sig} and P_{LO} are the DC components of the signal.

If $\omega_{IF} = 0$, then the signal frequency and LO oscillator frequency are synchronised such system is known as a homodyne detection system, if $\omega_{IF} \neq 0$ is known as a heterodyne detection system [8]. We are only interested in the signal component rather than the DC component. The phase of the signal and local oscillator is considered to be equal, which is achieved using a phase-locked loop [8][13].

Homodyne detector

The photocurrent of the homodyne detector is given as [8][13],

$$I_P(t) = 2R_d\sqrt{P_{Sig}P_{LO}}) \qquad (2.44)$$

So the average output power ($< I_P{}^2 >$) is,

$$< I_P{}^2(t) >= 4R_d{}^2\overline{P_{Sig}}P_{LO} \qquad (2.45)$$

Where, $\overline{P_{Sig}}$ is the average signal power. We know that the signal power of the DD receiver is $R_d{}^2 P_{Sig}{}^2$, then the improvement of the heterodyne detector over DD is given by [8][13],

$$\frac{4R_d{}^2\overline{P_{Sig}}P_{LO}}{R_d{}^2 P_{Sig}{}^2} = \frac{4P_{LO}}{P_{Sig}} \qquad (2.46)$$

Noise is the coherent detectors are considered to be in shot noise regime since the power of the local oscillator is more than the received signal power(i.e. dark current$I_d << R_dP_{LO}$, so it can be ignored). Hence the SNR of the homodyne detector in shot noise regime is given as,

$$SNR_{homodyne} = \frac{4R_d{}^2\overline{P_{Sig}}P_{LO}}{2qR_dP_{LO}\Delta f} \qquad (2.47)$$

We know that $R_d = \frac{\eta q}{h\nu}$,

$$SNR_{homodyne} = \frac{2\eta\overline{P_{Sig}}P_{LO}}{h\nu\Delta f} \qquad (2.48)$$

Hetrodyne detector

The average output power of the hetrodyne receiver is given by [8][13],

$$< I_P{}^2(t) >= 2R_d{}^2\overline{P_{Sig}}P_{LO} \tag{2.49}$$

Where the average of $cos^2\theta = 1/2$. Therefore, the improvement of the hetrodyne receiver over the DD receiver is,

$$\frac{2R_d{}^2\overline{P_{Sig}}P_{LO}}{R_d{}^2{P_{Sig}}^2} = \frac{2P_{LO}}{\overline{P_{Sig}}} \tag{2.50}$$

From the Equation 2.45 and 2.49 it is clear that the homodyne detector output has twice the signal power than the hetrodyne detector which is 3 dB higher [13]. The SNR of the hetrodyne detector in the shot noise regime is given as,

$$SNR_{hetrodyne} = \frac{2R_d{}^2\overline{P_{Sig}}P_{LO}}{2qR_dP_{LO}\Delta f} \tag{2.51}$$

We know that $R_d = \frac{\eta q}{h\nu}$,

$$SNR_{hetrodyne} = \frac{\eta\overline{P_{Sig}}P_{LO}}{h\nu\Delta f} \tag{2.52}$$

From the Equation 2.48 and 2.52, it is clear that the homodyne detector has a 3 dB benefit in SNR compared to the hetrodyne system, which also implies that the homodyne system has a 6 dB improvement in SNR compared to the DD receiver [13].

2.2.3 Bit Error Rate (BER) and Sensitivity

BER is defined as the probability of incorrect identification of a bit by the decision circuit of the receiver. The receiver makes a mistake in identifying the voltage levels of bits '1' and '0' due to the noise added to the received signal by the system and the channel. The commonly used BER criterion in communication system is less than $1E - 9$ [8]. The minimum average optical power required at the receiver to operate at $1E - 9$ BER is known as the sensitivity of the receiver. The BER of a thermal noise limited, OOK system with equal probability of transmitting '1' and '0' is given as [8],

$$BER = \frac{1}{2}erfc(\frac{Q}{\sqrt{2}}) \tag{2.53}$$

where $erfc$ is the complementary error function and Q is the quality factor. The quality factor Q is given as,

$$Q = \frac{I_1 - I_0}{\sigma_0 + \sigma_1} \tag{2.54}$$

Where, I_1 and σ_1 are the intensity and standard deviation of the optical noise probability density function (PDF) corresponding to bit '1' respectively. I_0 and σ_0 correspond to bit '0'. The PDFs are assumed to be Gaussian.

The sensitivity of the receiver(i.e. the average power of the receiver($\overline{P}$)) under the thermal noise limited condition is given by [8],

$$\overline{P} = \frac{Q\sqrt{\sigma_t{}^2}}{R_d} \tag{2.55}$$

Where, σ_t is the thermal noise standard deviation. Under the condition of $I_0 = 0$, SNR is related to the Q factor as $SNR = Q^2$. Therefore, BER can be expressed in terms of average number of photons(N_p) and quantum efficiency(η) as [8],

$$BER = \frac{1}{2}erfc(\sqrt{\frac{\eta N_p}{2}}) \tag{2.56}$$

In the shot noise limited condition, the noise variance should be considered as Poisson distribution since the photon arrival statistics is a Poisson random process. Its BER and sensitivity ($\overline{P}$) are given as [8],

$$BER = \frac{1}{2}e^{-N_p} \tag{2.57}$$

$$\overline{P} = \overline{N_p}h\nu B \tag{2.58}$$

Where, B is the bit rate and $\overline{N_p}$ is the average number of photons/bit when '0' bits carry no energy(i.e.$\overline{N_p} = N_p/2$).

The BER of BPSK and QPSK coherent detection (i.e. shot noise limited) is given as [18],

$$BER_{BPSK} = BER_{QPSK} = \frac{1}{2}erfc(\gamma_b) \tag{2.59}$$

Where, $\gamma_b = E_b/N_0$ The BER of M-ary PSK and M-QAM coherent detection is approximated as follows

$$BER_{PSK}(M) = \frac{1}{b}erfc(\sqrt{b\gamma_b}sin\frac{\pi}{M}) \tag{2.60}$$

$$BER_{QAM}(M) = \frac{2}{b}erfc(\sqrt{\frac{3b\gamma_b}{2(M-1)}}) \tag{2.61}$$

Where, M is the modulation order.

Table 1 shows the BER estimation for different modulation formats with respect to quality factor Q [8]. The receivers mentioned in this table are synchronous receivers (i.e. the phase difference between the signal and the local oscillator is 0), where BER for homodyne receivers are two times better than heterodyne receivers and synchronous PSK system has the best BER compared to ASK, frequency shift keying (FSK) and DPSK receivers [18].

Table 1: Lower order modulation format BER estimation [8].

	2-PSK homodyne	Sync-PSK heterodyne	Sync-ASK homoodyne	Sync-ASK heterodyne	Sync-FSK	DPSK
BER	$Q(\sqrt{4\gamma_b})$	$Q(\sqrt{2\gamma_b})$	$Q(\sqrt{\gamma_b})$	$Q(\sqrt{\gamma_b/2})$	$Q(\sqrt{\gamma_b/2})$	$(1/2)e^{(-\gamma_b)}$

The BER of the DQPSK format implemented with gray code is estimated using *Marcum's Q function* (Q_1) and given as [8],

$$BER_{DQPSK} = Q_1(a,b) - \frac{1}{2}I_0(ab)exp[-\frac{1}{2}(a^2+b^2)] \tag{2.62}$$

Where, $a = \sqrt{[\eta N_p(2-\sqrt{2})]}$ and $b = \sqrt{[\eta N_p(2+\sqrt{2})]}$

2.3 Comparison of 100G technologies

In order to achieve 100 Gbps data rates, higher order optical modulation formats should be used, which allows to efficiently access the spectrum grid. The following Table 2 is constructed by referring to available commercial optical communication systems and theoretical understanding according to the Key Performance Indicators (KPIs) such as coding efficiency, baud rate, BER, SNR, spectral efficiency and system complexity [19][20][21][22][23][24].

Table 2: Comparison of 100G technologies.

Modulation Formats KPI		OOK	BPSK	DBPSK	4-PAM	QPSK	DQPSK	DP-DQPSK	DP-QPSK	QAM
Must	Coding efficiency (bits/symbol) [21]	1	1	1	2	2	2	2*2	2*2	4
	Baud Rate (symbols/second) [21]	100G	100G	100G	50G	50G	50G	25G*25G	25G*25G	25G
	Spectral Grid occupancy(GHz), NRZ [21]	200	200	200	100	100	100	50	50	50
	Spectral Effeciency (bits/s/Hz) [21]	0.5	0.5	0.5	1	1	1	2	2	2
Should	BER/SNR at 1E-04 [19][20]	18dB	8.4dB	10.5dB	24dB	8.8dB	11dB	11dB	8.8dB	18dB
	BER/SNR at 1E-09 [19][20]	21dB	12dB	15.5dB	29dB	12.5dB	13dB	13dB	12.5dB	22dB
	Coh/nonCoh Rx [21]	Non-Coh	Coh	Non-Coh	Non-Coh	Coh	Non-Coh	Non-Coh	Coh	Coh
	complexity [21]	Less	Moderate	Less	Moderate	Moderate	Moderate	Complex	Complex	Highly complex
Could	No. Modulators	1MZI	1MZI	1MZI	1MZI	1IQ	1IQ	2*2IQ	2*2IQ	2IQ
	No. Laser	1	2	1	1	2	1	1	2	2
	No. PD	1	2	2	1	4	4	8	8	4

	Good
	Better
	Bad

In the Table 2, the KPIs for 100 Gbps optical communication system are categorised as *Must, Should, Could* according to the system design priorities. The priorities are set according to the understanding of the 100G system requirements and the performance quantification of the optical communication system from the previous section.

In the case of coding efficiency, multi-level modulation formats such as 4-PAM, QPSK and DQPSK encode two bits per symbol each. Whereas, dual polarisation modulation formats DP-QPSK and DP-DQPSK encode 2 bits per symbol in both X and Y polarisation each. However, QAM modulation format also has best coding efficiency of 4 bits per symbol. On the contrary other modulation formats such as OOK, BPSK and DBPSK has comparatively poor coding efficiency of 1 bit per symbol each.

It is also observed that QAM, DP-QPSK and DP-DQPSK modulation formats have an effective baud rate of 25 GBd baud each. On the other hand, 4-PAM, QPSK and DQPSK have a better baud rate of 50 GBd each. While OOK, BPSK and DBPSK modulation formats have comparatively ineffective baud rate of 100 GBd each.

In terms of spectral occupancy DP-QPSK, DP-DQPSK and QAM modulation formats occupies only 50 GHz of spectrum which is within the allocated bandwidth of 100 GHz according to the International Telecommunication Union(ITU) standard. Likewise, 4-PAM, QPSK and DQPSK occupies 100 GHz bandwidth which is also feasible. Whereas, other modulation formats such as OOK, BPSK and DBPSK requires larger bandwidth which makes channel more susceptible to cross-talk with neighbouring channels.

Since the BER and SNR quantify the performance of the system, these metrics are categorised under *should* parameters. The system with good BER to SNR value should be prioritised. Typically, the BER criterion in a communication system is in the range of 1E-9 and 1E-15 after forward error correction (FEC) encoding. Likewise, 1E-3 before FEC decoding is applied.

Other system performance metrics are based on the physical hardware and its implementation, which has more flexibility because it could be chosen and adapted with some restrictions. Therefore, these metrics are categorised as *could* parameters.

From the Table 2, it can be said that the OOK and DBPSK systems have simple physical system compared to other systems. Whereas, BPSK, 4-PAM, QPSK and DQPSK have moderate system complexity with coherent, non-coherent, coherent and non-coherent receiver setup respectively. Likewise, DP-QPSK and DP-DQPSK system requires coherent and non coherent receivers with additional components due to dual polarisation. On the contrary, QAM system has good performance in other metrics, but suffers from very high system implementation complexity. As a result, QAM systems are very difficult to design and execute.

It is evident that QAM, DP-QPSK and DP-DQPSK systems have overall good performance. But, QAM system SNR is difficult to achieve and its system architecture is comparatively highly complex to design and implement which makes DP-QPSK and DP-DQPSK systems advantageous from system designer's perspective.

From the Table 2, it can be concluded that DP-QPSK system has promising performance in all aspects comparatively for 100G system. Followed by DP-DQPSK system with the advantage of lower receiver complexity. Therefore, the performance of DP-QPSK and DP-DQPSK system for 100 Gbps data rate is further analysed and their PIC layout is designed according to the foundry description in the following chapters of this thesis.

3 100G DP-QPSK System

3.1 Theoretical overview on DP-QPSK Modulation

In dual polarisation - quadrature phase shift keying (DP-QPSK) system, information bits are encoded into four different phases of the laser electric field on both horizontally and vertically polarised photons.

In general, the QPSK signal is generated by modulating the message/information bits to the in-phase and quadrature of the carrier signal. As a result, the message bits are encoded into four different phases of the carrier signal each representing two message bits. In other words, four symbols represent four different phases of the carrier, each symbol carries two bits. In higher-order systems, the transmission rate is usually expressed as the symbol rate and its unit is given in Baud. As mentioned in the previous chapter, the baud rate of 100 Gbps DP-QPSK system in X and Y polarisation is 25 Gbaud.

The carrier signal($x(t)$) is given as [10],

$$x(t) = A\cos(2\pi f_c t + \theta(k)), kT \leq t \leq (k+T) \tag{3.1}$$

Where, A is the amplitude, f_c is the center frequency, θ is the phase of the carrier and $kT \leq t \leq (k+T)$ is the symbol time interval. Suppose m_I and m_Q are the message bits encoded in the in-phase and quadrature phases of the carrier, respectively. Then the phase state of the QPSK signal is represented as follows [10],

$$\theta(t) = \begin{cases} \frac{\pi}{4} & if(m_I(K), m_Q(K)) = (0,0) \\ \frac{3\pi}{4} & if(m_I(K), m_Q(K)) = (1,0) \\ \frac{5\pi}{4} & if(m_I(K), m_Q(K)) = (1,1) \\ \frac{7\pi}{4} & if(m_I(K), m_Q(K)) = (0,1) \end{cases} \tag{3.2}$$

The above representation of bits to their corresponding phases is also known as bit mapping and it is visually represented as a constellation diagram as shown in Figure 8 [10].
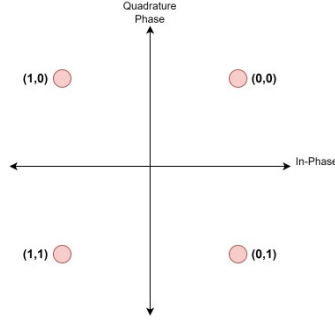
Figure 8: QPSK constellation diagram [10].

3.1.1 DP-QPSK Transmitter

In an optical communication system, QPSK modulation is implemented using an IQ modulator. The IQ modulator consists of two MZMs and a phase shifter with splitter and combiner as shown in Figure 9. The drive voltages $V_I(t)$ and $V_Q(t)$ of two MZMs are configured and biased at the appropriate operating point so that the above mentioned bit mapping condition is satisfied. The MZM on the upper branch corresponds to in-phase modulation and the MZM with 90° phase shifter branch corresponds to quadrature phase modulation [13].

The transfer function of the MZM is given by,

$$E_{out} = E_{in}\cos(\pi V(t)/V_\pi) \qquad (3.3)$$

Where, E_{in} and E_{out} are the input and output optical signal fields of the MZMs, $V(t)$ is the drive voltage signal or control signal of the MZM and V_π is the voltage required for a π rad phase shift in the signal passing through it. Therefore, the output of the QPSK modulator is given as,

$$E_{out} = E_{in}(\cos(\pi V_I(t)/V_\pi) + \cos(\pi V_Q(t)/V_\pi)e^{j\pi/2} \qquad (3.4)$$

$$E_{out} = E_{in}\sqrt{(\cos^2(\pi V_I(t)/V_\pi) + \cos^2(\pi V_Q(t)/V_\pi))}e^{j\tan^{-1}\left(\frac{\cos(\pi V_Q(t)/V_\pi)}{\cos(\pi V_I(t)/V_\pi)}\right)} \qquad (3.5)$$
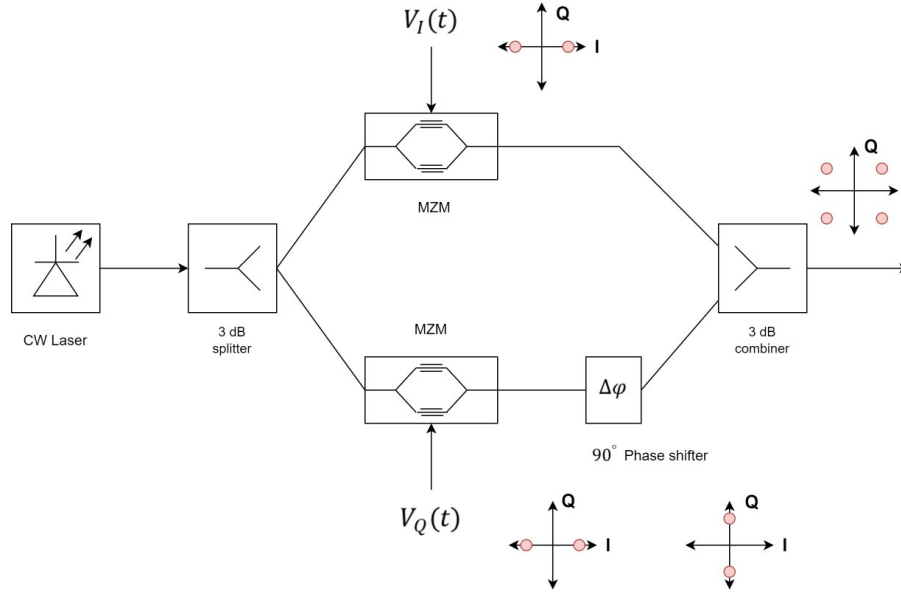
Figure 9: QPSK transmitter [13].

To achieve QPSK modulation $V_I(t)$ and $V_Q(t)$ should be 0 or V_π. Then the phase shift introduced on the input signal E_{in} is shown in the Table 3.

Table 3: QPSK Modulation [8].

$V_I(t)$	$V_Q(t)$	$\cos(\pi V_I(t)/V_\pi)$	$\cos(\pi V_Q(t)/V_\pi)$	$\tan^{-1}\frac{\cos(\pi V_Q(t)/V_\pi)}{\cos(\pi V_I(t)/V_\pi)}$
0	0	1	1	$\pi/4$
0	V_π	1	-1	$-\pi/4$
V_π	0	-1	1	$3\pi/4$
V_π	V_π	-1	-1	$5\pi/4$

Therefore, DP-QPSK transmission is achieved by simultaneously using two QPSK modulators for the dual polarisation optical carrier. Figure 10 shows the DP-QPSK transmitter setup, where the X and Y polarisations are handled by polarisation beam combiner (PBC) and polarisation beam splitter (PBS).

3.1.2 DP-QPSK Receiver

The QPSK signal is demodulated using the coherent detection technique, where the phase information is obtained by beating the received signal with the local oscillator. Demodulation is performed by a quadrature coherent detector consisting of a 90° optical hybrid and a set of balanced photodetector (BPD) as shown in
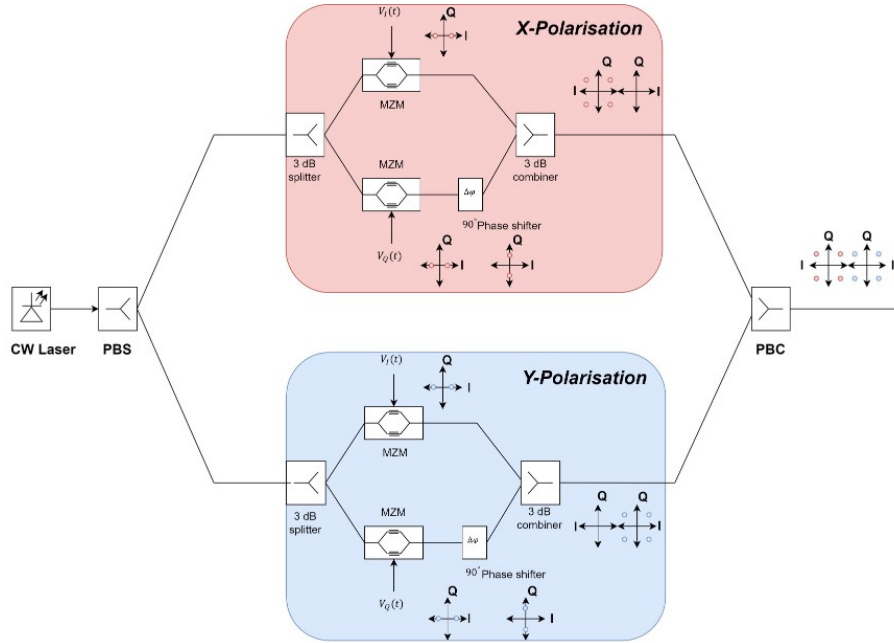
Figure 10: DP-QPSK transmitter [13].

Figure 11. The balance detection technique removes the DC component of the signal without filtering and improves OSNR tolerance [13]. The 90° optical hybrid is built using multi-mode interferometer (MMI) based 2x2 optical couplers and a phase shifter. Polarisation controllers (PCs) are used to maintain the precise polarisation alignment between the received signal and the local oscillator. After BPD, the electrical analog signal is converted to digital by analog to digital converter (ADC) and post-processed by digital signal processing (DSP) [13].
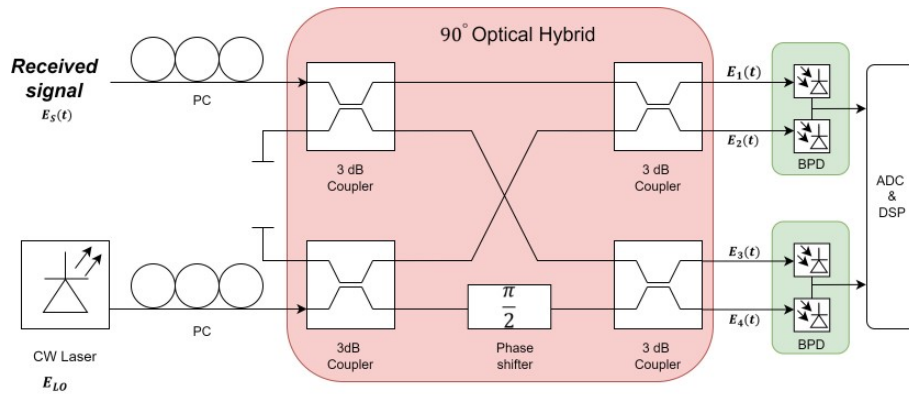
Figure 11: Quadrature coherent detector [13]

Where, $E_S(t)$ and E_{LO} are the received signal field and the local oscillator field. $E_1(t), E_2(t), E_3(t)$ and $E_4(t)$ are the output electric field of the 90° optical hybrid. The output of the 90° optical hybrid is given by [13],

$$\begin{bmatrix} E_1(t) \\ E_2(t) \end{bmatrix} = \frac{1}{\sqrt{2}} \begin{bmatrix} 1 & j \\ j & 1 \end{bmatrix} \begin{bmatrix} E_S(t)/\sqrt{2} \\ E_{LO}/\sqrt{2} \end{bmatrix} \qquad (3.6)$$

$$\begin{bmatrix} E_3(t) \\ E_4(t) \end{bmatrix} = \frac{1}{\sqrt{2}} \begin{bmatrix} 1 & j \\ j & 1 \end{bmatrix} \begin{bmatrix} jE_S(t)/\sqrt{2} \\ -E_{LO}/\sqrt{2} \end{bmatrix} \qquad (3.7)$$

The corresponding photocurrent at the balanced photodetector is given by,

$$\Delta i_{12}(t) = i_1(t) - i_2(t) = R_D A_S(t) A_{LO} sin(\omega_{IF} t + \Delta\varphi_S(t) \qquad (3.8)$$

$$\Delta i_{34}(t) = i_3(t) - i_4(t) = R_D A_S(t) A_{LO} cos(\omega_{IF} t + \Delta\varphi_S(t) \qquad (3.9)$$

The above Equations 3.8 and 3.9 give the quadrature and in-phase signal components respectively, from which the signal phase information is obtained. In this way, higher-level modulation formats such as QPSK, 16-QAM and above can be demodulated using the quadrature coherent detector. Figure 12 shows the setup of DP-QPSK receiver, where two quadrature coherent receivers are used to simultaneously demodulate the X and Y polarisation signals separately [13].
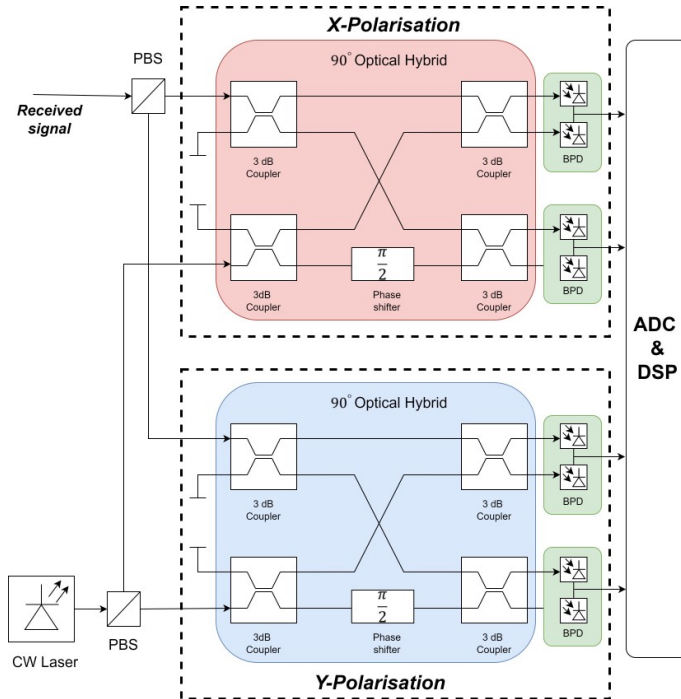
Figure 12: DP-QPSK receiver [13].

3.2 Simulation setup and parameters

The Optsim simulation tool has a suite of optical models and simulation engines to study systems ranging from long-haul optical communications to sub-micron photonic circuits at the physical level. It also includes of well-developed optical and electrical component models to study high data rate optical communication systems. Therefore, Optsim is used to simulate and analyse the performance of 100G DP-QPSK system.

Transmitter setup
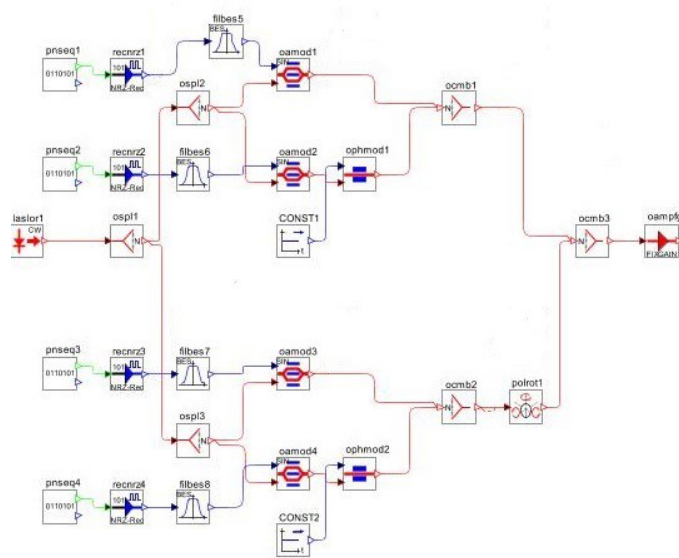
Figure 13: DP-QPSK Transmitter.

Figure 13 shows the simulation setup of the DP-QPSK transmitter. The random bit sequence at the bit rate of 100 Gbps is generated by Pseudo Random Binary Sequence (PRBS) generator and their respective non-return-to-zero (NRZ) voltage pulses drive the MZM of I and Q branches. Ideally, a CW laser is split into X and Y polarisation using PBS and given to the modulator circuit. The on-chip PBS considered in this thesis is an active component that requires an external electronic circuit to function and its DC routing makes PIC system design complex. Since polarisation components such as PBC, PBS are active, large in size, less mature and sensitive to fabrication tolerances in the PIC technology, system design with less number of polarisation components is preferred. Therefore, a CW laser(X polarisation) is split using a 1x2 power splitter and its output signals are modulated at a

data rate of 50 Gbps each. Then one of the modulated signals is rotated to Y polarisation using polarisation rotator (PR). The on-chip PR considered in this thesis is a passive component, which means that it does not require any external electronic circuit to function and is smaller in size than a PBS/PBC. Finally, both X and Y polarisation modulated signals are combined using a 2x1 combiner and transmitted over the FSO channel after the signal has been amplified using an EDFA, also known as a booster amplifier. The properties of each component are set according to the PIC foundry values, and some of the main transmitter properties are shown in Table 4.

Table 4: Transmitter simulation parameter list.

Component	Configuration Parameter	Value
Continuous Wave (CW) Laser	Wavelength	1550 nm
	Power	10 dBm
	Linewidth	0 kHz
	RIN	<-140 dB/Hz
	Azimuth	0 deg
	Ellipticity	0 deg
Power Splitter	Power ratio	3 dB
	Loss	0.5 dB
MZM	Extinction ratio	20 dB
	Insertion loss	6 dB
	V pi	4V
Phase shifter	Phase shift	90 deg
Polarisation rotator	Rotation angle	90 deg
Power combiner	Loss	0.5 dB
Booster EDFA	Gain	40 dB
	Noise Figure	6 dB

Receiver setup

The received signal is amplified by EDFA at the front end of the receiver, also known as the pre-amplifier and filtered by an optical filter at the reference center frequency with a specified bandwidth in order to select the channel and reduce the crosstalk from the neighbouring channels. The filtered optical signal is then fed to a homodyne coherent receiver to demodulate the PD-QPSK signal. The 90° optical hybrid in the coherent receivers is available as built-in component in Optsim, modelled as shown in Figure 12. The local oscillator with the 90° hybrid compound component provides the four-phase outputs. These outputs from the receiver are connected to the photodetectors, followed by transimpedance amplifier (TIA) to

amplify the photocurrents and convert them into corresponding voltages. These electrical signals are then filtered using a low pass Bessel filter and passed to a DSP unit as shown in Figure 14. The DSP unit recovers the transmitted symbols on both polarisations using Constant Modulus Algorithm (CMA) and Viterbi-Viterbi (VV) algorithms. After these steps, the resulting signal is error counted and the BER is calculated. Dispersion compensation is performed using an electronic dispersion component before the DSP unit. In this simulation, the dispersion is assumed to be close to 0 because the PIC system has a relatively short waveguide length and the link is considered to be a loss-only channel, which is discussed in the next section. To reduce the number of components and optimise the area of the PIC, the 90°
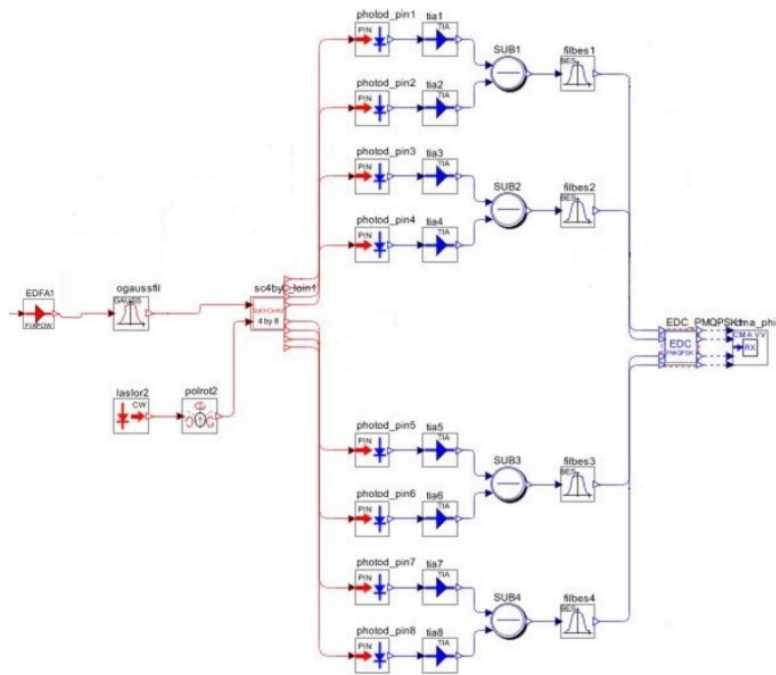
Figure 14: DP-QPSK Receiver with inbuilt 90 degree optical hybrid

optical hybrid is implemented using a 3 dB splitter and 2×2 couplers as shown in Figure 15. From here referred to as PIC based 90° optical hybrid.

The output of the PIC based 90° optical hybrid is given as,

$$\begin{bmatrix} E_1(t) \\ E_2(t) \end{bmatrix} = \frac{1}{2} \begin{bmatrix} jE_S(t) + jE_LO \\ -E_S(t) + E_LO \end{bmatrix} \tag{3.10}$$

$$\begin{bmatrix} E_3(t) \\ E_4(t) \end{bmatrix} = \frac{1}{2} \begin{bmatrix} E_S(t) + jE_LO \\ jE_S(t) + E_LO \end{bmatrix} \tag{3.11}$$
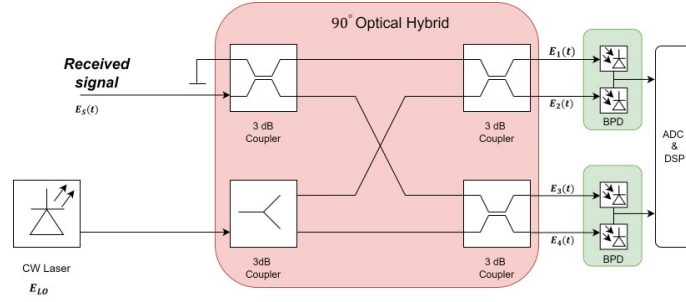
Figure 15: PIC based 90° optical hybrid model.

Table 5: Output of PIC based 90° optical hybrid.

output	Phase difference	Value
E1(t)	0	$jE_S(t) + jE_LO$
E2(t)	π	$-E_S(t) + E_LO$
E3(t)	$\frac{\pi}{2}$	$E_S(t) + jE_LO$
E4(t)	$\frac{-\pi}{2}$	$jE_S(t) + E_LO$

From Table 5, it can be concluded that the PIC based 90° optical hybrid provides the same phase differences at the output as the 90° optical hybrid discussed in section 3.1.2. Therefore, a coherent receiver with a PIC based 90° optical hybrid is considered for the simulation.

Similar to the transmitter setup, in the receiver the signals are mainly processed in X polarisation due to the polarization dependance of certain components on the photonic chip. This behaviour is represented in the Optsim simulation software by using polariser to filter the received X and Y signals followed by a polarisation rotator in the Y signal branch as shown in Figure 16. Where, the optical noise adder component at the input port of the 2×2 coupler acts as an optical null in this simulation setup. Ideally, a PBS is used to split the X and Y polarisation of the received signal as would happen on an actual PIC.
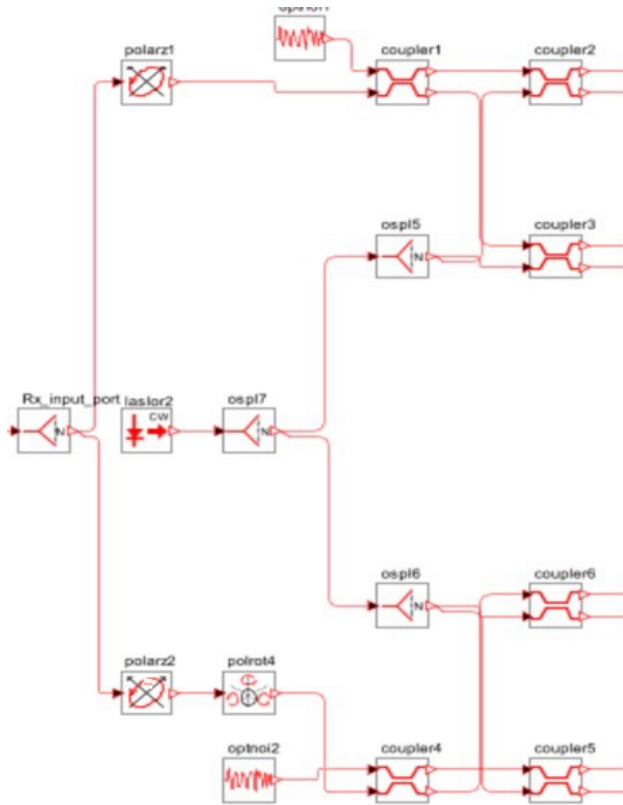
Figure 16: PIC based PD-QPSK receiver setup.

The main receiver parameters are listed in Table 6.

Table 6: Receiver Parameter.

Component	Configuration Parameter	Value
Optical filter	Type	Bandpass
	Order	2
	Bandwidth	50 GHz
Optical coupler	Output port ratio	50:50
Power Splitter	Power ratio	3 dB
	Loss	0.5 dB
Polarisation rotator	Rotation angle	90 deg
Photodetector	Responsivity	0.8 A/W
	Dark current	10 nA
Pre-amplifer EDFA	Gain	30 dB
	Output power	0 dBm
	Noise Figure	4 dB

Channel link

The static link budget of ground-to-space link for GEO satellites is referred from *'Optical technologies for very high throughput satellite communications by Mata Calvo'* [1]. The main parameters considered for the optical feeder link and the GEO link budget are shown in Table 7.

Table 7: Channel link Parameter.

Parameters	GEO
Spacecraft altitude	36000 Km
Elevation	30 degree
Transmitted divergence(e^-2)	6 µrad
Beam wander or pointing jitter	1.7 µrad
satellite receiver antenna	30 cm
Ground antenna Gain	113.4 dB
Free-space loss	-290 dB
Mean pointing-loss	-2.8 dB
Scintillation margin for 99.99% availability	-3.7 dB
Atmospheric attenuation + Cloud margin	-2.0 dB
satellite receiver antenna Gain	115.7 dB
Transmitter and receiver efficiency	-4 dB
atmospheric attenuation + Cloud margin (ancillary losses)	-2 dB
Total link loss	**-75.3 dB**

From the Table 7, it can be said that the optical communication system for GEO satellites should be designed with a minimum link loss allowance of ≈75.3 dB. Since the table includes the main link impairments and the optical feeder link parameters, the consideration of the channel loss alone is the starting point to design the system and evaluate its performance under different system noise conditions. Therefore, various simulations are performed to analyse the 100G DP-QPSK system performance under different system impairments.

3.3 Results and discussion

The simulations are carried out with the previously mentioned system parameters in Tables 4, 6 and 7 for both DP-QPSK receiver with built-in 90° optical hybrid and DP-QPSK receiver with PIC based 90° optical hybrid model as shown in Figures 17 and 18. The attenuator is included in the channel link with a sweep range of 77 - 85 dB to cover the GEO link loss budget. According to the Institute of Electrical

and Electronics Engineers (IEEE) standard, the minimum BER requirement for a 100G optical communication system without FEC encoding is ≤4.5E-3 in order to achieve a post-FEC BER of ≤10E-15 [25]. Therefore, the simulations are performed with 100000 simulation bits for the bit rate of 100 Gbps to calculate BER rate in the range of up to 1E-6 at the center frequency of 1550 nm.
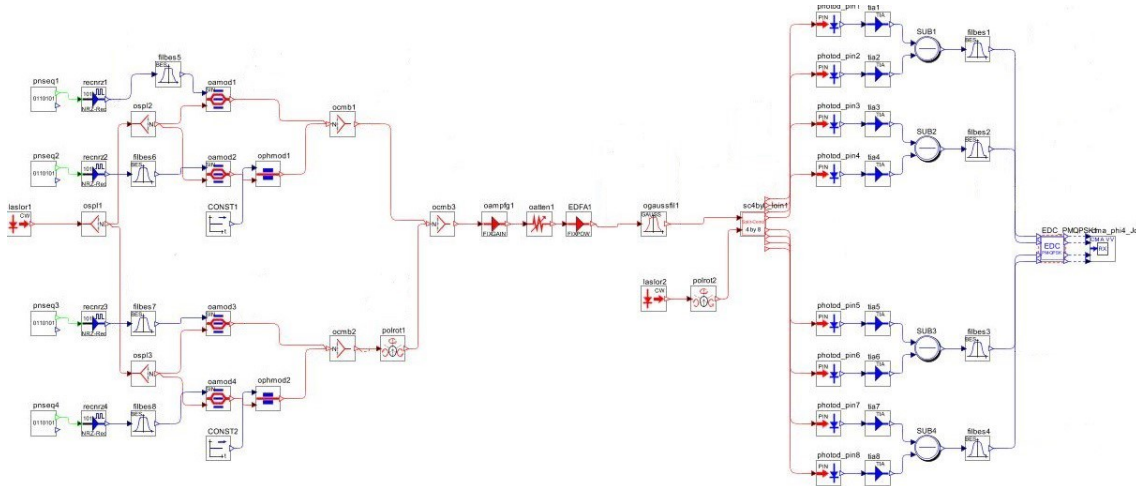
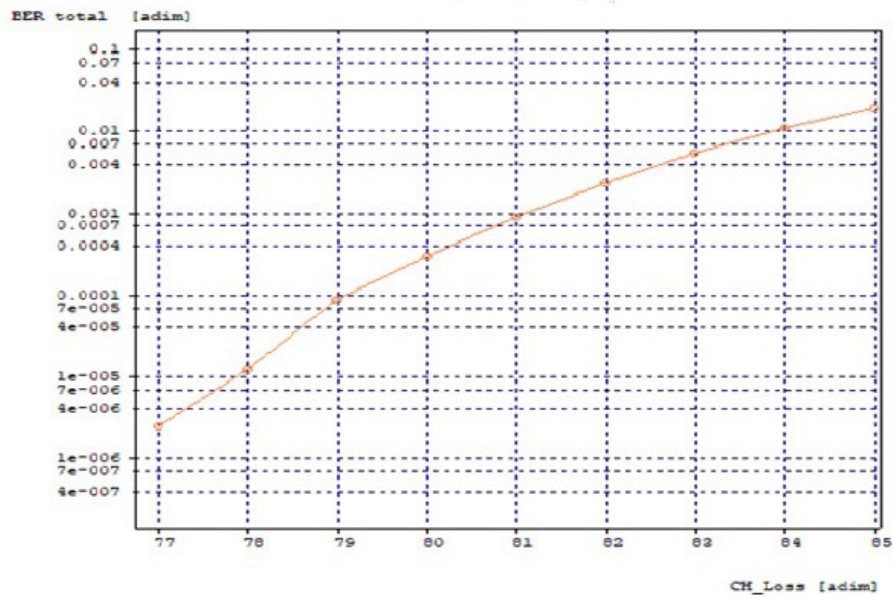**Figure 17:** System with Inbuilt receiver setup.
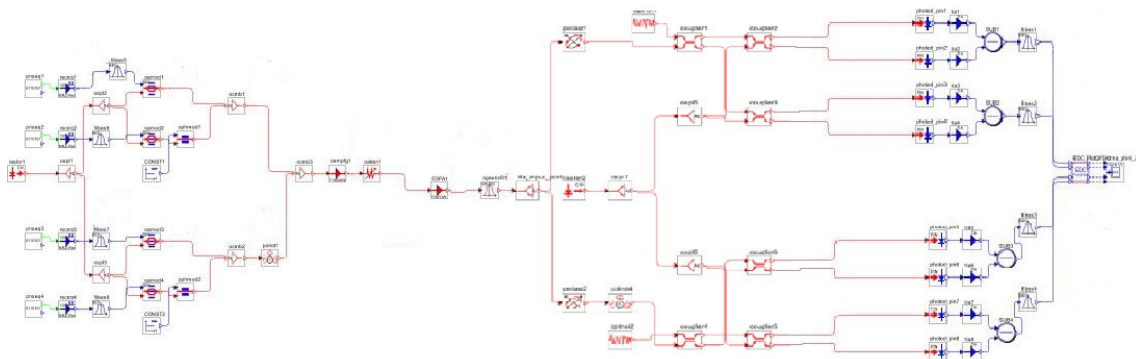
Figure 18: System with PIC based DP-QPSK receiver setup.

The channel loss vs BER for both the systems is shown in Figure 19. It is observed that as the channel loss increases, the BER also increases, which means that the system becomes more susceptible to noise at higher system losses, which eventually reduces the quality of the received signal so that the receiver can't retrieve the symbols.

At BER 1E-3, both systems can accommodate the channel loss of 81 dB, which is more than the GEO link budget requirement of 75.3 dB. The optical signal to noise ratio (OSNR) of the received signal at the optical filter is shown in Figure 20. It is

(a) System with Inbuilt receiver model.
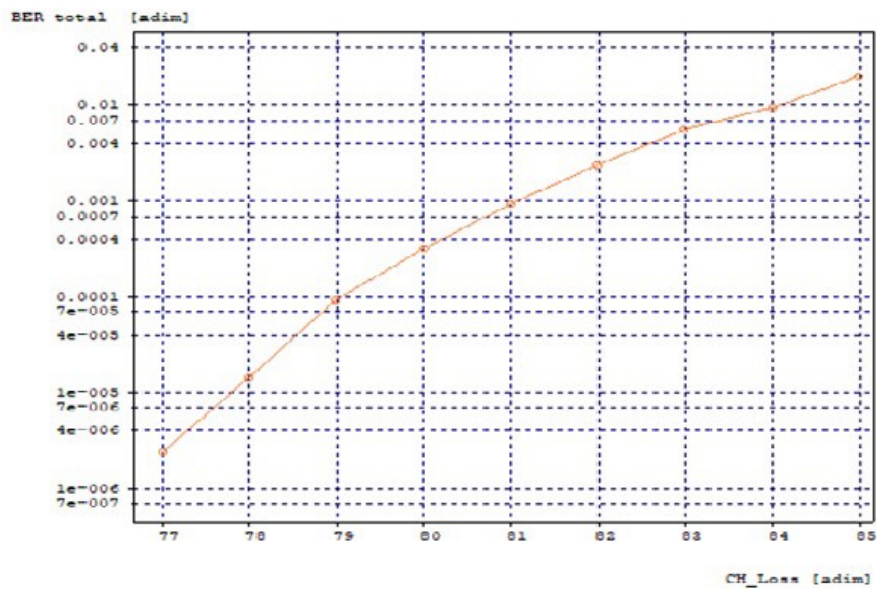
(b) System with PIC based receiver model.

Figure 19: Performance analysis of DP-QPSK system: Channel loss Vs BER.

observed that as the channel loss (sweep run) increases, the OSNR decreases. This means that the signal power is less than the noise power at higher link losses of >81 dB and even with the local oscillator the receiver cannot able to recover the symbols.

Therefore, the receiver with PIC based 90° optical hybrid will be considered for further detailed performance analysis with different system noise.

(a) Received signal spectrum.

(b) OSNR (dB) Vs Channel loss in dB (sweep run).
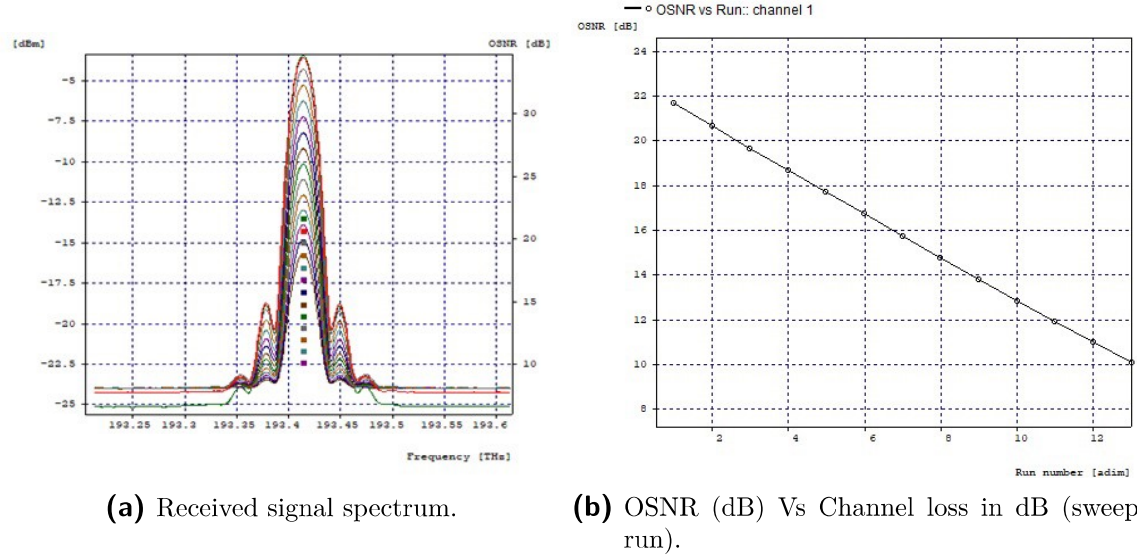
Figure 20: Performance analysis of DP-QPSK system: OSNR.

3.3.1 Performance under different noise conditions

The system is simulated under different conditions such as no noise, shot noise only and EDFA ASE noise only to determine the dominant noise source in the system. Figure 21, Figure 22 and Figure 23 shows the BER performance and constellation diagram of the received symbols before DSP for the above said conditions.

(a) Link loss (dB) Vs BER.

(b) Constellation diagram.
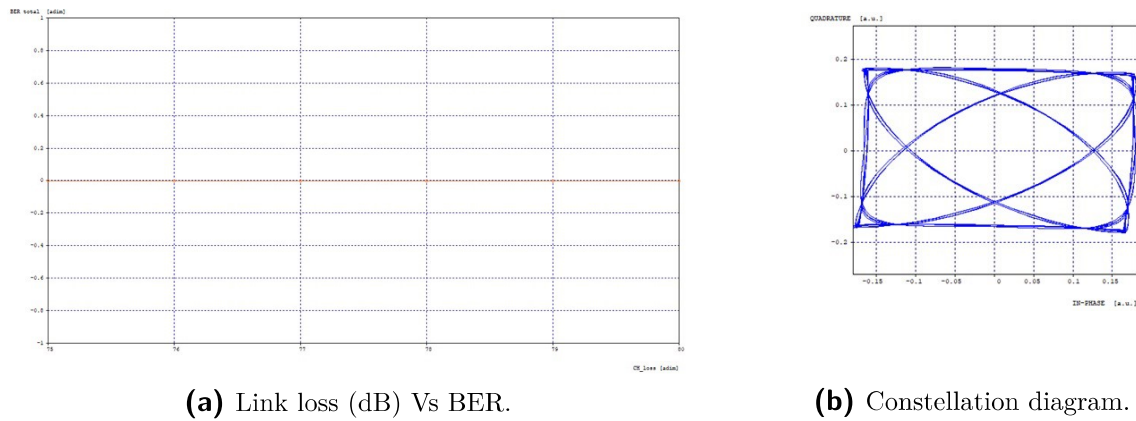
Figure 21: Performance analysis: No noise system.

From Figure 21, it is clear that the no noise system has 0 error bits along the channel loss sweep of 75 - 80 dB (Figure 21a). Its constellation diagram, visualised at the receiver shown in Figure 21b, clearly shows the four different symbols and their transition path. This means that the receiver can precisely demodulate the signal and make the correct decision at the appropriate threshold voltage of bits '0' and '1'.

47

(a) Link loss (dB) Vs BER.

(b) Constellation diagram.
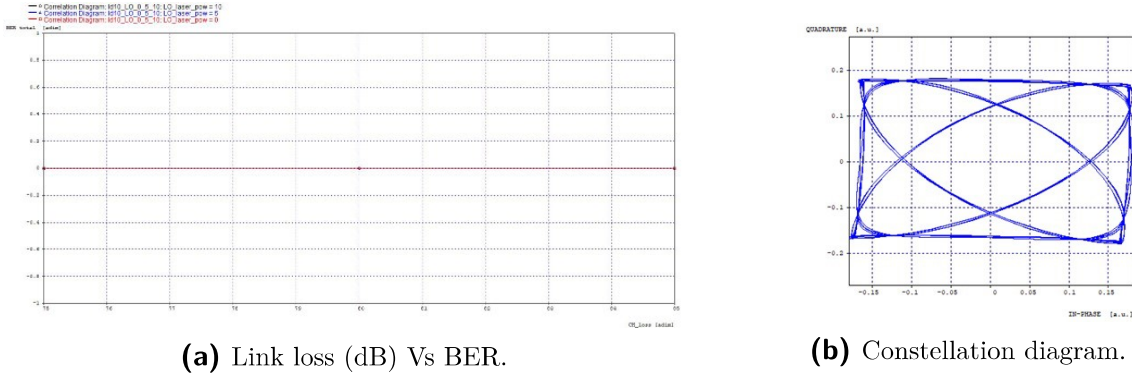
Figure 22: Performance analysis: Shot noise system.

(a) Link loss (dB) Vs BER.

(b) Constellation diagram.
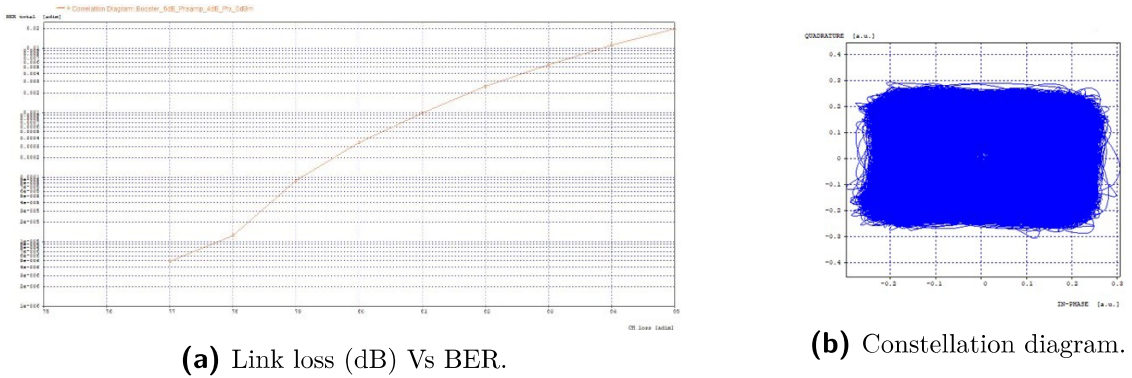
Figure 23: Performance analysis: ASE noise system.

The BER performance of the system under the shot noise only condition is shown in Figure 22. Where different ranges of shot noise at the receiver are simulated by varying the local oscillator power. Figure 22a shows the channel loss vs BER relationship for the local oscillator power sweep of 0, 5 and 10 dBm with 10 nA dark current. It can be seen that the system with shot noise only system has 0 bit error rate along the channel loss sweep from 75 to 85 dB. Its constellation diagram (22b) at the receiver also implies that shot noise does not affect the received signal by clearly visualising the symbols and their transition path.

While the system performance with EDFA ASE noise only condition shown in Figure 23, implies that ASE noise affects the system performance in the GEO link loss region. In Figure 23a, it is observed that as the channel loss increases, the BER also increases. Also, the received signal quality degrades at higher link losses which can be seen in the constellation diagram shown in Figure 23b. Where, the transition paths between the symbols become closer and symbols cannot be distinguished. Therefore, it can be concluded that the ASE noise source is dominant in the system and its impact on the BER performance should be analysed in detail to evaluate the overall system performance for GEO satellite link.

3.4 Analysis of system performance with ASE noise

In this section, the system performance with ASE noise due to EDFA is studied in detail along with other noise sources in the system. All the simulated results are exported and plotted using MATLAB for better readability.

The analysis of system performance with ASE noise is divided as follows:

- ASE noise impact with different RIN noise of laser

- ASE noise impact with different MZM extiniction ratio

- ASE noise impact with different dark current

- ASE noise impact with different shot noise

3.4.1 ASE noise impact with different RIN noise of laser

In order to analyse the impact of ASE noise with RIN in the system performance, simulations are carried out with different NF of the booster and pre-amplifier together with realistic RIN values in the transmitter laser and LO. The effects of ASE noise with RIN under realistic received signal power are also considered. The simulation scenarios are given in the Table 8. The scenario with amplifiers NF of 0 dB is only considered for simulation purposes to analyse the system under 'no ASE noise' condition.

Table 8: ASE noise analysis wtih RIN simulation scenarios.

Scenario	NF of Booster and Pre-Amplifier (dB)	Received power(dBm)	RIN (dB/Hz)
1	0	0,-20	-120,-140
2	6	0,-20	-120,-140

From the Figure 24, it is observed that as the RIN increases from -140 dB/Hz to -120 dB/Hz along with the receiver power in the range of -20 dBm to 0 dBm, the channel loss that the system can accommodate at a BER of 1E-3 decreases in the range from $\approx$85.1 dB to $\approx$84.8 dB. Scenario 2 also shows the same trend of link loss vs BER in Figure 25, but the channel loss allowance is in the range of $\approx$79.2 dB to $\approx$78.8 dB at 10^{-3} BER. Therefore, the system configuration of minimum RIN, maximum received power and almost no ASE noise is simulated to have a reference of the system performance under no ASE noise condition and later compared with the system with poor configuration of maximum RIN, minimum received power and maximum EDFA NF is simulated. Their BER performances are shown in the
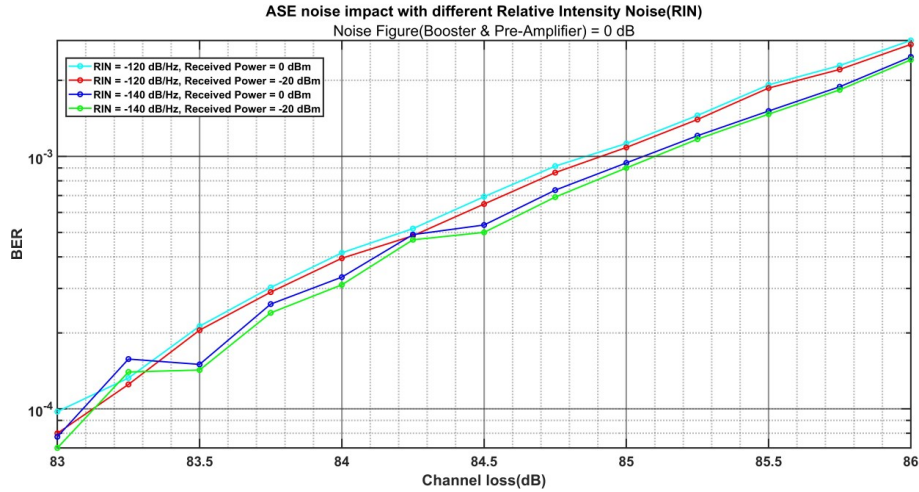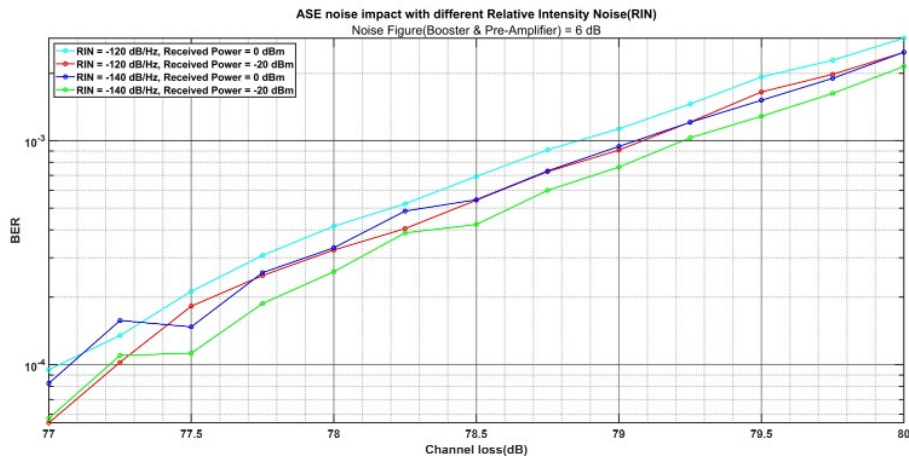
Figure 24: Scenario 1.

Figure 25: Scenario 2.

Figure 26. It is observed that the link loss allowance penalty between the system with almost no ASE noise condition (red) and high noise condition (blue) is ≈6 dB. However, in both the conditions the system is able to meet the GEO link loss budget.

3.4.2 ASE noise impact with different MZM extinction ratios

The extinction ratio of the MZM can degrade the quality of the signal to be demodulated at the receiver, so the effect of ASE noise with different MZM extinction ratios on system performance is analysed. The simulation scenarios are shown in the Table 9.

In Scenario 1, as the MZM extinction ratio increases, the link loss allowance also increases at BER of 1E-3. The link loss that the system can accommodate lies in
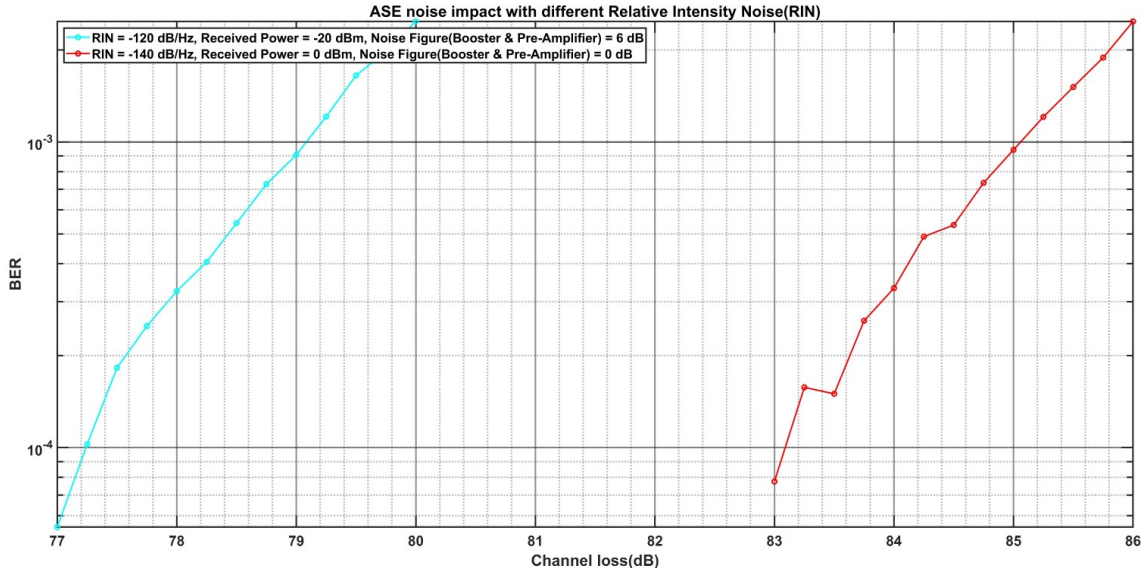
Figure 26: RIN with best and worst condition.

Table 9: ASE noise analysis with MZM extinction ratio scenarios.

Scenario	NF of Booster and Pre-Amplifier (dB)	Received power(dBm)	MZM ER (dB)
1	0	0,-20	5, 10, 15, 20
2	6	0,-20	5, 10, 15, 20
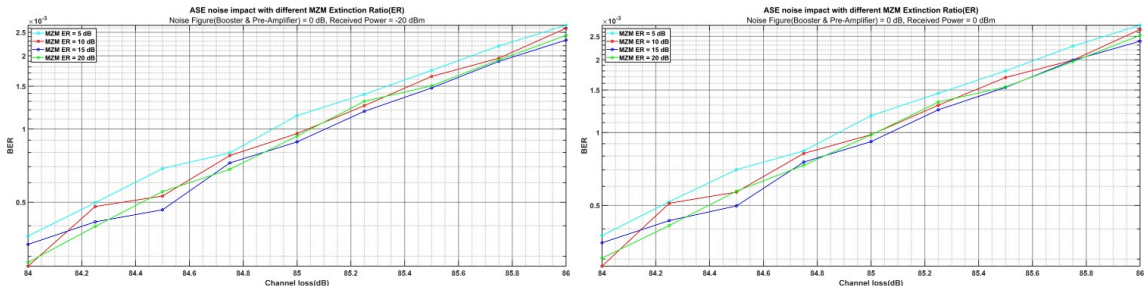
Figure 27: Scenario 1.
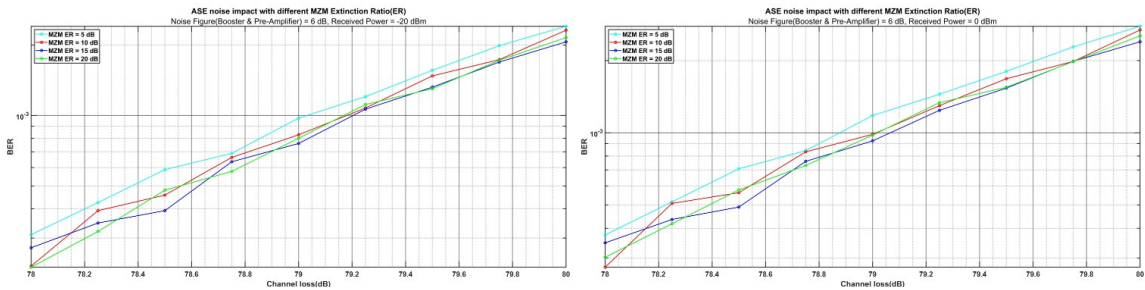
Figure 28: Scenario 2.

the range of ≈84.8 dB and ≈85.1 dB. Same trend is observed between the channel loss vs BER in scenario, but the link loss allowance is in the range of ≈78.9 dB and

$\approx$79.1 dB due to more noise in the EFDA.

Therefore, the system with maximum MZM extinction ratio with lower noise parameters and the system with minimum MZM extinction ratio with high noise condition are simulated. From this, the link loss allowance penalty between the system with the almost no ASE noise configuration and the high noise configuration influenced by MZM extinction ratio is analysed.
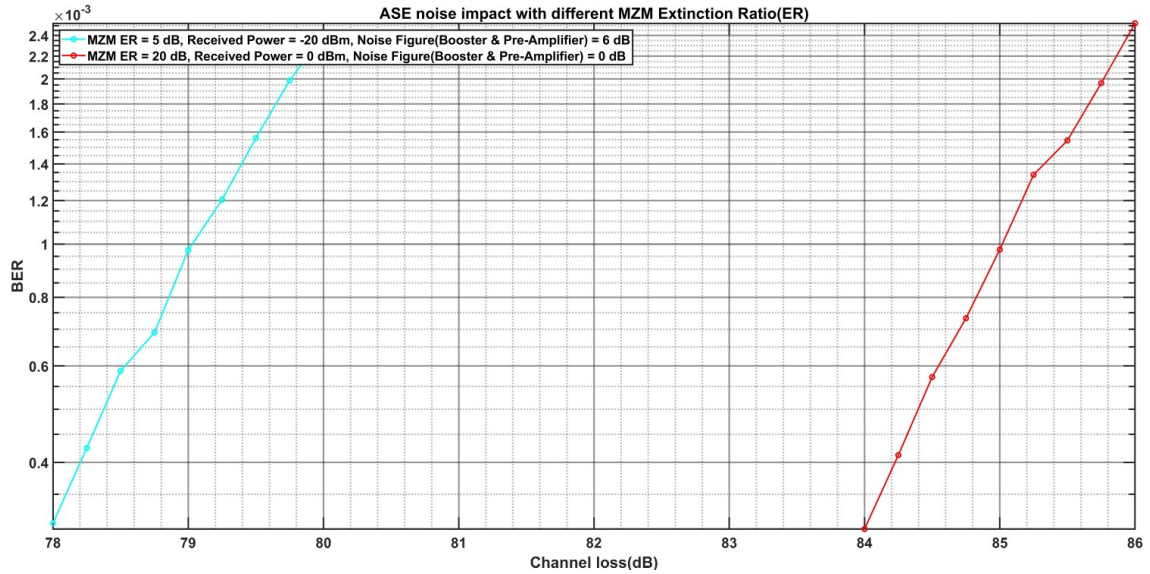
Figure 29: MZM extiction ratio with best and worst condition.

From 29, it is observed that the link loss allowance penalty between the system with almost no ASE noise condition (red) and high noise condition (blue) is $\approx$6 dB. It is in the range of $\approx$79 dB and $\approx$84 dB, which is above the required GEO link loss budget of 75.3 dB.

3.4.3 ASE noise impact with different dark current

This section discussed the impact of ASE noise together with photodetector dark current on the system performance, as the dark current generated by the photodetector can degrade the received signal quality and increase the BER. The simulation scenarios are shown in the Table 10.

From the Figure 30, it can be seen that as the dark current in the photodetector increases, the channel loss allowance decreases correspondingly at a BER of 1E-3. The penalty between the dark currents is $\approx$0.1 dB in the channel loss range of $\approx$84.7 dB and $\approx$85 dB for the received power of 0 and -20 dBm respectively. In Scenario

Table 10: ASE noise analysis with photodetector dark current scenarios.

Scenario	NF of Booster and Pre-Amplifier (dB)	Received power(dBm)	Dark current (nA)
1	0	0,-20	0, 5, 10
2	6	0,-20	0, 5, 10
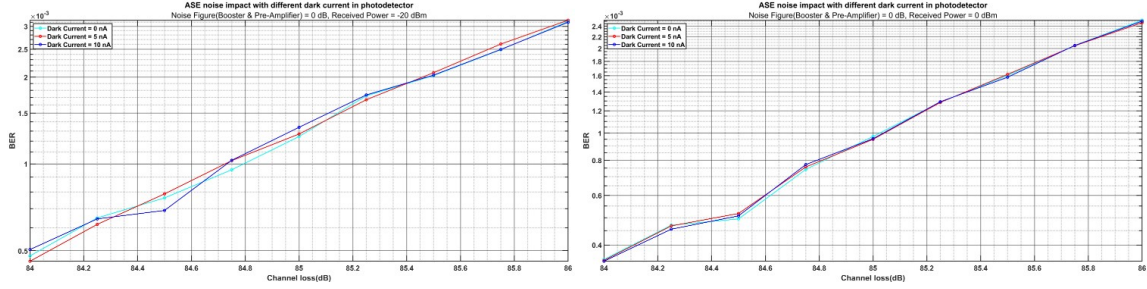
Figure 30: Scenario 1.
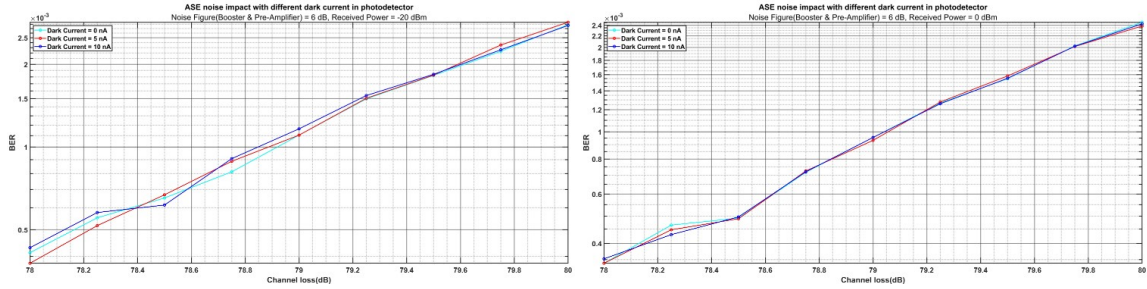
Figure 31: Scenario 2.

2, the penalty between the dark currents is also ≈0.1 dB, but in the channel loss range of ≈79.1 dB and ≈78.9 dB for received power 0 and -20 dB respectively.

Therefore, the systems with almost no ASE noise configuration and high ASE noise configuration with dark current are simulated to evaluate the link loss allowance penalty between them.

From Figure 32, it is observed that the link loss allowance penalty between the system with almost no ASE noise condition (red) and high noise condition (blue) is ≈6.2 dB in the channel loss accommodation range of ≈78.8 dB and ≈85 dB. Nevertheless, the system is able to meet the GEO link loss budget in both conditions.

3.4.4 ASE noise impact with different shot noise

The main noise source at the receiver is the shot noise, which is mainly influenced by the LO power and the dark current. Therefore, the effect of ASE noise together
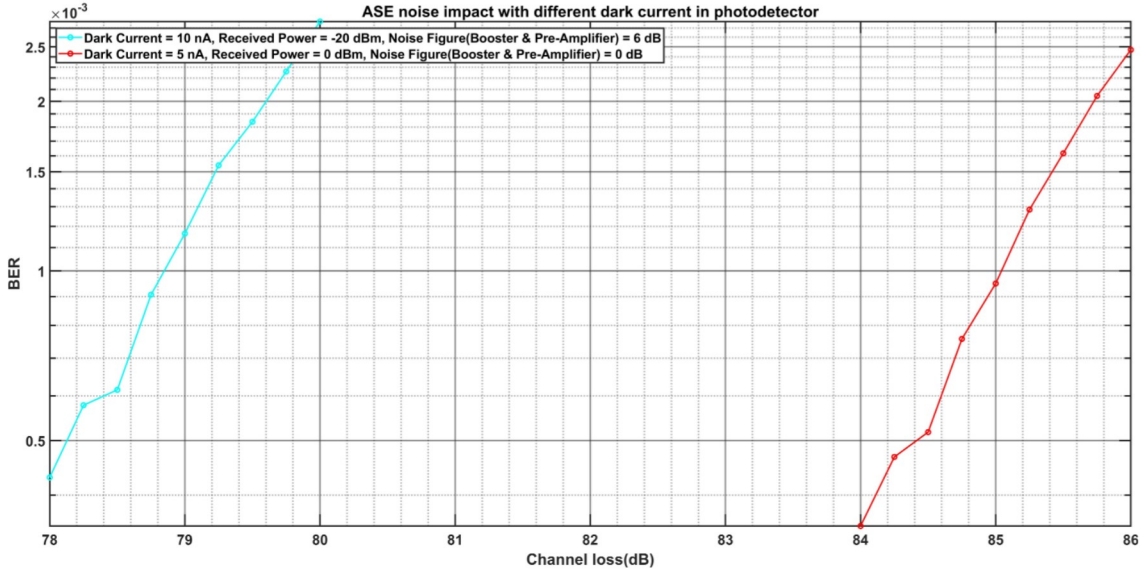
Figure 32: Photodetector dark current with best and worst condition.

with shot noise on system performance is studied under different scenarios. The simulation scenarios are shown in the Table 11.

Table 11: ASE noise analysis with shot noise scenarios.

Scenario	NF of Booster and Pre-Amplifier (dB)	Received power(dBm)	LO power (dBm)
1	0	0,-20	0, 5, 10
2	6	0,-20	0, 5, 10
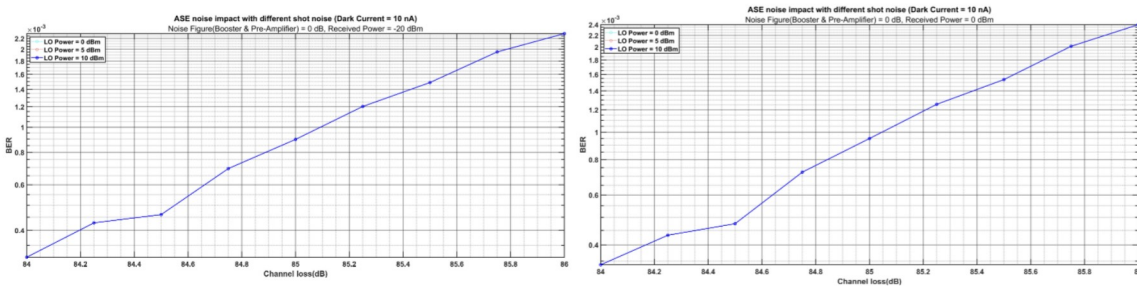
Figure 33: Scenario 1.

From the Figure 33, it is observed that the system with -20 dBm received power has a link loss allowance of ≈85.1 dB irrespective of the LO power. On the other hand, the system with 0 dBm received power has the link loss allowance of ≈85.05 dB irrespective of the LO power. So that the link loss allowance penalty between them is negligible regardless of the LO power. From this, it can be concluded that in scenario 1, shot noise has a no impact on system performance as the received
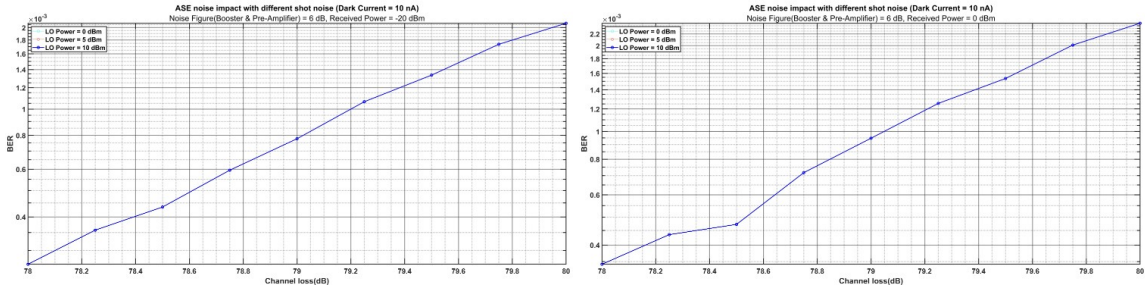
Figure 34: Scenario 2.

signal power increases.

In the scenario 2 system performance shown in Figure 34, the link loss allowance is ≈79.2 dB for the system with -20 dBm received power and ≈79.05 dB for the system with 0 dBm received power. The penalty for the link loss allowance between them is 0.15 dB regardless of the LO power. This means that in a system with high ASE noise, the effect of shot noise on system performance increases rapidly as the received signal power increases. Therefore, the system is simulated with the almost no ASE noise configuration and the maximum ASE noise configuration together with the shot noise to evaluate the link loss allowance penalty between them. From Figure
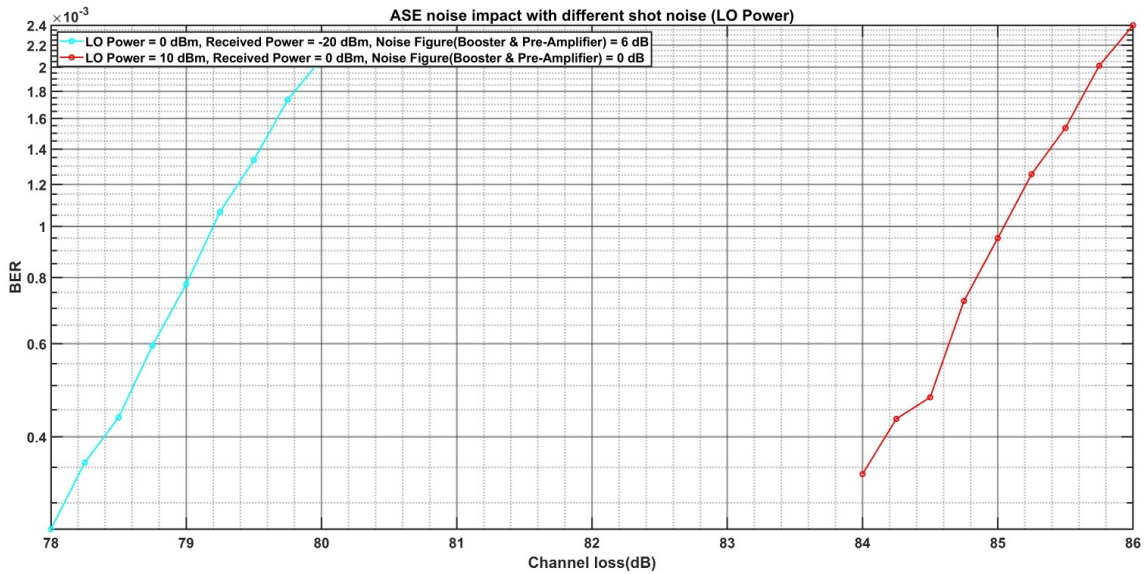
Figure 35: ASE with Shot noise under best and worst condition.

32, it is observed that the link loss accommodation penalty between the system with low noise condition (best system configuration) and high noise condition (poor system configuration) is ≈5.8 dB in the channel loss range of ≈78.2 dB and ≈85 dB, which is above the required GEO link loss budget.

3.5 Overall system performance

From the previous section, it is clear that the ASE noise together with different system noise scenarios does not limit the system performance for GEO satellite link. Therefore, systems with different overall conditions are simulated in order to scale the corresponding system performance in terms of link loss allowance. The various scenarios are given in the Table 12.

Table 12: Different overall system conditions.

Scenario	Booster NF(dB), Gain(dB)	Pre-Amp NF(dB), Power(dBm)	RIN(dB/Hz)	MZM ER(dB)	Dark current(nA)
1	6, 40	6, 0	-120	5	10
2	3, 40	3, 0	-140	20	10
3	0, 40	0, 0	-140	20	0
4	6, 40	4, 0	-140	20	10
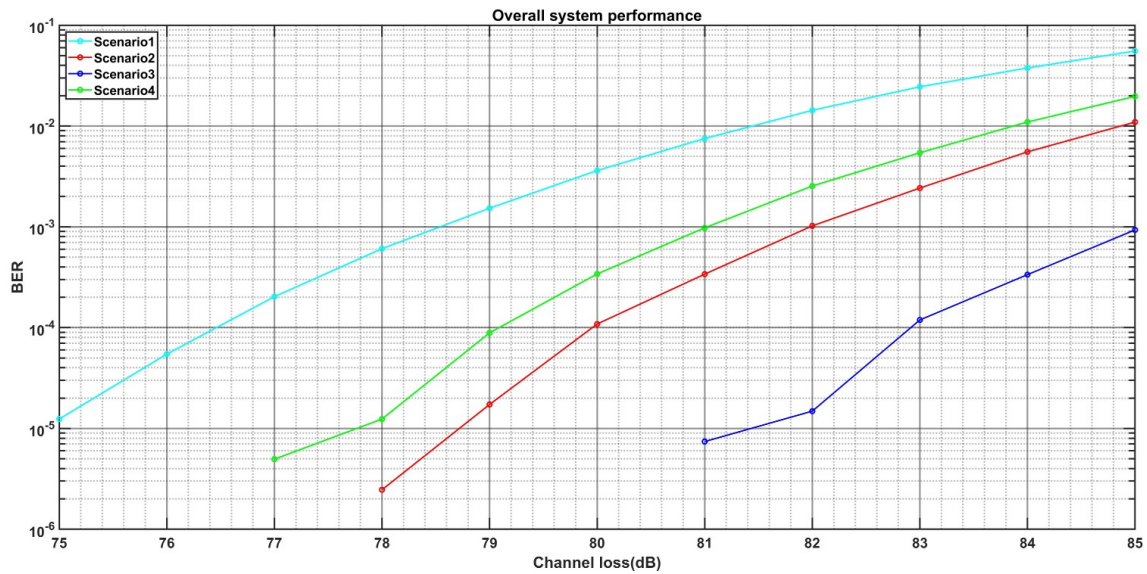
Figure 36: Overall system conditions.

In Figure 36, it is observed that the system in scenario 1 with high noise condition is able to tolerate the link loss of ≈78.5 dB at 1E-3 BER. The physical limit of EDFA is 3 dB, so the system performance with 3 dB NF is plotted as Scenario 2 and it shows the link loss tolerance of ≈82 dB at 1E-3 BER. The system in scenario 3 with almost no noise condition can tolerate the link loss of ≈85 dB at 1E-3. The system performance according to the foundry specification is shown in scenario 4, which has a link loss tolerance of ≈81 dB at 1E-3 BER.

From the noise analysis of various system conditions, it can be observed that the NF of EDFA mainly affects the system performance in the channel loss range of ≈78.5 dB and ≈85 dB at a BER of 1E-3. The booster amplifiers placed at the transmitter side provides compensation to the losses in the transmitter components and maximize the output power so that signal can travel longer distance. Therefore, booster amplifier is selected with high saturation power with moderate gain and NF.

Whereas, pre-amplifer is placed in front of the receiver to amplify the weak received signal to the level where the receiver can detect the signal above the thermal noise threshold and provides an improvement in receiver sensitivity. In this case, sensitivity depends upon the pre-amplifier NF, gain and optical bandwidth. Hence, the pre-amplifier is selected with low NF and gain corresponds to receiver sensitivity. So, NF of pre-amplifier becomes more important since it can potentially increase and decrease the system performance. Therefore, the system is simulated for different pre-amplifier NF with a given booster amplifier configuration at a link loss of 81 dB and its BER performance is shown in Figure 37.
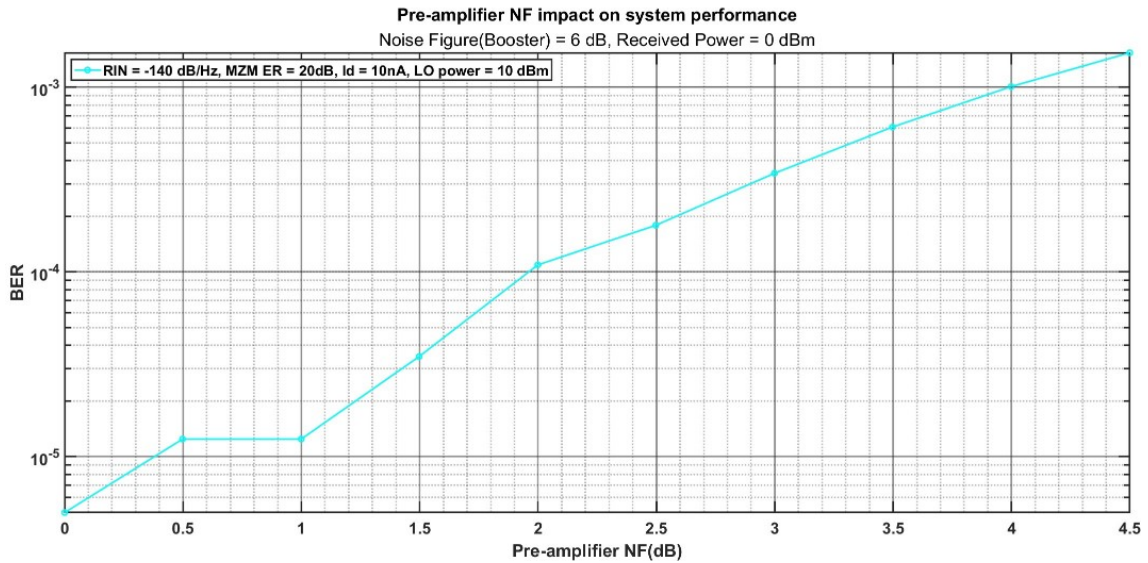
Figure 37: System performance under different NF of pre-amplifier.

It is observed that the system configured with given foundry parameters, as NF of pre-amplifier increases, BER also increases for the link loss of 81 dB. It can be seen from the above figure at 4 dB NF in EDFA the system has a link loss allowance of 81 dB at BER of 1E-3. Therefore, it can be concluded that the simulated 100 Gbps DP-QPSK system meets the GEO satellite link loss budget of 75.3 dB.

3.6 DP-QPSK system PIC layout

The PIC layout for the simulated DP-QPSK system is done using the Nazca design tool. The Nazca design tool is an open source Python based tool to provide a high quality PIC design. Nazca uses an open source Klayout editor/viewer to visualise the PIC layout. Using Nazca design tool, hierarchical PIC design can be done using script syntax and visualised in mask layout.

The dimensional parameters of the optical components are provided by the PIC foundry. The PIC should be designed according to the foundry's design guidelines. Important design parameters and guidelines are given in the Table 13.

Table 13: PIC layout guidelines.

Criteria	Comments
RF	500 μm GSG contact pitch and 100 μm spacing from chip edges - Minimum RF routing bending radius is 600 μm
DC	- DC pads pitch 250 μm 100 μm spacing from top and bottom of PIC - Minimum DC metal routing width 16 μm - Minimum routing gap between two metal is 24 μm boundary
Optical	0.5 mm of exclusion tone from fiber array - Waveguide width 2 μm - Minimum routing gap between waveguide is 2 μm boundary - Minimum bending radius is 250 μm
Routing	- DC - Optical crossing at 90° or 45° - RF - Optical crossing at 90°

3.6.1 Layout

According to the guidelines and component dimension the PIC layout for 100 Gbps PD-QPSK system is done in $8 \times 12mm^2$ chip and shown in Figure 38.
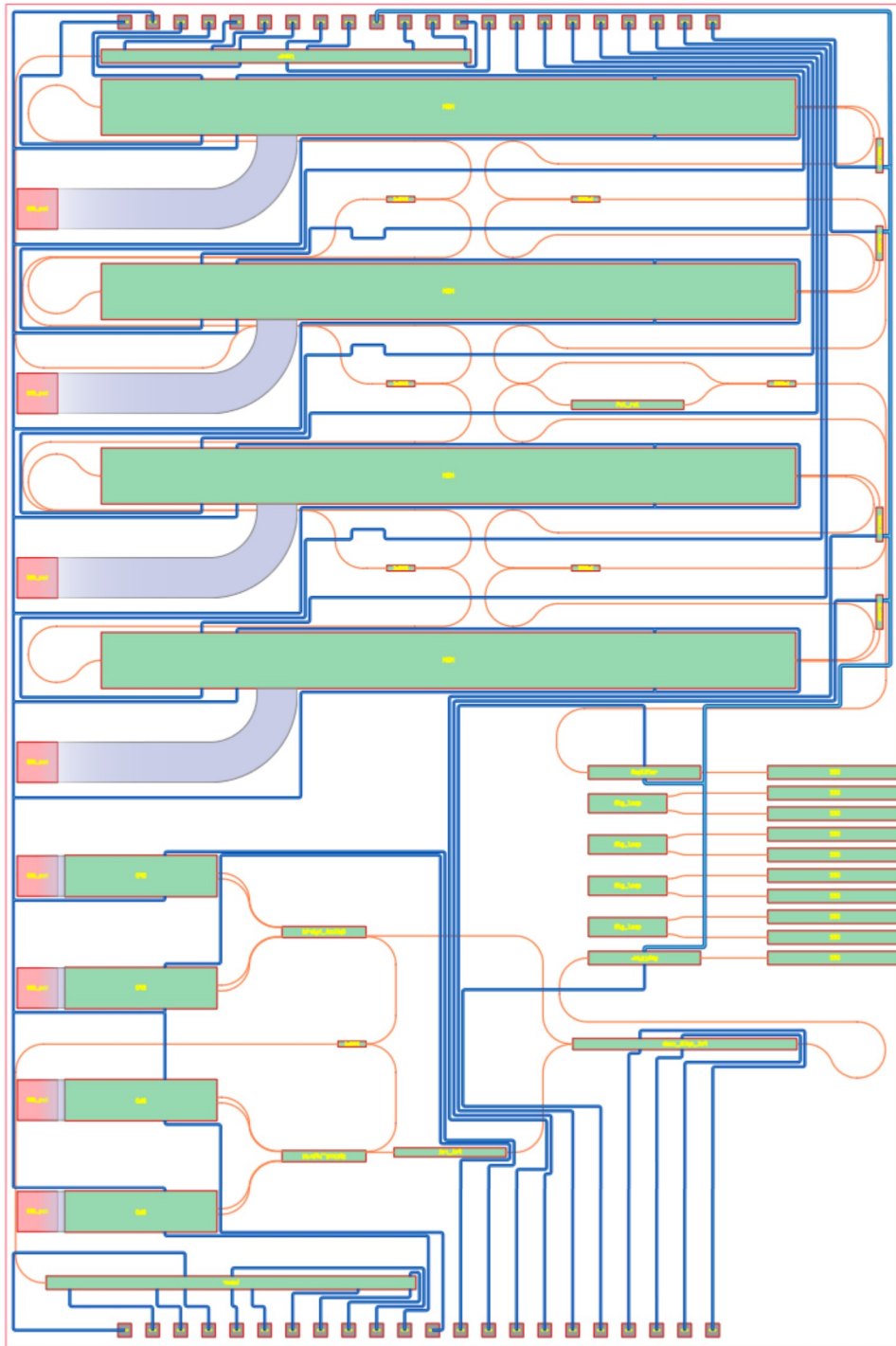
Figure 38: PD-QPSK PIC layout.

This layout shows the DP-QPSK system on InP material. The rectangular place-holders are used to design the system instead of the actual design of the individual components. The placeholder dimensions of the optical devices, the electrical contact pads and their input/output (I/O) ports are designed according to the foundry specifications. The DC contact pads(gray) are placed in the area closer to the top and bottom edges of the chip, and the area closer to the left part of the chip is reserved for the RF GSG contact pads(red).

The optical devices are coded in green colour. They are strategically placed to provide modulation and demodulation functionality. This means that a CW transmitter laser placed near the top DC pad array is split and connected to the input ports of four MZMs so that the light enters through them and modulated at the same time, in other words the CW laser is split and connected to the four MZMs using equal length waveguides. Similarly, the signal from the output ports of the MZMs is combined using equal length waveguides to achieve DP-QPSK modulation.

Likewise, the receiver components are strategically placed so that the X and Y polarisation signals reach their respective 90° optical hybrids simultaneously, and then the demodulated signals from the 90° optical hybrids reach their respective BPDs simultaneously. The optical and metal routing is also strategically planned so that it does not overlap with the devices and follows the given foundry guidelines. The RF routing is also planned in such way that, at the transmitter, the MZM drive voltage signals reach their respective MZMs simultaneously and modulate the optical signal at a rate of 25 Gbps each. Similarly, the IQ components of the X and Y polarisation demodulated signals are connected to corresponding GSG contact pads using the same length of RF routing, so that the signals are delivered to the post-processing unit for information recovery without any latency.

The RF, DC metal and waveguide are colour coded as purple, blue and orange respectively. The area closer to the right edge of the chip is reserved for an optical fiber array with spot-size converter through which the signal is transmitted and received. In addition, four alignment loops are placed closer to the fiber array, which are used for active alignment routines to achieve the best coupling efficiency at the optical interface. A monitor photodetector for the transmitter laser, LO and four MZMs are also added close to the respective devices for system monitoring and debugging.

The upper part of the chip is designed with a transmitter. Where, four MZMs placeholders occupy a large area in the chip. The first IQ modulator modulates the 25G baud of data and transmits the signal in X polarisation, while the bottom IQ modulator modulates the 25G baud data and transmits in Y polarisation using a polarisation rotator component. The quadrature phase modulation is achieved by connecting the 90° phase difference output ports of the 2nd and 4th MZMs to the 0° phase difference output ports of the 1nd and 3rd MZMs respectively. The signals are the combined by the 2×2 combiner, followed by the booster amplifier. Finally, the signal is transmitted out of the PIC through a spot size converter.

The receiver is designed in the lower part of the chip, where the received signal is split into two orthogonal polarisations using a polarisation beam splitter. The two signals are then separately demodulated using two 90° optical hybrids in the X polarisation, which is achieved by adding a polarisation rotator in the Y polarisation branch and their respective photocurrents from the balance detectors are fed to the post-processing unit via GSG pads.

4 100G DP-DQPSK System

4.1 Theoretical overview on DP-DQPSK Modulation

Similarly to the DP-QPSK scheme, the DP-DQPSK scheme encodes message bits into four different phases of the carrier signal on two orthogonal polarisations. Each symbol carries two bits, so both the X and Y polarisation states are modulated at a rate of 50 Gbps each. However, the phase modulation done in the DQPSK system is differential with respect to the previously transmitted symbol. This is achieved by using a precoder that provides differential output symbols corresponding to the current message bits and the previously transmitted symbol [10].

At the receiver, detection of the phase changes provides the information about the message bits which can be achieved by delaying the signal by one symbol period using delay line interferometer (DLI). Therefore, coherent receiver setup is not needed to demodulate the signal by using local oscillator [10]. Demodulation of the received signal can be achieved by direct detection receiver with a delay line interferometer.

4.1.1 DP-DQPSK Transmitter

The transmitter setup is similar to the DP-QPSK transmitter setup, but with an additional precoder component that drives the MZM [10]. The transmitted signal with differential phase is given as,

$$x(t) = A\cos(2\pi f_c t + \theta_d(k)), kT \le t \le (k+T) \tag{4.1}$$

Where, $\theta_d(k)$ is the differential phase. The phase difference between the phase of the currently transmitted symbol $\theta_d(k)$ and the phase of the previously transmitted

symbol $\theta_d(k-1)$ according to the message bits is given by [10],

$$
\theta_d(k) - \theta_d(k-1) = \begin{cases} \pi & if(m_I(K), m_Q(K)) = (0,0) \\ \frac{3\pi}{2} & if(m_I(K), m_Q(K)) = (1,0) \\ 0 & if(m_I(K), m_Q(K)) = (1,1) \\ \frac{\pi}{2} & if(m_I(K), m_Q(K)) = (0,1) \end{cases} \tag{4.2}
$$

Where, m_I and m_Q are the message bits modulated to the in-phase and quadrature phases of the carrier signal.

Precoder

The DQPSK coding condition given in the Equation 4.2 is achieved using the precoder subsystem shown in Figure 39. The precoder processes the previously transmitted symbol $x_d(K-1)$ using one symbol period delay unit τ and current message bits $x(k)$ to produce the differential output x_d according to the above said coding conditions [10].
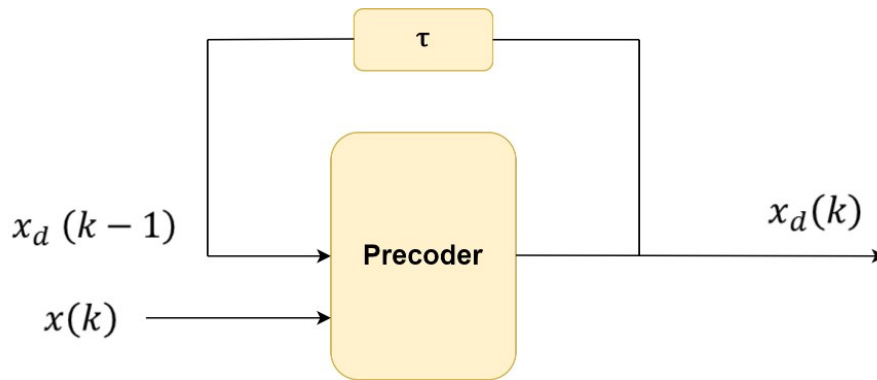
Figure 39: DQPSK precoder [10].

The precoder output chart is shown in Table 14. Where, $m_I(k)$ and $m_Q(k)$ are the message bits with the corresponding QPSK phase mapping of $\theta(k)$. $I_d(k-1)$ and $Q_d(k-1)$ are the previously transmitted bits with the corresponding QPSK phase mapping of $\theta_d(k-1)$. $I_d(k)$ and $Q_d(k)$ are the current differential output bits with the corresponding phase of $\theta(k)$. $\theta_d(k) - \theta_d(k-1)$ is the differential phase condition between the previous transmitted symbol and the current symbol [10].

Table 14: Precoder output chart [10].

$m_I(k)$	$m_Q(k)$	$\theta(k)$	$I_d(k-1)$	$Q_d(k-1)$	$\theta_d(k-1)$	$I_d(k)$	$Q_d(k)$	$\theta_d(k)$	$\theta_d(k) - \theta_d(k-1)$
0	0	$\pi/4$	0	0	$\pi/4$	1	1	$5\pi/4$	π
0	0	$\pi/4$	0	1	$7\pi/4$	1	0	$3\pi/4$	π
0	0	$\pi/4$	1	0	$3\pi/4$	0	1	$7\pi/4$	π
0	0	$\pi/4$	1	1	$5\pi/4$	0	0	$\pi/4$	π
0	1	$7\pi/4$	0	0	$\pi/4$	1	0	$3\pi/4$	$\pi/2$
0	1	$7\pi/4$	0	1	$7\pi/4$	0	0	$\pi/4$	$\pi/2$
0	1	$7\pi/4$	1	0	$3\pi/4$	1	1	$5\pi/4$	$\pi/2$
0	1	$7\pi/4$	1	1	$5\pi/4$	0	1	$7\pi/4$	$\pi/2$
1	0	$3\pi/4$	0	0	$\pi/4$	0	1	$7\pi/4$	$3\pi/2$
1	0	$3\pi/4$	0	1	$7\pi/4$	1	1	$5\pi/4$	$3\pi/2$
1	0	$3\pi/4$	1	0	$3\pi/4$	0	0	$\pi/4$	$3\pi/2$
1	0	$3\pi/4$	1	1	$5\pi/4$	1	0	$3\pi/4$	$3\pi/2$
1	1	$5\pi/4$	0	0	$\pi/4$	0	0	$\pi/4$	0
1	1	$5\pi/4$	0	1	$7\pi/4$	0	1	$7\pi/4$	0
1	1	$5\pi/4$	1	0	$3\pi/4$	1	0	$3\pi/4$	0
1	1	$5\pi/4$	1	1	$5\pi/4$	1	1	$5\pi/4$	0

Looking at the first, second and last columns of the table above, it can be concluded that the precoder provides differential phase coding for all combinations of the message bits and previously transmitted symbols. This differential output drives the IQ modulators to modulate the phase of the orthogonally polarised signals. In this way, DP-DQPSK modulation is achieved and its setup is shown in Figure 40.
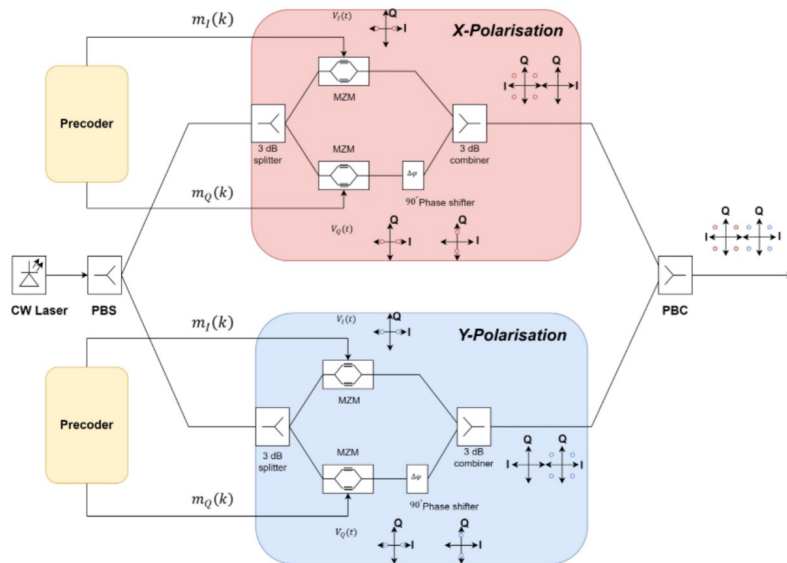
Figure 40: DP-DQPSK Transmitter.

4.1.2 DP-DQPSK receiver

As mentioned earlier, the DQPSK receiver does not need a local oscillator to demodulate the received signal, since the phase difference between current and previous symbol is obtained using the direct detection method with delay line interferometer [10]. Therefore, the system complexity is lower compared to the coherent receiver and it is shown in Figure 41.
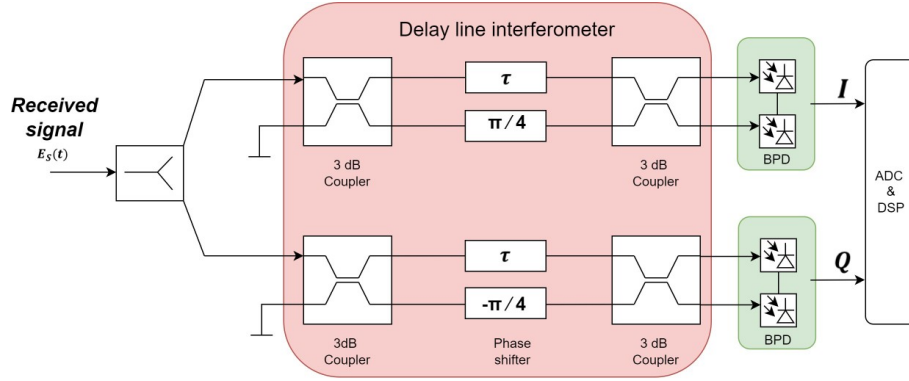
Figure 41: DQPSK receiver [10].

Where,

$$I = Cos(\frac{\pi}{4} + \Delta\theta)$$
$$Q = Sin(\frac{\pi}{4} + \Delta\theta)$$

(4.3)

From the Equation 4.3, the in-phase and quadrature phase components of the signal are obtained. This received signal is then processed by the ADC and DSP unit. The bit mapping of the demodulated signal is shown in Table 15.

Table 15: DQPSK demodulation bit mapping [10].

$\Delta\theta$	I	Q	$LogicI$	$LogicQ$
0	$1/\sqrt{2}$	$1/\sqrt{2}$	1	1
$\pi/2$	$-1/\sqrt{2}$	$1/\sqrt{2}$	0	1
π	$-1/\sqrt{2}$	$-1/\sqrt{2}$	0	0
$3\pi/2$	$1/\sqrt{2}$	$-1/\sqrt{2}$	1	0

The receiver setup of the DP-DQPSK system is shown in Figure 42, where the PBS splits the received signal into two orthogonal polarisations and demodulation is performed using two delay line interferometers. The delay line interferometer consists of two 2×2 couplers with a delay line on one branch and $\pm\pi/4$ phase

shifter on another branch to demodulate the DQPSK signal, followed by balanced photodetector, ADC and DSP unit.
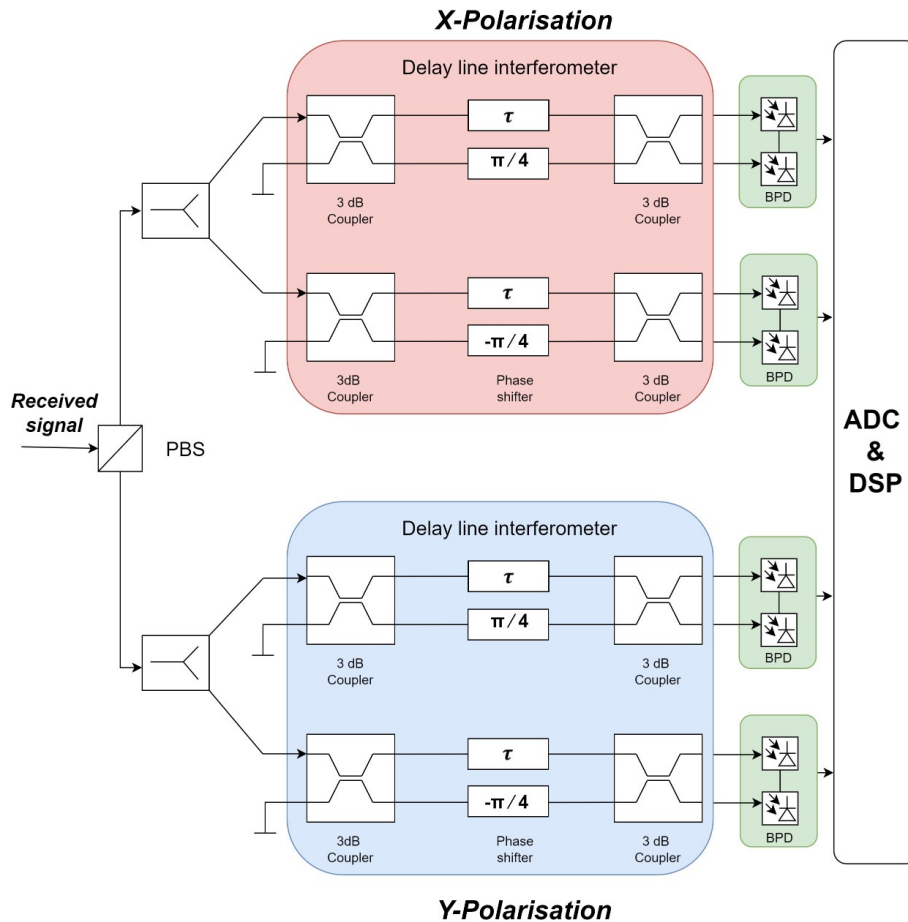
Figure 42: DP-DQPSK receiver

Alternative DP-DQPSK receiver setup

The article *"A low-cost alternative scheme to detect a 100 Gbps PM-DQPSK signal"* by *Chen et al., 2014* [26] discusses the alternative low-cost receiver approach for polarisation multiplexed DQPSK receiver. Where, the DQPSK received signal is demodulated by converting the phase shift keying signal to a polarisation shift keying (PolSK) signal using a tunable birefringent element. A time delay of one symbol period is then introduced between the two orthogonal polarisation states. The PolSK signals are then converted into two intensity modulation signals by a PBS. Since the DP-QPSK signal already consists of a DQPSK signal in the orthogonal polarisation states, to avoid interference existing between the two converted PolSK signals, the birefringent element is replaced by a polarisation rotator and a fiber delay line as

shown in Figure 43. In the low-cost alternative receiver setup, the signal is split into
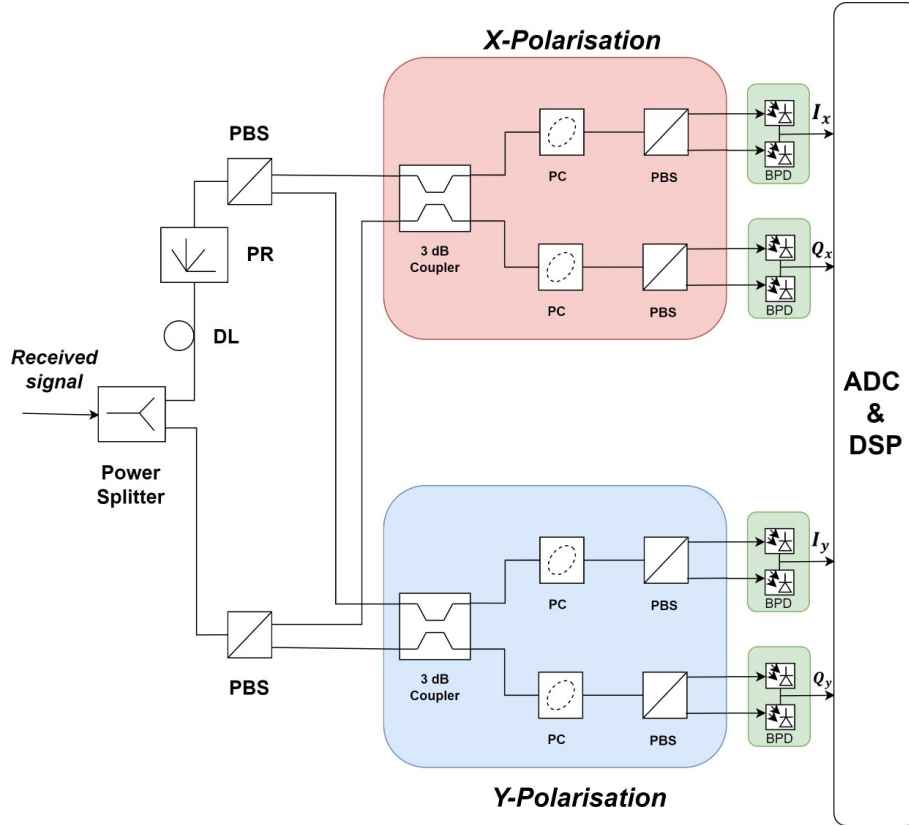
Figure 43: Alternate PD-DQPSK receiver setup [26].

two halves using a 3 dB power splitter. One signal is connected directly to a PBS and is split into two orthogonal polarisation sub-beams. The other signal passes through a delay line (DL) of one symbol period and a polarisation rotator(PR) with an rotation angle of 90°. It is then split into two orthogonal polarisation sub-beams by the PBS. These sub-beams from the delay line branch and the other branch are then coupled by two 2×2 couplers, the outputs of which are then given to the polarisation controller (PC) and the PBS to obtain the corresponding amplitude of the PolSK signal. Where, the PC is used to generate $+45°$ and $-45°$ phase difference between the two orthogonal polarisation signals. The output power of balanced photodetectors are given as

$$I_{x/y} = \frac{\sqrt{2}}{4} \vec{E}_{x/y}^{\ 2} [Cos(\Delta\theta) - Sin(\Delta\theta)] \tag{4.4}$$

$$Q_{x/y} = \frac{\sqrt{2}}{4} \vec{E}_{x/y}^{\ 2} [Cos(\Delta\theta) + Sin(\Delta\theta)] \tag{4.5}$$

The bit mapping of the demodulated signal is shown in Table 16.

Table 16: DP-DQPSK demodulation bit mapping [26].

$\Delta\theta$	I_{xy}	Q_{xy}	$LogicI_{x/y} = X$	$LogicI_{x/y} = Y$
0	$1\sqrt{2}$	$1\sqrt{2}$	1	1
$\pi2$	$-1\sqrt{2}$	$1\sqrt{2}$	0	1
π	$-1\sqrt{2}$	$-1\sqrt{2}$	0	0
$3\pi2$	$1\sqrt{2}$	$-1\sqrt{2}$	1	0

Advantages of the alternative DP-DQPSK receiver:

- In a back-to-back operation without FEC technology, the sensitivity is -23.7 $\pm$ 0.2 dBm for a BER of E-12 and -27.4 ± 0.2 dBm for a BER of E-3 which is approximately 0.5 dB better sensitivity than the conventional DP-QPSK receiver with four delay line interferometers.

- In the case of DWDM high-speed optical networks, a signal may pass through a large number of Reconfigurable Optical Add-Drop Multiplexers (ROADM) and as a result, a filtering effect is applied to the signal. Therefore, the performance of the alternative DP-DQPSK receiver under cascaded narrow optical filtering is studied and the result shows that ten 50 GHz filters can be cascaded with a 1 dB OSNR penalty, which reduces the intersymbol interference (ISI) caused by the spectral bandwidth loss. Whereas in *"Direct Detection of 107-Gb/s Polarization Multiplexed RZ-DQPSK Without Optical Polarization Demultiplexing* by *S. Chandrasekhar et al.,2208* [27], only two 50 GHz filters can be cascaded with $\approx$1 dB OSNR penalty.

- As only one delay line is used, the proposed receiver easily be upgraded to a bit-rate tunable receiver using a tunable delay line.

Disadvantages of alternate DP-DQPSK receiver:

- In ideal conditions, the rotation angle of the polarisation rotator is 90°. However, it is highly difficult to maintain the rotation angle at 90° all the time under realistic conditions.

- If the rotation angle deviates from the ideal condition, signal distortion will increase and it will be difficult to maintain the system stability.

- Polarisation controllers and rotators are still immature components in the PIC technology. More number of these immature components are used in this receiver setup, which in turn can collapse the receiver system.

4.2 Performance Analysis

In chapter 2, it is discussed that the direct detection system has 6 dB and 3 dB penalty in SNR compared to the homodyne and heterodyne coherent receivers respectively. Looking at the advantages and disadvantages of the low-cost alternative DP-DQPSK receiver setup, it can be concluded that the direct detection receiver with a delay line interferometer is easy to implement on a photonic chip because it requires fewer polarisation control components. In addition to that, the performance of the alternative receiver is only 0.5 dB better than the direct detection receiver, which is negligible at the scale of a 100 Gbps system.

Therefore, before performing the simulations to evaluate the performance of the DP-DQPSK system under different system noise conditions, its receiver chip area requirement should be estimated in order to evaluate the size index of the C-SWaP metrics.

4.2.1 Delay line calculation

To estimate the area of the DP-DQPSK receiver, the length of the delay line must be calculated. Therefore, the length of the delay line is calculated as follows,

The refractive index (η) of InP at 1550nm wavelength [28] = 3.1649.

Speed of light in InP = $0.9479 * 10^8$

One symbol duration = $\frac{1}{25GHz} = 40\,ps$

Distance or equivalent length of one symbol period = $40 * 10^{-12} * 0.9479 * 10^8$ $\approx 3.8\,mm$ or $3800\,\mu m$

Therefore, the 100G DP-DQPSK system requires a delay line of $\approx 3800\mu m$ at the receiver to demodulate the signal.

4.2.2 Delay line PIC layout

The delay line of $3800\mu m$ is designed using the Nazca design tool and the PIC layout of delay line interferometer is shown in Figure 44. The received signal is passed through a 2×2 coupler and one of its outputs is fed to the delay line of one symbol period, which is designed as a spiral waveguide structure to reduce the overall component area. The other output is directly connected to one of the inputs

of the second coupler, as shown in Figure 41 and a phase shift of $\pm\pi/4$ is introduced using a thermo-optical phase shifter whose electrodes are placed in parallel to the directly connected waveguide. The thermo-optical(tunable) can also counter the potential fabrication errors in the path lengths.
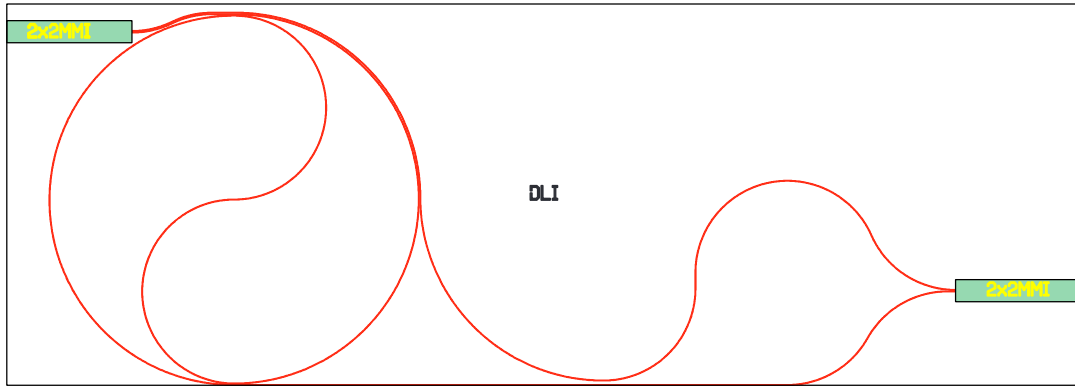
Figure 44: Delay line PIC layout.

4.2.3 DP-DQPSK PIC layout

The PIC layout of the 100G DP-DQPSK system in an $8 \times 12mm^2$ chip is shown in Figure 45. In terms of the transmitter, the layout remains the same, because the differential precoder is a separate electronic subsystem. At the receiver, the four delay line interferometer units are placed between the balanced detector and the PBS.

This layout shows that there is not enough chip area for optical (gray) routing between DLIs and BPDs. Similarly, there is not enough space for splitters and polarisation rotators to feed the signal from the PBS to the DLIs. Also, some metal routing overlaps with optical components, which means more area is needed to reroute the metal connections. Therefore, it can be concluded that a 100G DP-DQPSK system cannot fit on the same chip size as DP-DQPSK and requires a larger PIC size by approximately a few mm^2.
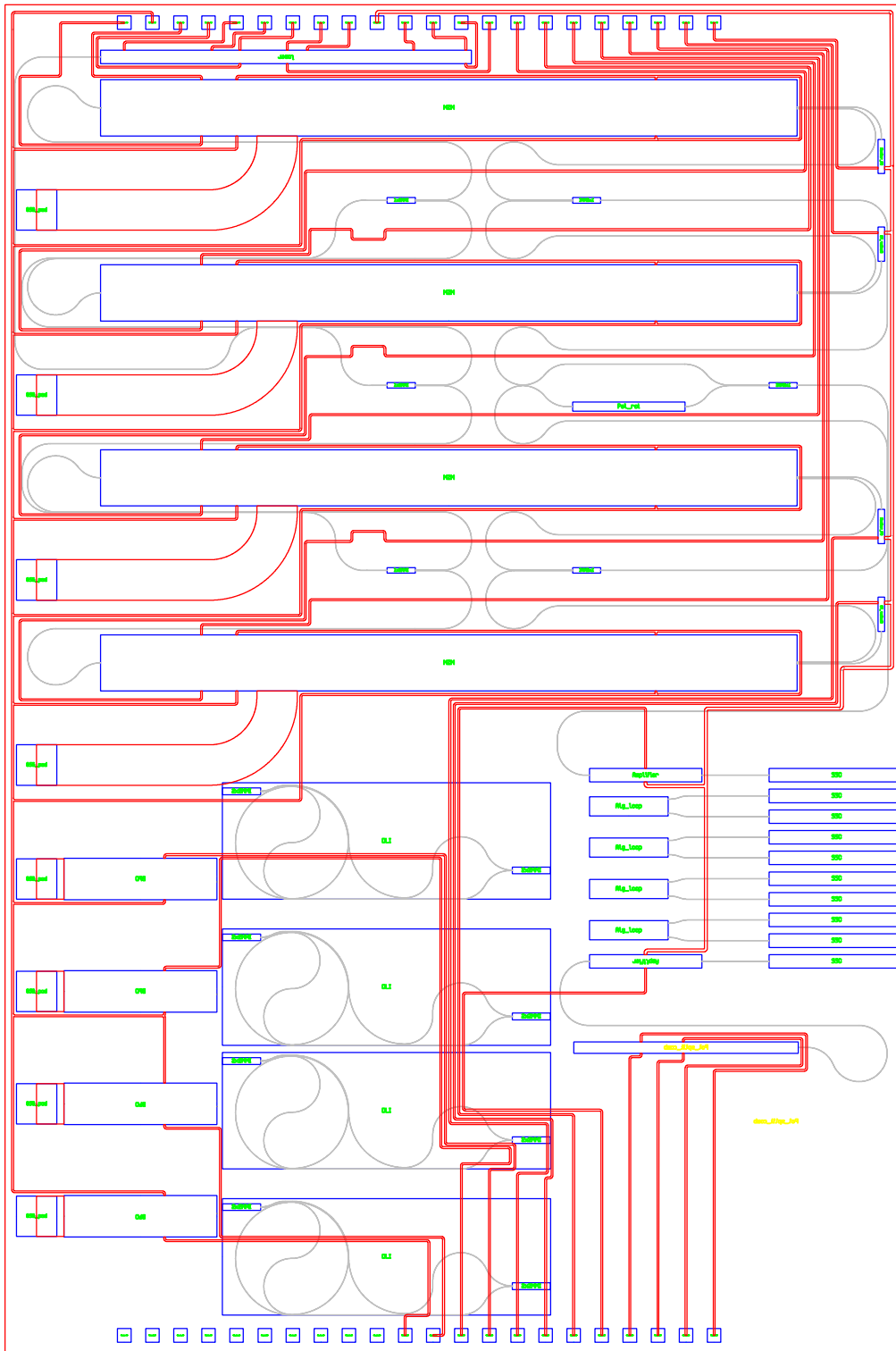
Figure 45: DP-DQPSK PIC layout.

4.3 Conclusion

From the DP-DQPSK PIC layout, it is clear that the DP-DQPSK receiver cannot be designed within the given 8×12 mm^2 chip area. Therefore, the required PIC area for the 100 Gbps DP-DQPSK system is larger compared to the DP-QPSK system. Also, theoretically, the SNR penalty is at least 3 dB for the direct detection receiver compared to the coherent receiver. Therefore, it can stated that the DP-QPSK system has multiple advantages over the DP-DQPSK system considering the C-SWaP metrics. As a result, no further noise analysis is performed for the DP-DQPSK system.

5 DWDM System

In this chapter, the throughput scale-up potential of a single 100G system up to four channels using dense wavelength division multiplexing is analysed using the Optisystem simulation tool. From the chapters 3 and 4, it is concluded that PD-QPSK system has a better C-SWaP performance compared to PD-DQPSK system. Therefore, a four channel DWDM PD-DQPSK system of 100 Gbps each is stimulated. Its performance is analysed with and without parametric non-linear effects induced by the EDFA such as self-phase modulation (SMP), cross-phase modulation (XPM) and four wave mixing (FWM).

5.1 Theoretical overview on DWDM system

Today, the telecommunications industries relies on DWDM technology to maximise the capacity and efficiency of the communications network. In optical DWDM, the number channels is densely packed across the communication spectrum, with approximately 160 channels [29].

In most cases, the channel spacing is minimised to only 0.4 nm to 0.8 nm, which is why it is called as dense wavelength division multiplexing. DWDM is also protocol and bit rate independent [29]. The main optical components of a DWDM system are the optical multiplexers (Mux) and demultiplexers (DeMux).

Optical Mux/DeMux is a passive component used to multiplex and demultiplex the multichannel optical signal at the transmitter and receiver respectively, as shown in Figure 46. The multiplexer at the transmitter combines the signals from different channels into a composite signal according to the specified channel spacing [29]. The DeMux at the receiver, separates the channels from the composite signal according to the specified channel spacing and each channel is then processed separately. As the optical Mux and DeMux are passive components, they have a low insertion loss

and no external power is required to multiplex and demultiplex the optical signal [29].
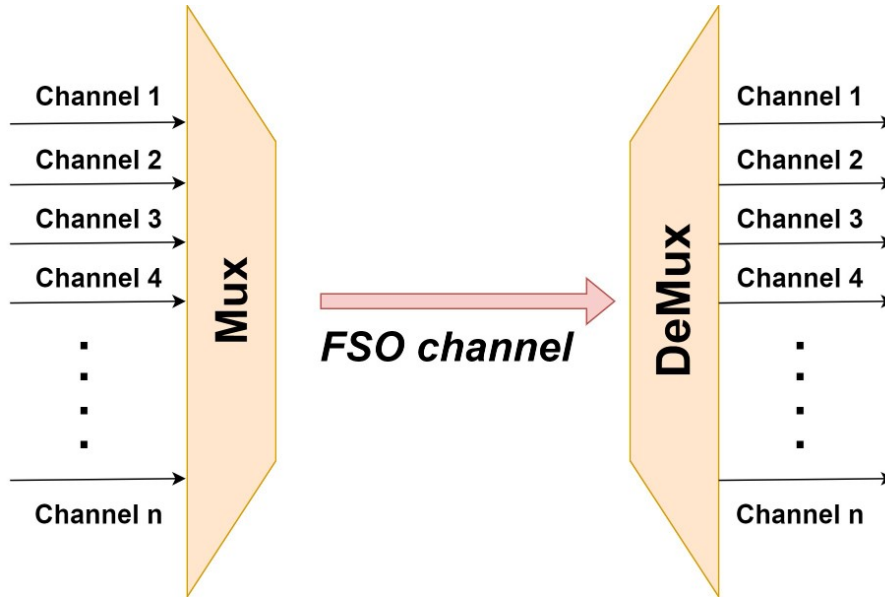
Figure 46: DWDM system [29].

In an FSO-based DWDM system, the performance is mainly affected by the non-linear effects of EDFA. As the intensity of the optical pulse propagating in the fiber increases, the magnetic field associated with the pulse changes the refractive index of the medium and affects the signal. This phenomenon is known as the 'non-linear Kerr effect'. Especially, at the booster amplifier the transmit signal power is amplified to a high power to accommodate the link loss, by which the signal power enters the non-linear regime of optical fiber and signal impairment occurs. This non-linear response of the fiber due to the change in refractive index caused by the non-harmonic motion of electrons under the influence of an applied field. Therefore, due to the non-linear electromagnetic field the total polarisation P induced by electric dipoles is also non-linear and directly proportional to the incident electric field intensity [30] [31]. It is given by,

$$P = \varepsilon_0(\chi^{(1)}.E + \chi^{(2)}.EE + \chi^{(3)}.EEE + ...) \tag{5.1}$$

Where, ε_0 is the vacuum permittivity and χ^j is a different orders of susceptibility. The non-linear effects such as self-phase modulation(SPM), cross-phase modulation(XPM) and four wave mixing(FWM) arise from the third order susceptibility($\chi^{(3)}$). The most prominent parametric non-linear effects in an FSO-based multichannel optical systems are XPM and FWM. Therefore, the effects of XPM and FWM are

analysed in this thesis.

5.1.1 Cross phase modulation (XPM)

XPM occurs in a multi-channel DWDM system due to the change in the non-linear refractive index of the propagation medium caused by the magnetic fields of all copropagating beams from different channels. Therefore, the intensity fluctuation of one channel causes the phase fluctuation of other copropagating channels. Due to the XPM, the copropagating beams of different wavelengths overlap, resulting in asymmetric spectral broadening with distortion, which increases the BER [32].

5.1.2 Four wave mixing (FWM)

When more than one optical channel is transmitted over the same channel with equal channel spacing, unwanted signals are produced at different wavelengths due to third order nonlinear susceptibility, called as four wave mixing (FWM). In terms of two channel system at frequencies ω_1 and ω_2 with equal channel spacing, the additional unwanted signals are produced at frequencies $(2\omega_1 - \omega_2)$ and $(2\omega_2 - \omega_1)$ as shown in Figure 47. These side bands propagate with the signal and reduce its strength. Therefore, FWM is the main problem in a DWDM system because as the number of channels increases, the side bands due to FWM also increase and drastically reduce the system performance by increasing the bit error rate. The number of unwanted signals generated by FWM can be calculated using the Equation 5.2 [32].

$$k = (N^3 - N^2)/2 \tag{5.2}$$

Where, K is number of additional unwanted signals generated and N is the number of channels transmitted.
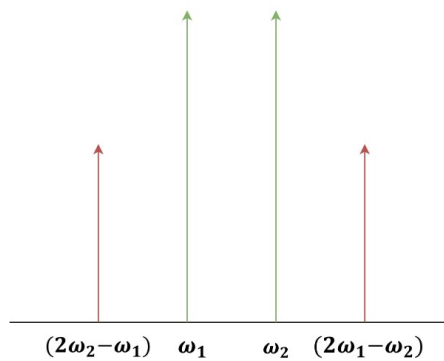
Figure 47: FWM [32].

In order to investigate the scaling up potential of a four channel PIC based 100 Gbps DP-QPSK system, the non-linear effects such as XPM and FWM should be analysed. Therefore, in the next section the four channel DWDM system is simulated with and without non-linear effects using Optisystem and the results are discussed.

5.2 Simulation setup

First, the same system setup of a 100Gbps DP-QPSK system in Optsim is replicated in optisystem. Then the BER performance is analysed and also the system performance with laser phase noise is analysed by introducing a laser line width of 700 KHz . Therefore, the Geo link loss(Channel loss) Vs BER performance of the simulation model in Optsim and Optisystem is shown in Figure 48. In optisystem, the simulations are performed with 65000 bits in order to reduce the simulation time.
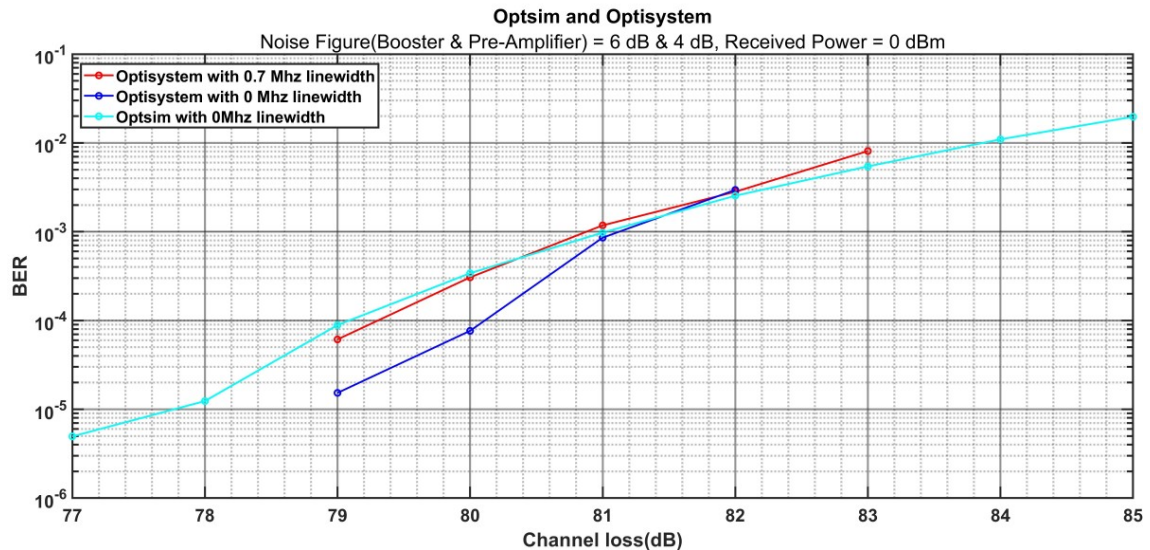
Figure 48: PD-QPSK system performance in Optisystem and Optsim.

From the above graph, it is observed that at BER of 1E-3, the Optsim and Optisystem results for the 0 MHz linewidth sytems are matching with each other. But the 0.7 MHz linewidth system has ≈0.2 dB penalty in terms of the GEO link loss allowance in compared to the 0 MHz linewidth system. It was observed that the Optisystem BER curve diverges drastically from the Optsim BER curve below 81 dB link loss. This is due to the lower number of simulation bits, which reduces the accuracy in the simulation engine when calculating lower bit rates. However, the DP-QPSK system performance with narrow linewidth of 700 KHz still supports the GEO link loss budget of 75.3 dB. The four channel DP-QPSK system is modelled

in Optisystem using the transmitter and receiver setup shown in Figure 49, and the channel link with DWDM system components shown in Figure 50 .

The general EDFA model in Optisystem does not include non-linear effects, so an optical fiber is added after EDFA to include the EDFA's gain medium non-linear effects such as SPM, XPM and FWM.

Since the booster amplifier has a longer gain medium and high output power compared to the pre-amplifier in the FSO system, the non-linear effects of the booster amplifier is strong. Therefore, the degradation of the system performance due to the non-linear effects of booster amplifier of a length 50m is analysed in this thesis.

The four channels are simulated with equal channel spacing of 0.8 nm (100 GHz according to the ITU standard) at wavelengths 1550nm, 1550.8nm, 1551.6 nm and 1552.4 nm respectively.

5.3 Results and discussion

5.3.1 System without non-linear effects

First, the four channel DWDM system for the GEO link is simulated without including nonlinear effects in the EDFA. Its transmitted optical output spectrum is shown in Figure 51a and the received signal spectrum is shown in Figure 51b.

It is observed that, without the non-linear effects in the EDFA, the transmitted spectrum and received spectrum have peaks at the center frequencies of corresponding channels with distortion due to the noise added by the system. The received spectrum has less power due to the channel attenuation of 78 dB and is closer to the noise floor. The received signal is demultiplexed using a DeMux and the channels are selected using dedicated 50 GHz bandwidth optical filters. The filtered signals are then fed to the coherent receivers to demodulate the corresponding DP-QPSK signals and post-processed using DSP. To evaluate the signal quality, the received signal spectrum of each channel after optical filtering is examined and the constellation diagram of the demodulated signal before and after DSP is viewed.
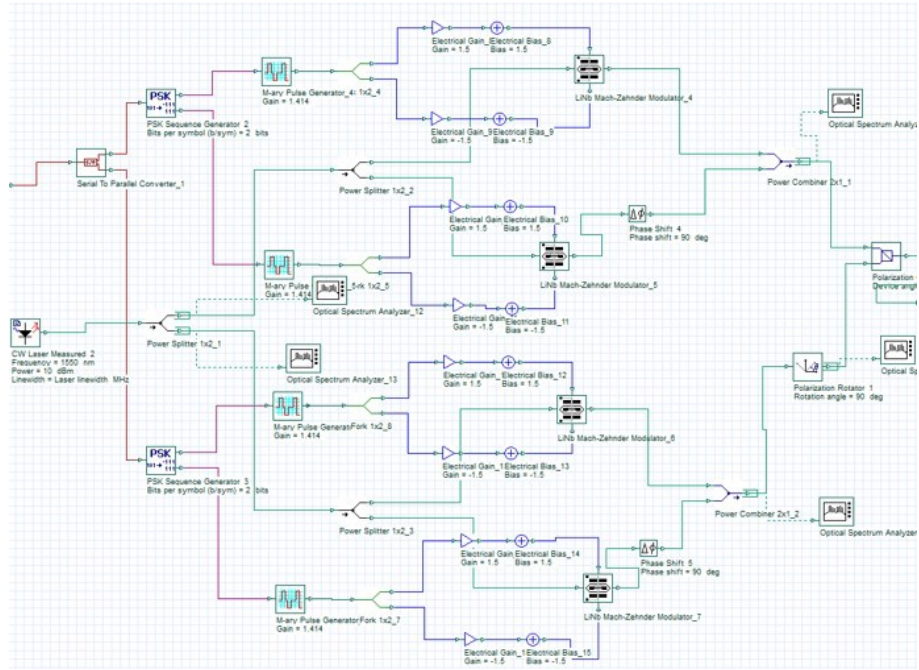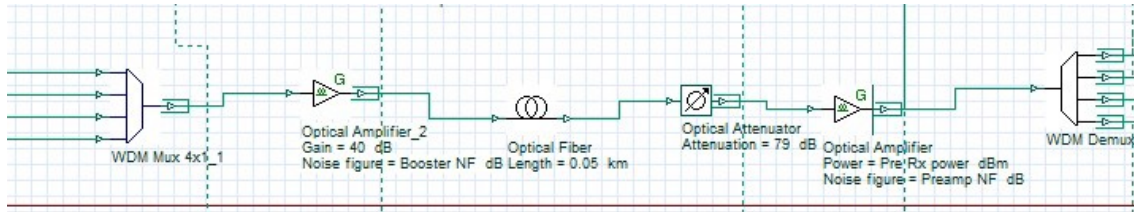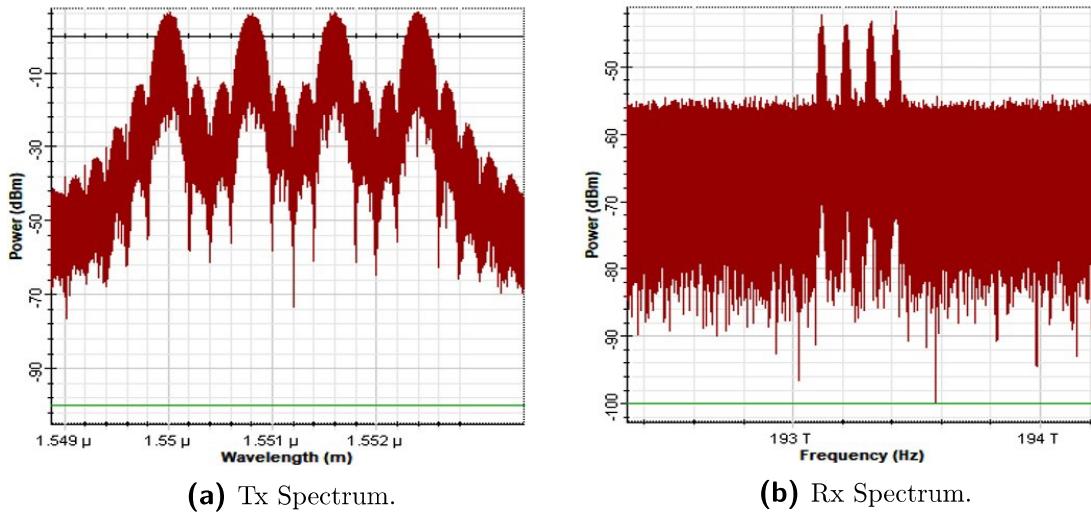
(a) DP-QPSK Transmitter.
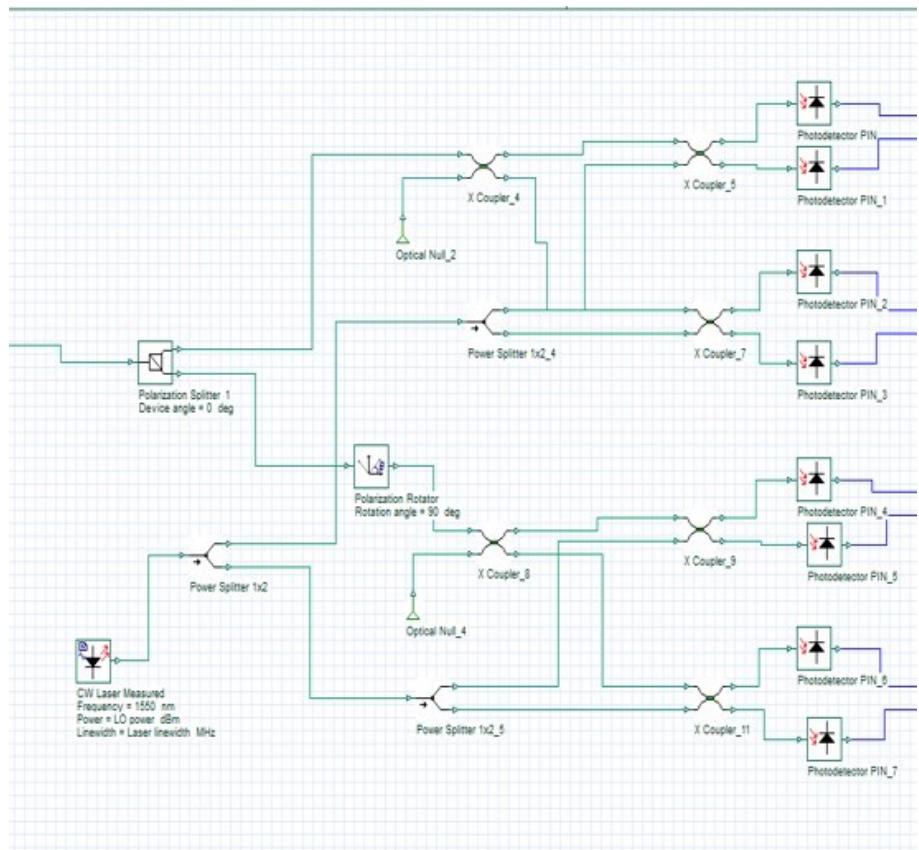
(b) DP-QPSK Receiver.

Figure 49: DP-QPSK system simulation model in Optisystem.

Figure 50: Four channel DWDM link.

(a) Tx Spectrum.

(b) Rx Spectrum.

Figure 51: DWDM signal spectrum.

The filtered optical signal spectrum of each channel is shown in Figure 52. All the channel spectrum have a peak at their center frequency and signals outside the filter bandwidth are removed. All the spectrum also contain distortion due to the dominant ASE noise from the EDFA. No cross talk between the channels is observed.

Channel 1's constellation diagram of both polarisations is shown in Figure 53. It can be seen that before DSP the symbols are scatter around the DC point or center and grow away. After performing, timing recovery, frequency offset compensation and phase offset compensation using DSP, the symbols are recovered and scattered around their respective symbol boundaries in the IQ plot. The same result is observed in all four channels.

(a) Channel 1.

(b) Channel 2.

(c) Channel 3.
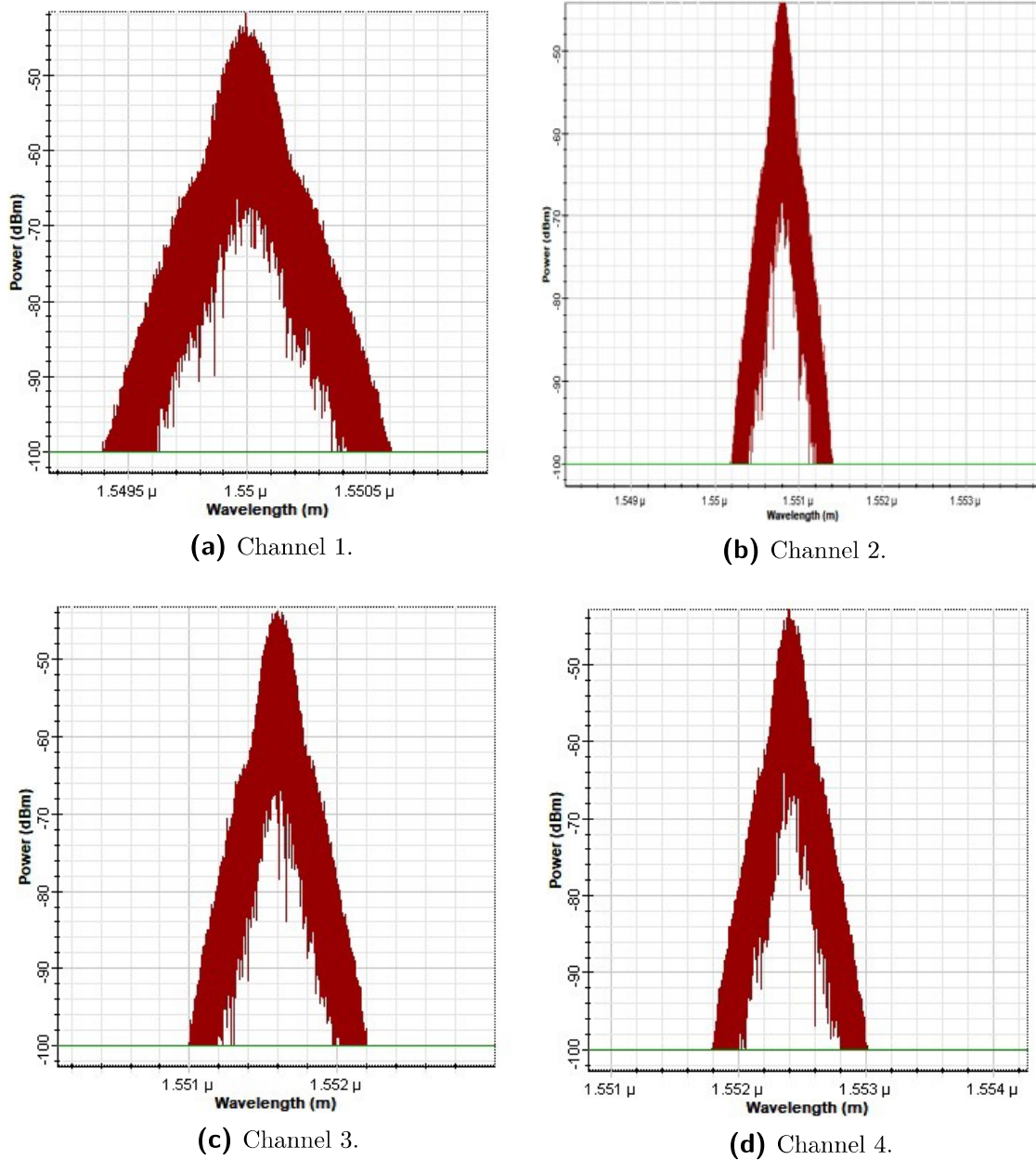
(d) Channel 4.

Figure 52: Received signal spectrum after optical filter.

Therefore, it can be concluded that, if the system operates without any non-linear effects then the performance of the four channel DP-QPSK system is not affected for GEO satellite link assuming that the insertion loss in Mux/Demux is minimal.

(a) X-pol before DSP.

(b) X-pol after DSP.

(c) Y-pol before DSP.

(d) Y-pol after DSP.
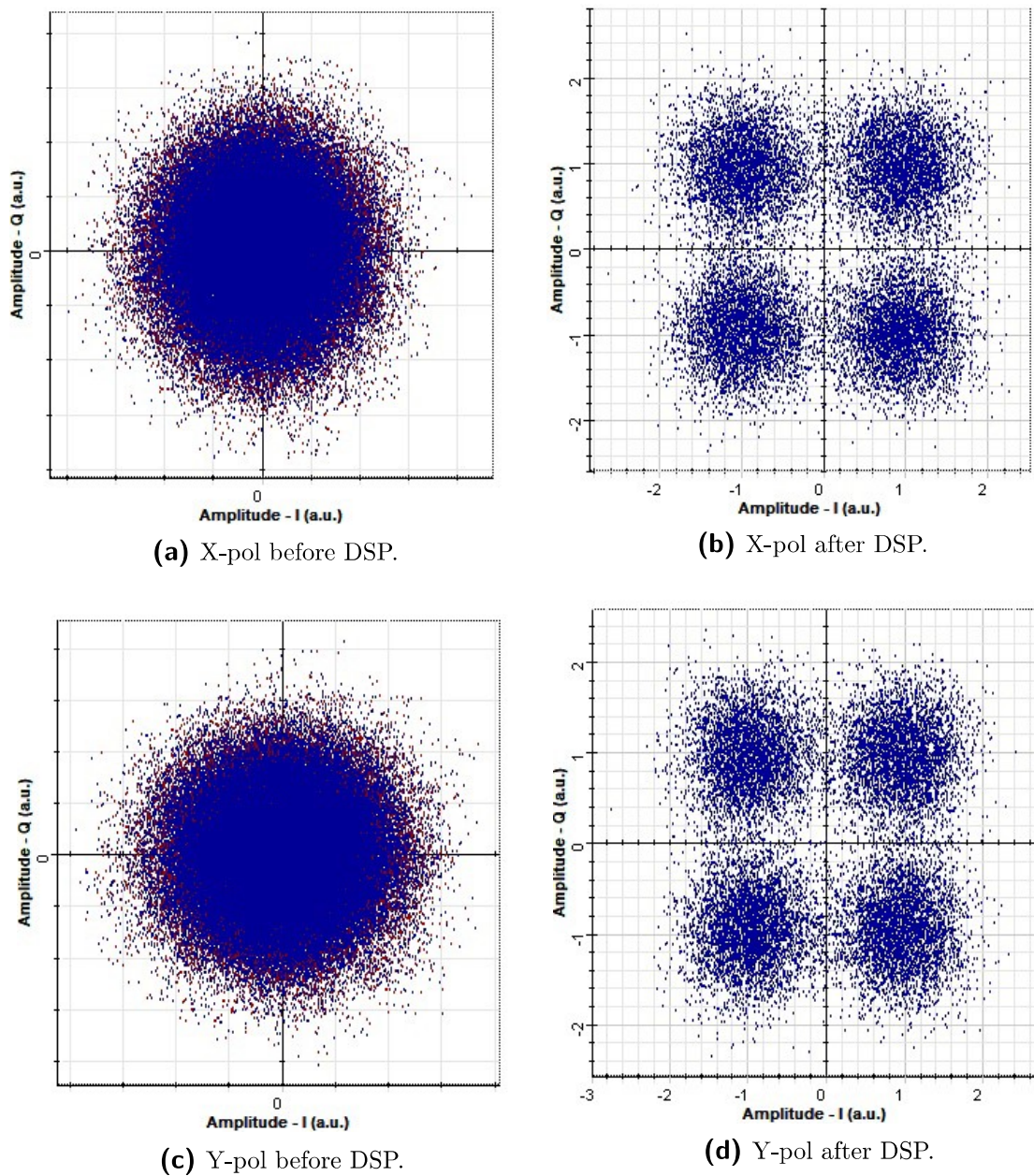
Figure 53: Channel 1 - constellation diagram.

5.3.2 System with non-linear effects

The XPM and FWM are activated in the booster amplifier and the system performance is evaluated in this section. The transmitted and received signal spectra are shown in Figure 55.

The transmitted spectrum shows that the channels have crossed their channel spacing and cross-talk is observed. The spectrum is completely distorted and several frequency peaks other than the respective center frequencies of the four channels

(a) Tx Spectrum.
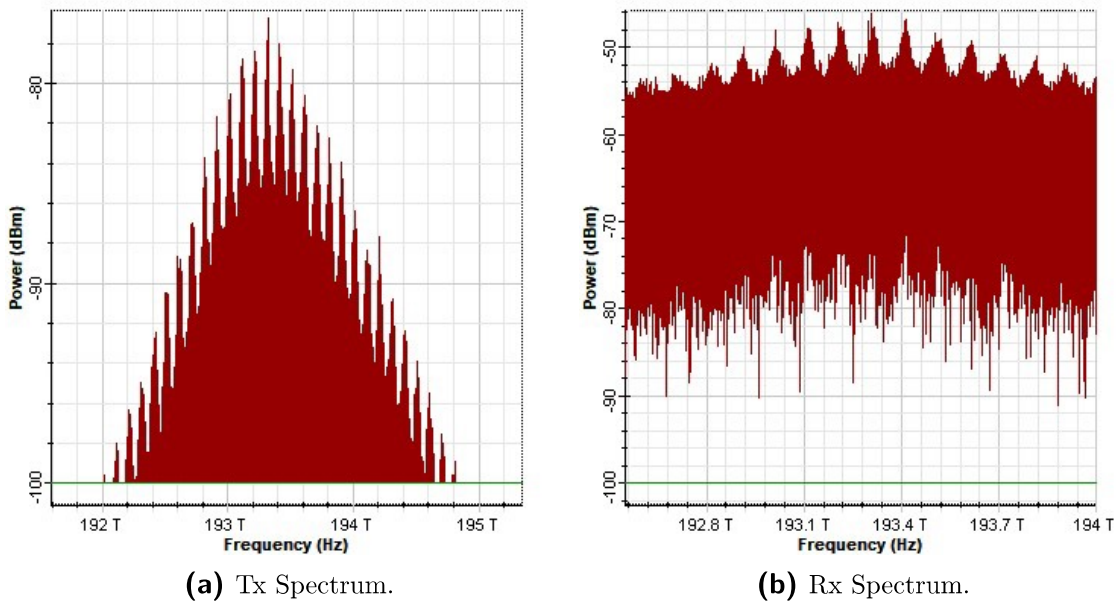
(b) Rx Spectrum.

Figure 54: DWDM signal spectrum with non-linear effects

are observed. From the Equation 5.2, the number of extra signals generated by FWM can be calculated as follows,

$$k = (N^3 - N^2)/2 = (4^3 - 4^2)/2 = 24 \tag{5.3}$$

Where, number of channels $N = 4$. In Figure 54a, 24 additional peaks are observed, confirming that FWM is present in the system. The spectrum is also broadened by XPM, making the spectrum completely distorted and introducing cross-talk between the channels. The received spectrum shown in Figure 54b at 78 dB link loss is highly distorted and close to the noise floor. It is therefore essential to look into the spectrum after the demux and optical filter to assess whether the symbols can be recovered by the coherent receiver and DSP.

From Figure 55, it is observed that the extra unwanted frequencies due to FWM are removed by optical filtering in all four channels. However, at FWHM the spectrums are completely distorted and noisy, implying that the signal eye is completely closed. This is due to the non-linear effects present in the system. To confirm this, the spectrum before optical filtering is shown in Figure 56, where the cross talk frequencies are observed in all four channels with spectrum broadening due to FWM and XPM. Due to non-linear effects, the received signal quality and the system performance are drastically reduced. As a result, the system is unable to recover the symbols even after performing symbol recovery algorithms using DSP, which can be observed in the constellation diagram of channel 1 shown in Figure 57, where the symbols are

(a) Channel 1.

(b) Channel 2.

(c) Channel 3.
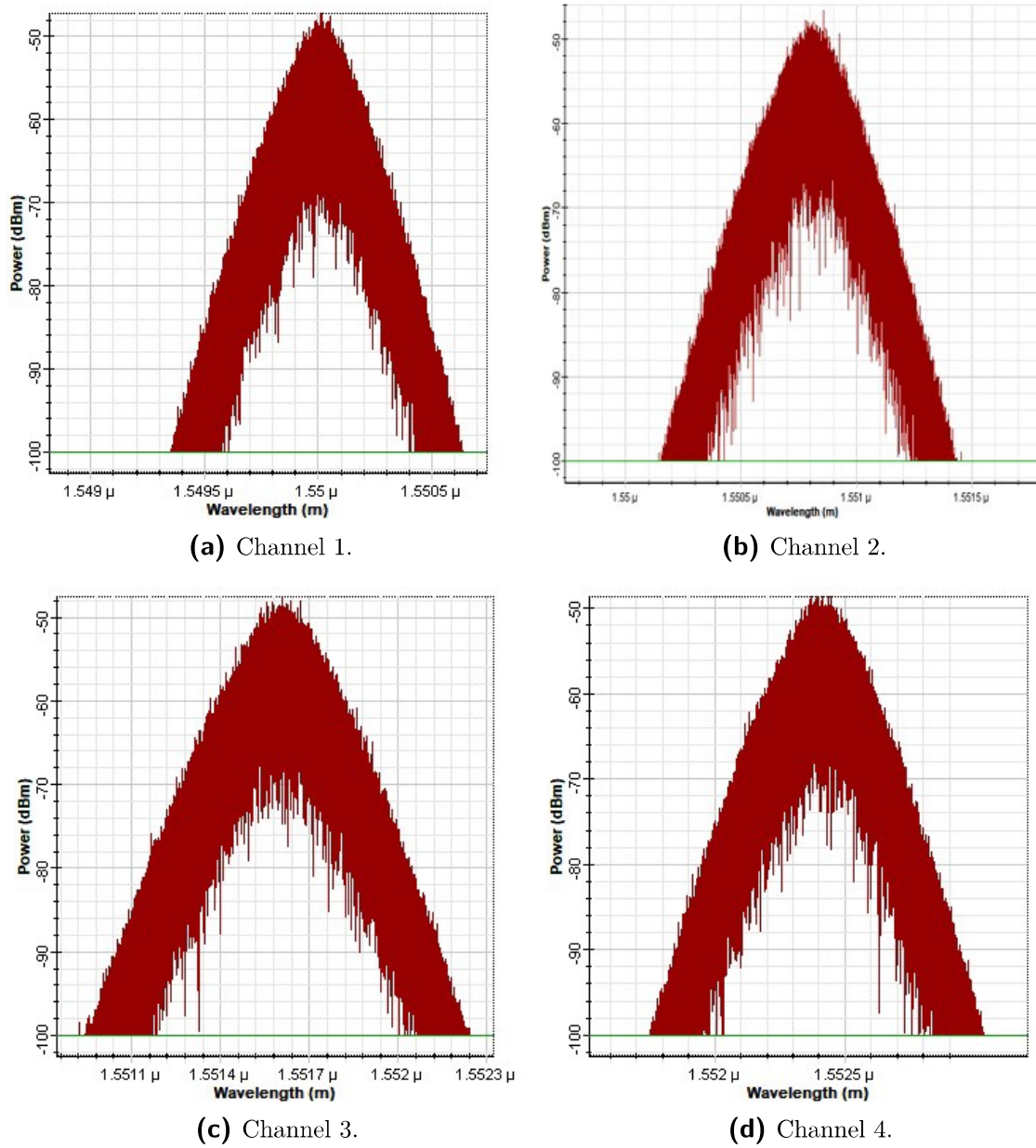
(d) Channel 4.

Figure 55: Received signal spectrum after optical filter with non-linear effects.

still scattered away from their respective symbol boundaries after DSP. The same response in the constellation diagram of other channels was observed.
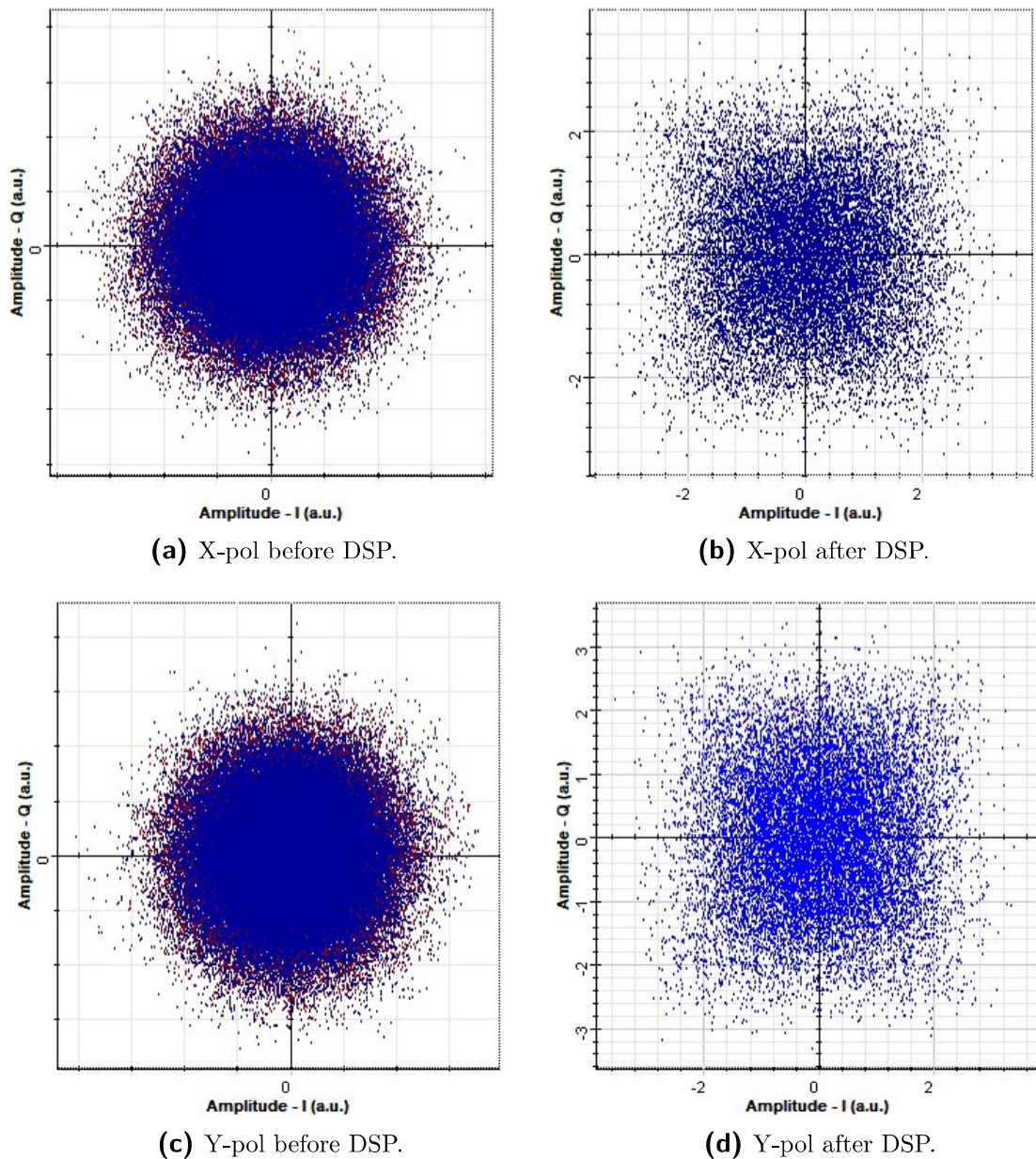
(a) Channel 1.

(b) Channel 2.

(c) Channel 3.

(d) Channel 4.
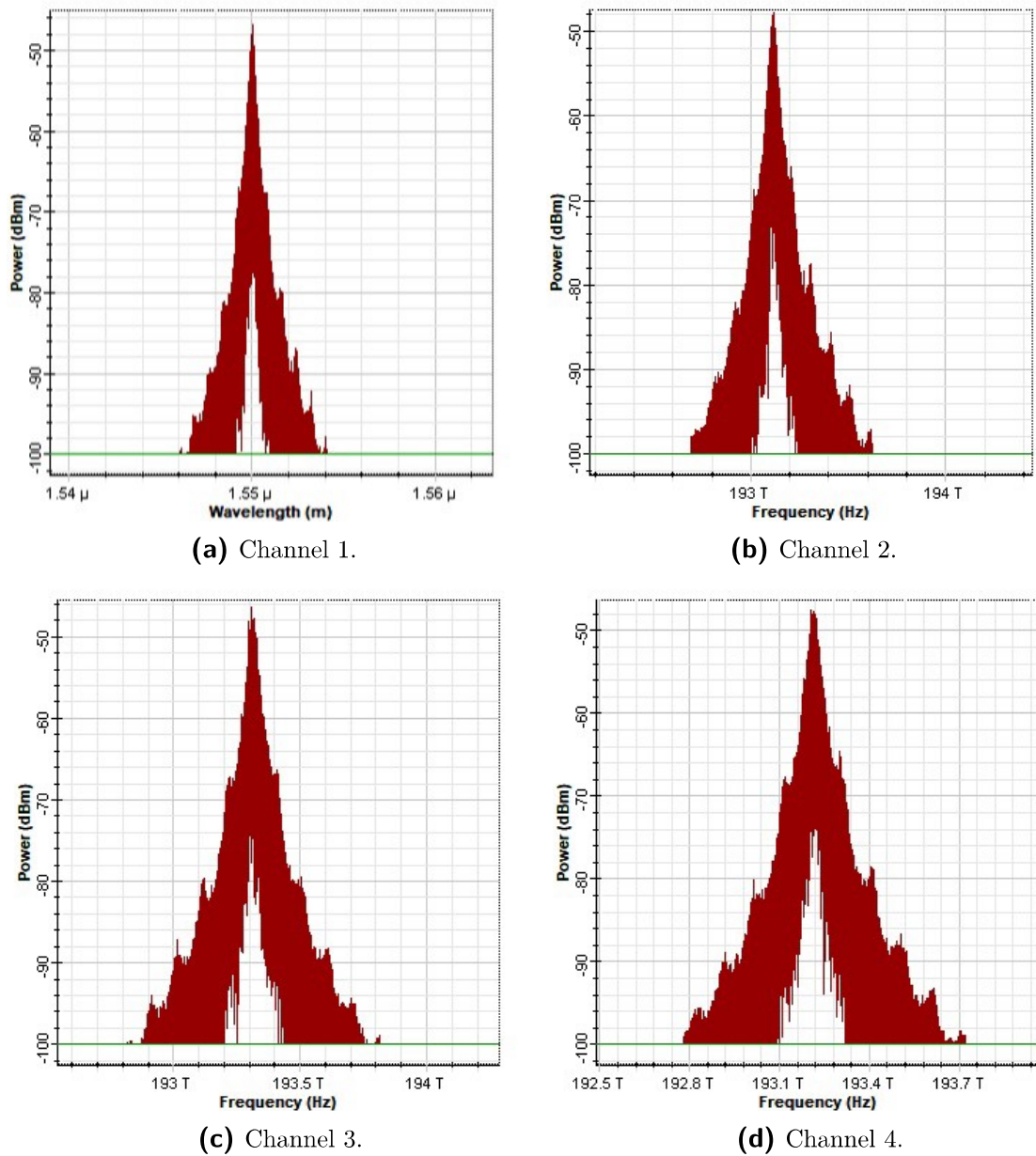
Figure 56: Received signal spectrum before optical filter with non-linear effects.

From the Figures 57b and 57d, it can be seen that the DSP unit is not able to recover the symbols due to the non-linear effects.

5.3.3 Suggestions for non-linear effects mitigation technique

From the analysis of the four channel DP-QPSK system with and without non-linear effects, it can be concluded that non-linear effects completely distort the system performance. Therefore, these non-linear effects should be reduced to improve the system performance.

(a) X-pol before DSP.

(b) X-pol after DSP.

(c) Y-pol before DSP.

(d) Y-pol after DSP.

Figure 57: Channel 1 - constellation diagram with non-linear effects.

The effects of XPM can be mitigated by adding some chromatic dispersion, which acts in the opposite direction to broadening of the signal and cancels out the XPM effects [32].

On the other hand, the FWM effect can be reduced by making the channel spacing uneven so that the unwanted signals disappear [32]. Therefore, system with appropriate dispersion coefficient and unequal channel spacing is suggested to improve the DWDM system performance.

6 Conclusion

In this thesis, a quantitative study of GEO satellite to ground FSO communication link supporting ≥ 100 Gbps based PIC technology is investigated. The review on different modulation formats to perform 100Gbps data rate communication is done to access their performance metrics such as OSNR, spectral efficiency, coding efficiency and system complexity. From which the two overall best performing systems are selected namely DP-QPSK and DP-DQPSK. The performance of the DP-QPSK system is evaluated by simulating the system under different system noise conditions and it is concluded that the pre-amplifier ASE noise is the important system performance limiting parameter. The PIC layout for the DP-QPSK system is designed based on the InP PIC foundry specification and its optical, electrical and RF routing is optimised according to the foundry guidelines.

In terms of PD-DQPSK system, a conventional receiver with four delay lines and an alternative low cost receiver from a review paper are compared according to their performance and system implementation. As a result, the conventional receiver setup is selected for the PIC based system. From the theoretical comparison of the performance penalty between the DP-QPDK system and the DP-DQPSK system, it is concluded that the DP-QPSK system has better OSNR. Therefore, before performing simulations to analyse the effect of system noise on PD-DQPSK system performance, its PIC size is compared with DP-QPSK PIC size to determine whether PD-DQPSK system has size advantage. So, the delay line length is calculated and its PIC layout is designed. Then, using this delay line layout, the PIC layout of the PD-DQPSK system is designed and analysed. As a result, it is found that the DP-DQPSK system cannot be designed within the given chip size due to large delay line size. Therefore it is concluded that the DP-QPDK system has theoretically better performance than the DP-DQPSK system and it requires smaller chip area compared to the DP-DQPSK system implementation.

The scalability of the DP-QPSK system using DWDM technique is investigated. The performance of the four channel DWDM system decreases significantly when non-linear effects such as XPM and FWM are included in the system. The mitigation techniques to reduce the non-linear effects are suggested, such as the inclusion of chromatic dispersion and asymmetric channel spacing.

Future work

As the PD-QPSK system has a high performance index and its performance under different system noises for GEO satellite link loss is studied, it will also be useful to study the effects of space radiation on the PIC and how it affects the system behaviour. The effects of space radiation can be modelled as a background noise in the channel link using a simulation environment and its effects on the system performance can be studied to optimise the system characteristics.

In order to increase the link capacity using DWDM technology, the suggested mitigation techniques to reduce the cross talk can be analysed and the impact of other non-linear scattering effects such as Stimulated Raman Scattering (SRS) and Stimulated Brillion Scattering (SBS) can be investigated.

Bibliography

[1] Ramon Mata Calvo et al. "Optical technologies for very high throughput satellite communications". In: *SPIE Photonics West LASE*. Vol. 109100. Proc. SPIE 10910, Free-Space Laser Communications XXXI. Querschnittsthema Global Connectivity. SPIE, Mar. 2019. URL: https://elib.dlr.de/126597/.

[2] Philip Conroy et al. "Demonstration of 40GBaud intradyne transmission through worst-case atmospheric turbulence conditions for geostationary satellite uplink". In: *Applied Optics* 57.18 (June 2018), pp. 5095–5101. URL: https://elib.dlr.de/120543/.

[3] Arun K. Majumdar. "Laser Satellite Communications: Fundamentals, Systems, Technologies, and Applications". In: *Laser Communication with Constellation Satellites, UAVs, HAPs and Balloons: Fundamentals and Systems Analysis for Global Connectivity*. Cham: Springer International Publishing, 2022, pp. 63–95. ISBN: 978-3-031-03972-0. DOI: 10.1007/978-3-031-03972-0_3. URL: https://doi.org/10.1007/978-3-031-03972-0_3.

[4] Dimitar Radkov Kolev et al. "Latest Developments in the Field of Optical Communications for Small Satellites and Beyond". In: *Journal of Lightwave Technology* 41.12 (2023), pp. 3750–3757. DOI: 10.1109/JLT.2023.3276981.

[5] Katherine Schauer Catherine G. Manning. *Optical Communications*. URL: https://www.nasa.gov/technology/space-comms/optical-communications-overview/#section-5.

[6] Marcin Wojciech Ziarko, Giulio Terrasanta, and Ramon Mata Calvo. "Optical communications for very high throughput satellites". Advanced Photonics Congress 2021, virtual. July 2021. URL: https://elib.dlr.de/185595/.

[7] Hongwei Zhao et al. "Indium Phosphide Photonic Integrated Circuits for Free Space Optical Links". In: *IEEE Journal of Selected Topics in Quantum Electronics* 24.6 (2018), pp. 1–6. DOI: 10.1109/JSTQE.2018.2866677.

[8] G.P. Agrawal. *Fiber-Optic Communication Systems*. Wiley Series in Microwave and Optical Engineering. Wiley, 2012. ISBN: 9780470922828. URL: https://books.google.de/books?id=yGQ4n1-r2eQC.

[9] Fiberoptix Team. *Complete Guide To Optical Modulation Techniques*. 2024. URL: https://fiberopticx.com/optical-modulation-techniques/ (visited on 05/30/2024).

[10] Ariel Nachum Lian Zhao Hari Shankar. *40G QPSK and DQPSK Modulation*. 2014. URL: https://www.optiwave.com/wp-content/uploads/2014/04/40G-QPSK-and-DQPSK-Modulation.pdf (visited on 05/20/2024).

[11] Matthias Seimetz. "High-Order Modulation for Optical Fiber Transmission". In: 2009. URL: https://api.semanticscholar.org/CorpusID:107267920.

[12] Robert P. Dahlgren and Bob. Dahlgren. "NOISE IN FIBER OPTIC COMMUNICATION LINKS". In: 2001. URL: https://api.semanticscholar.org/CorpusID:7815560.

[13] Dr.Deepa Venkitesh. *Fiber Optic Communication Technology*. 2021. URL: https://www.youtube.com/playlist?list=PLyqSpQzTE6M8Ki6mNmm3RvFVmAlksTo_L (visited on 04/08/2024).

[14] R. Paschotta. *Relative Intensity Noise*. Nov. 2007. DOI: 10.61835/xx3. URL: https://www.rp-photonics.com/relative_intensity_noise.html (visited on 04/08/2024).

[15] Mohsen Ganjali and S. Esmail Hosseini. "Effects of frequency chirping and finite extinction ratio of optical modulators in microwave photonic IFM receivers". In: *Optics Communications* 452 (2019), pp. 380–386. ISSN: 0030-4018. DOI: https://doi.org/10.1016/j.optcom.2019.07.070. URL: https://www.sciencedirect.com/science/article/pii/S0030401819306625.

[16] synopsys. *Mach-Zehnder modulator*. URL: https://www.synopsys.com/glossary/what-is-a-mach-zehnder-modulator.html (visited on 04/08/2024).

[17] K. Anbarasi, C. Hemanth, and R.G. Sangeetha. "A review on channel models in free space optical communication systems". In: *Optics and Laser Technology* 97 (2017), pp. 161–171. ISSN: 0030-3992. DOI: https://doi.org/10.1016/j.optlastec.2017.06.018. URL: https://www.sciencedirect.com/science/article/pii/S0030399216315006.

[18] Esdras Anzuola Valencia. "Atmospheric compensation experiments on free-space optical coherent communication systems". In: 2015. URL: https://api.semanticscholar.org/CorpusID:111889226.

[19] Taissir Y. Elganimi. "Studying the BER performance, power- and bandwidth-efficiency for FSO communication systems under various modulation schemes". In: *2013 IEEE Jordan Conference on Applied Electrical Engineering and Computing Technologies (AEECT)*. 2013, pp. 1–6. DOI: 10.1109/AEECT.2013.6716426.

[20] keysight. *How Do I Measure the Bit Error Rate (BER) to a Given Confidence Level on the J-BERT M8020A and the M8040A High-Performance BERT?* URL: https://edadocs.software.keysight.com/kkbopen/how-do-i-measure-the-bit-error-rate-ber-to-a-given-confidence-level-on-the-j-bert-m8020a-and-the-m8040a-high-performance-bert-588276182.html.

[21] FOSCO. *MODULATION FORMATS FOR 100G AND BEYOND*. URL: https://www.fiberoptics4sale.com/blogs/archive-posts/95041158-modulation-formats-for-100g-and-beyond.

[22] R. Pradeep, K. C. Ravikumar, and S. b Umesh. "Comparative Analysis of Different Modulation Technique for Free-Space Optical Communication". In: 2018. URL: https://api.semanticscholar.org/CorpusID:212439339.

[23] Cisco. *Cisco Digital CFP2-DCO Coherent Optical Module Data Sheet.* URL: `https://www.cisco.com/c/en/us/products/collateral/interfaces-modules/transceiver-modules/datasheet-c78-743732.html`.

[24] GIGALIGHT. *GIGALIGHT 100G CFP DCO Optical Transponder GCF-S101-xx-xTCA.* URL: `https://www.gigalight.com/datasheets/100g-cfp-dco.pdf`.

[25] Matt Schmitt. *DATA TO SUPPORT 100G OPTICAL PARAMETER SELECTION.* URL: `https://www.ieee802.org/3/ct/public/19_05/` (visited on 05/13/2024).

[26] Xiaoyong Chen, Paloma R Horche, and Alfredo M Minguez. "A low-cost alternative scheme to detect a 100 Gbps PM-DQPSK signal". In: *Photonic Network Communications* 28 (2014), pp. 203–213.

[27] Sethumadhavan Chandrasekhar et al. "Direct Detection of 107-Gb/s Polarization-Multiplexed RZ-DQPSK Without Optical Polarization Demultiplexing". In: *IEEE Photonics Technology Letters* 20 (2008), pp. 1878–1880. URL: `https://api.semanticscholar.org/CorpusID:13452379`.

[28] *Refractive index database.* URL: `https://refractiveindex.info/?shelf=main&book=InP&page=Aspnes` (visited on 05/30/2024).

[29] Irving. *An Overview of DWDM Technology and DWDM System Components.* 2021. URL: `https://community.fs.com/article/an-overview-of-dwdm-technology-and-dwdm-system-components.html` (visited on 05/25/2024).

[30] Shiva Kumar and M Jamal Deen. *Fiber optic communications: fundamentals and applications.* John Wiley & Sons, 2014.

[31] N Bhusari Shraddha, Ujjwal Vikas, and S Jagdale Shantanu. "Analysis of SPM, XPM, and FWM in Fiber Optic Communication Using OptiSystem". In: *International Journal For Science Technology And Engineering* 2 (2016), pp. 136–142. URL: `https://api.semanticscholar.org/CorpusID:56058438`.

[32] Walid S. El-Deeb, M. Mohamed, and Abdelaziz E. Abdelnaiem. "Analysis of the Nonlinear Impairments on the DWDM Optical Communication Systems". In: *International Journal of Engineering* 22 (2017), pp. 19–26. URL: `https://api.semanticscholar.org/CorpusID:116522346`.

List of Figures

List of Tables

List of Acronyms

ADC	analog to digital converter. 37
ASE	amplified spontaneous emission. 22
BER	bit error rate. 25
BPD	balanced photodetector. 36, 38, 66
BPSK	binary phase shift keying. 13
C-SWaP	cost, size, weight and power. 5
CMA	Constant Modulus Algorithm. 41
CW	continuous wave. 16
DBPSK	differential binary phase shift keying. 13
DD	displacement damage. 11
DLI	delay line interferometer. 62
DoS	Denial of Service. *Glossar:* Denial of Service
DP-QPSK	dual polarisation - quadrature phase shift keying. 34
DQPSK	differential quadrature phase shift keying. 13
DSP	digital signal processing. 37
DWDM	dense wavelength division multiplexing. 5, 12, 73
EDFA	Erbium Doped Fiber Amplifier. 13, 22
EDRS	European Data Relay System. 9
FEC	forward error correction. 32
FSK	frequency shift keying. 30
FSO	free-space optical. 5, 15
FWHM	Full Width at Half Maximum. 18
FWM	four wave mixing. 73, 75
GEO	geostationary earth orbit. 5
HAPS	high-altitude platforms. 9
I/O	input/output. 60
IEEE	Institute of Electrical and Electronics Engineers. 44
InP	Indium Phosphide. 10
IoT	Internet of Things. 8
ITU	International Telecommunication Union. 13

LEO   low earth orbit. 9
LO   local oscillator. 26

MMI   multi-mode interferometer. 37
MZM   Mach-Zehnder modulator. 16

NF   noise figure. 24
NICT   National Institute of Information and Communications Technology.
           9
NRZ   non-return-to-zero. 39

OOK   on-off keying. 13
OSNR   optical signal to noise ratio. 45

PBC   polarisation beam combiner. 36
PBS   polarisation beam splitter. 36
PC   Polarisation controller. 37
PDF   probability density function. 29
PIC   Photonic Integrated Circuit. 5, 10
PR   polarisation rotator. 40
PRBS   Pseudo Random Binary Sequence. 39
PSD   power spectral density. 17

QAM   quadrature amplitude modulation. 13
QPSK   quadrature phase shift keying. 13

R&D   research and development. 9
RF   radio frequency. 8
RIN   Relative Intensity Noise. 17
rms   root mean square. 17
ROADM   Reconfigurable Optical Add-Drop Multiplexers. 68

SBS   Stimulated Brillion Scattering. 87
SEE   single-event effect. 11
SMP   self-phase modulation. 73
SNR   signal-to-noise ratio. 25
SRS   Stimulated Raman Scattering. 87
SWaP   size, weight and power. 9

TIA   transimpedance amplifier. 40
TID   total-ionizing dose damage. 11

VV   Viterbi-Viterbi. 41

XPM   cross-phase modulation. 73

Declaration of Independence

I hereby declare that I completed this work independently and that I have used no aids other than those referenced. The parts of the work, which include phrases or points taken from other sources, are clearly marked with the origin of the information. This also applies to diagrams, sketches, visual representations as well as for sources from the Internet.

I also declare that I have not submitted this work in any other testing procedure as an examination paper, nor will I in the future.

The submitted written work corresponds to the electronic version. I agree that an electronic copy may be made and stored to enable verification by anti-plagiarism software.

Place, Date   Signature